Energetic Processes on the Sun during the Extreme Events

Stochastic Particle Acceleration in Solar Flares

V. Petrosian[1], S. Liu[2]

[1]*Center for Space Science and Astrophysics, Department of Physics and Applied Physics, Stanford University, Stanford, CA 94305;* vahe@astronomy.stanford.edu

[2] *Los Alamos National Laboratory, Los Alamos, NM 87545; liusm@lanl.edu*

We review the stochastic particle acceleration by turbulent plasma waves in solar flares. Turbulence plays important roles in most of the astrophysical particle acceleration mechanisms and can convert energy of large scale flow motions and magnetic field fluctuations into heat and energetic particles. High resolution observations of solar flares suggest that this is the dominant channel of conversion of energy released by reconnection to radiation. In this magnetic field dominated environment obliquely propagating waves are subject to the transit-time damping by the background particles and may dominate the plasma heating. The waves propagating parallel to the magnetic field lines can cascade to the scale of the background particle gyro-radii and therefore accelerate particles efficiently from the thermal background to high energies. The model explains many features of X-ray and higher energy emissions from solar flares and the accompanying Solar Energetic Particle Events and has the potential to connect the observed are characteristics to the properties of the flaring plasma and the turbulence generation mechanism directly. The theory is quite general, addresses the acceleration of all charged particles in the background plasma, and may find applications in many high energy astrophysical sources.

1 Introduction

Acceleration of particles is ubiquitous in the universe. It takes place on a wide range of spatial scales from planetary magnetospheres to clusters of galaxies, it can occur on timescales less than a second to billions of years under a variety of conditions, and can produce particles with energies ranging from sub-keV to $>10^{20}$ eV. The accelerated particles are detected directly as galactic and extragalactic cosmic rays (CR), as solar energetic particles (SEPs), and indirectly by the nonthermal radiation they produce, which extends from long wavelength radio to TeV gamma-rays. Electrons emit via bremsstrahlung, synchrotron and inverse Compton processes and high energy protons (and ions) emit via excitation of nuclear lines and from decay of π_0 mesons produced in p- p interactions. All these products of the acceleration, except those arising from inverse Compton scatterings, are observed in solar flares and provide ample opportunity to investigate the acceleration process through both detection methods. Because of suns proximity to us the solar flares can be observed to a much greater detail than is possible for other astronomical sources, and provide us with an excellent laboratory for the testing of the theoretical models.

It is generally agreed that the are energy comes from the annihilation of magnetic fields via reconnection. Exactly how this energy is released or dissipated remains controversial. Dissipation can occur via *Plasma Heating, Particle Acceleration or Plasma Turbulence*. Initially, it was believed that most of the energy goes directly into heating. But the discovery of nonthermal radiations (microwaves, hard X-rays, HXRs, and gamma-rays) lead to the idea that all of the energy goes into the acceleration of particles, which produce the nonthermal radiations directly (via synchrotron for microwaves, electron bremsstrahlung for continuum X- and gamma-rays, and nuclear excitation by protons and ions for gamma-ray lines), and the thermal radiations (soft X-rays**, SXRs,** etc) by heating and evaporating the chromospheric plasma via collisions. Some of the accelerated particles escape the Sun and produce Type III bursts, and are observed near the Earth as SEPs. However, high resolution observations by instruments on board earlier and currently active (*RHESSI, ACE* and *WIND*) satellites, indicate that the above picture is not complete. It appears that plasma turbulence plays a more prominent role than suspected previously and most of the are energy goes through the third channel. The resultant turbulence, then can both accelerate particles stochastically and heat the plasma.

The particles couple with the waves via resonant interactions, which in principle only depend on the properties of the background plasma and wave generation mechanism. Given that the radiative processes and related transport effects have been well studied , one therefore expects to use the characteristics of the observed radiation to uncover the energy release process. Although there has been significant progress in our understanding of hydrodynamic (HD) and Magnetohydrodynamic (MHD) turbulence, there still remain some unsolved problems in the complex nonlinear interactions involved here. Nevertheless, the theory of resonant wave-particle interactions is relatively well established, and for a given spectrum of turbulence, one can evaluate the characteristics of the accelerated particles. Application of these to solar flares have lead to many interesting results.

The above mentioned satellites continue to provide excellent data for testing the predictions of this new paradigm. Over the past decade we have shown that many aspects of these observations can be explained in a model where the particles are accelerated stochastically by plasma waves or turbulence. Here we summarized some of the more recent results from these works. In the next section we give a brief description of the basic characteristics of the model and some theoretical arguments supporting it. These results will be very general and applicable to many astrophysical sources. In §3 we describe application of the model to solar flares and in §4 we compare model results with solar are observations concentrating on three topics, namely radiative signature of the electrons, the relative acceleration of electrons and protons, and finally the enrichments of certain ions in SEPs with focus on the relative acceleration of ^3He

and ^4He. In §5 we present a brief summary and some discussion.

2 Particle Acceleration

In this section we first compare various acceleration processes and stress the importance of plasma wave or turbulence (PWT) as an agent of acceleration, in general, and then describe the basic scenario and equations for treatment of these processes in solar flares by the stochastic acceleration (**SA**) model.

2.1 Theoretical Arguments

There are several lines of arguments indicating that **PWT** plays an important role in accelerating particles in solar flares. This may be true in other space and astrophysical plasmas as well. The three most commonly used acceleration mechanisms are the following.

Electric Fields parallel to magnetic fields can accelerate charged particles. For fields greater than the Dreicer field, $\mathbf{E}_D = k_{\rm B}T/e\lambda_{\rm Coul} \sim 10^{-5}(n/10^{10}{\rm cm}^{-3})$ $(10^7{\rm K}/T)$ V/cm/T) V/cm, where k_B, n, and T are the Boltzmann constant, the density, and temperature of the background plasma, respectively, particles of charge e gain energy faster than they lose by Coulomb collisions with mean-free-path $\lambda_{\rm Coul} \sim 9\times$ $\times 10^7(T/10^7{\rm K})^2(n/10^{10}{\rm cm}^{-3})$ cm. This can lead to runaway unstable particle distributions that give rise to PWT (Boris et al. 1970, Holman 1985). Sub-Dreicer fields, in order to accelerate electrons to gamma-ray ranges, must extend over a region of 1013 cm (>> length L ~10^9 109 cm of a typical are loop) unless the electrical resistivity or the plasma density is anomalously high (Tsuneta 1985; Holman 1996b). Also, for production of a broad power-law spectrum of particles one needs a wide range of potential changes (e.g. Litvinenko, 2003).

Shocks can accelerate particles to high energies if i) there is an injection process to overcome the losses at low energies and ii) there are some scattering agents to cause repeated passages of the particles through the shock front. For most astrophysical non-thermal sources, including solar flares, the most likely agent for scattering is plasma turbulence. This is called *diffusive shock acceleration* (Jokipii 1987). The rate of energy gain then is governed by the pitch angle scattering rate ($\propto D_{\mu\mu}$), the pitch angle diffusion coefficient, μ the cosine of the pitch angle). However, this turbulence can also accelerate particles stochastically with a rate of D_{EE}/E^2 (here DEE is the energy diffusion coefficient) so that shocks may not be always necessary. Moreover, there is no direct evidence for presence of shocks near the flaring loop during the impulsive phase when acceleration is taking place, and some of the features which make acceleration of cosmic rays by shocks attractive are not present in solar flares. On the other hand, in gradual flares there may be a need for a second stage acceleration of SEPs by coronal shocks.

Stochastic Acceleration (SA) is favored in solar flares for several reasons. First contrary to some beliefs Hamilton & Petrosian (1992) and Miller and Reames (1996) among others have shown that under are conditions plasma waves can accelerate the low energy background particles to high energies within the desired time. Second and more importantly, Pryadko & Petrosian (1997) have shown that at low energies and/or in strongly magnetized plasmas $D_{EE}/E^2 > D_{\mu\mu}$, so that SA is more efficient than the shock acceleration. Therefore, for are conditions, at least initially, low energy particles are accelerated more efficiently by plasma waves or turbulence PWT than by shocks, even if shocks are present. Note that in practice, i.e., mathematically, there is little difference between the two mechanisms (Jones 1994), and the contribution from shocks can be added as indicated in equation (3) below.

Irrespective of which process dominates the particle acceleration, it is clear that PWT has a role in all of them. Thus, understanding of the production of PWT and its interaction with particles is extremely important.

Turbulence is expected to be present in most astrophysical plasmas including solar flares because the ordinary and magnetic Reynolds numbers are very large. It is associated with efficient energy dissipations of non-equilibrium systems. Gradual accumulation of knowledge of waves in a magnetized plasma (see Pouquet et al. 1976; Shebalin, Matthaeus & Montgomery 1983; Higdon 1984; Passot et al. 1988; Matthaeus & Brown 1988; Norlund et al. 1992; Biskamp 1995; Goldreich & Sridhar 1995, GS95; Matthaeus et al.1996; Cho, Lazarian & Vishniac 2003; Biskamp 2003) has paved the way for a substantial progress in the understanding of both compressible and incompressible MHD turbulence (Lithwick & Goldreich 2003; Cho & Lazarian 2002 and 2003; Cho & Lazarian 2006). These provide new tools for a more quantitative investigation of turbulence and the role it plays in solar flares.

2.2 Basic Scenario

The complete picture of a solar are involves many phases or steps. After a complex pre-are buildup, the first phase is the reconnection or the energy release process. The final consequences of this released energy are the observed radiations from long wavelength radio to ~ GeV gammarays, SEPs, and CMEs. There are many steps involved in conversion of the released energy into radiation. As stressed above we believe that PWT plays an important role. We envision the following scenario. Magnetic energy is converted into turbulence by the reconnection process above corona loops which we refer to as the acceleration site or the loop top (LT) source. Shocks may also be produced at higher corona. The turbulence or waves undergo nonlinear interactions causing them to cascade to smaller scales. At the same time they are damped by the background plasma, accelerating particles into a non-thermal tail and heating the plasma directly, or indirectly via the non-thermal particles. The plasma particles while being energized by the PWT produce the observed non-thermal radiations via their interactions with the background particles (and fields). Most of the energy of the non-thermal particles is lost by collisions along the loop and at the FPs, causing heating and evaporation of the colder chromospheric plasma, which is responsible for most of the softer radiation. This process, described by the HD equations, has a time-scale comparable to the sound travel time, and is somewhat decoupled from

the acceleration process that has a much shorter time-scale. However, the evaporation can modulate the high energy processes by changing the density and temperature in the acceleration site. These processes can be addressed by the equations described below.

2.3 Basic Equations

We first present the general formalism for a complete treatment of the plasma heating and particle acceleration by turbulence, then shift to some details such as the resonant wave-particle coupling, the cascade of the turbulence and its damping by the background particles, and the transport of and radiation by the accelerated particles.

2.3.1 Kinetic Equations

The general equation for treatment of the particle transport is the Fokker-Planck equation for the gyro-phase averaged particle distribution f(t; s;E; μ) as a function of distance s along the magnetic field lines. This equation can be found in §A.1 of the appendix, where we also show the conditions under which this equation can be simplified. In most astrophysical situations, including solar flares, one can i) adopt the isotropic approximation (or deal with the pitch-angle averaged distribution) and ii) impose the homogeneity condition (or deal with distribution integrated over the acceleration region), which amounts to determination of the evolution of the energy spectrum N(t,E) =$\iint$d μ ds f(t,s,E, μ). In a similar vane, i.e., adopting the diffusion approximation (Zhou & Matthaeus 1990), one can obtain the evolution of the spatially integrated wave spectrum W(k; t) as a function of wave vector k:

$$\frac{\partial N}{\partial t} = \frac{\partial}{\partial E}\left[D_{EE}\frac{\partial N}{\partial E} - (A - \dot{E}_L)N\right] - \frac{N}{T^p_{\rm esc}} + \dot{Q}^p, \quad (1)$$

$$\frac{\partial W}{\partial t} = \frac{\partial}{\partial k_i}\left[D_{ij}\frac{\partial}{\partial k_j}W\right] - \Gamma(\mathrm{k})W - \frac{W}{T^W_{\rm esc}(\mathbf{k})} + \dot{Q}^W. \quad (2)$$

Here $D_{EE}/E^2, A(E)/E$ and $\dot{E}_L/E$ give the diffusion, direct acceleration and energy loss rates of the particles, respectively, and $D_{ij}(k)/k^2$ and $\Gamma(k)$ describe the cascade and damping of the turbulence. The $\dot{Q}$'s and the terms with the escape times Tesc describe the source and leakage of particles and waves (see Miller et al. 1996; Petrosian & Liu 2004, PL04). The two equations are coupled by the fact that the coefficients of one depend on the spectral distribution of the other. Conservation of energy requires that the energy loss of the turbulence $\dot{W}_{tot} \equiv \int \Gamma(\mathrm{k})W(\mathrm{k})d^3k$ be equal to the energy gain from the waves by the particles $\dot{\varepsilon} = \int [A(E) - A_{sh}]N(E)dE$. Representing the energy transfer rate between the waves and particles by $\sum(\mathrm{k;E})$ this equality implies that

$$\Gamma(\mathbf{k}) = \int_0^\infty \mathrm{d}EN(E)\Sigma(\mathbf{k},E),$$

$$A(E) = \int_0^\infty d^3kW(\mathbf{k})\Sigma(\mathbf{k},E) + A_{\rm sh}\ , \quad (3)$$

where we have added Ash to represent contributions of other processes, e.g. shocks.

2.3.2 Dispersion Relation and Coefficients

The wave-particle interaction rates $\sum$ (that determines D_{EE};A(E) and $\Gamma(\mathrm{k})$) are obtained from the plasma *dispersion relation* ω(k) (e.g., in the MHD regime for a cold plasma, ω = υ_A kcosθ and υ_A k for the Alfvén and fast magneto-sonic waves, respectively) and the resonant condition ω-k cosθμυ=nΩ/γ for waves propagating at an angle θ with respect to the magnetic field and particles with gyro-frequency , velocity v, and Lorentz factor . Here the harmonic number (not to be confused with the density) n = 0 corresponds to the transit time damping (TTD) process, for parallel propagating waves (PPWs) n=$\pm$ 1, and for obliquely propagating waves n can be any integer. The complete equations for calculation of these coefficients in a cold plasma are given in the appendix. The primary parameter here is the Alfvén velocity in units of the speed of light [1]

$$\beta_{\rm A} = v_{\rm A}/c = 7\times10^{-3}(B/100{\rm G})(10^{10}{\rm cm}^{-3}/n)^{1/2}. \quad (4)$$

Figure 1 shows the dispersion surfaces (depicted by the colored curves) obtained from equation (15) for all possible modes in a cold plasma along with the resonant planes (colored planes) in the (k; $k_\perp$; ω) space. Intersections between the dispersion surfaces and the resonant planes define the resonant wave-particle interactions.

The right and left panels show these near the proton and electron gyro-frequencies, respectively. The resonant condition for each mode is satisfied along the curve ω_{res} (k , θ , E, μ) obtained from the intersections of the mode dispersion surface with resonant planes (for a given E and μ). The rates flare evaluated along such curves (see §A.2). The wave diffusion coefficient D_{ij} resulting from nonlinear wave-wave interactions is also determined by the dispersion relation (e.g., the solution for three wave processes ω($\mathbf{k}_1$)+ω($\mathbf{k}_2$)=ω($\mathbf{k}_3$) and $\mathbf{k}_1+\mathbf{k}_2=\mathbf{k}_3$ clearly depends on this relation.)

The above dispersion relations are good approximations for low beta plasmas,

$$\beta_p = 2(v_s/v_{\rm A})^2 = 8\pi nk_{\rm B}T/B^2 = 3.4\times10^{-2}(n/10^{10}{\rm cm}^{-3}) \quad (5)$$

$$(100{\rm G}/B)^2(T/10^7{\rm K}) \ll 1,$$

where $\upsilon_S \sim \sqrt{k_S T/m_P}$ is the sound speed. For higher beta plasmas, e.g., at higher temperatures, these relations are modiffied, specially for higher k's. For example, in the MHD regime, in addition to the Alfvén mode one gets fast and slow modes with the dispersion relation (see e.g., Sturrock 1994)

[1] Other parameters are the masses and relative abundances of electrons, protons and α-particles in the background Plasma which flare known. Note also that $\beta_{\rm A}^{-1} = \alpha_p = \alpha/\sqrt{\delta}$, where $\alpha(\alpha_p)$ is the ratio of plasma to gyro-frequency of electrons (protons), $\delta \equiv m_e/m_p$, and me and mp are the electron and proton masses, respectively.

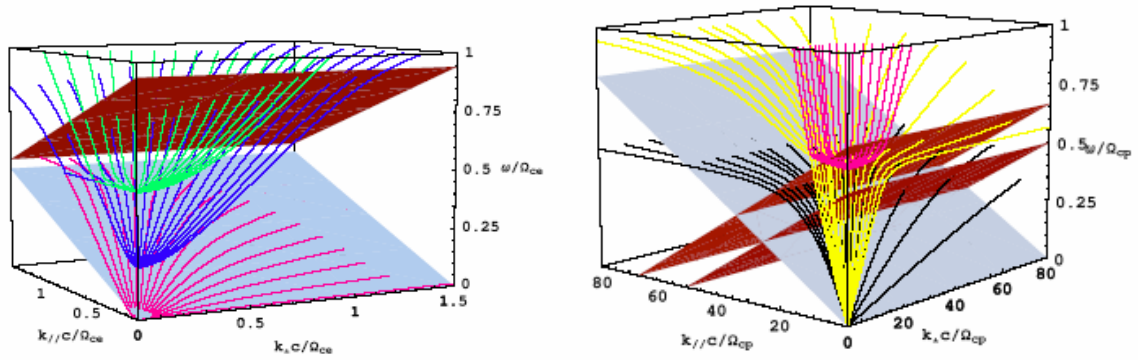

Fig.1. Dispersion relation (curves) and resonance condition (at) surfaces for a cold fully ionized H and He (10% by number) plasma with β_A *= 0.012 showing the regions around the electron (left) and proton (right) gyro-frequencies. Only waves with positive k;* $k_\perp$ *(or* $0 < \theta < \pi/2$*) are shown. The mirror image with respect to the (ω;* $k_\perp$*) plane gives the waves propagating in the opposite direction. From high to low frequencies, we have one of the electromagnetic branches (green), upper-hybrid branch (purple), lower-hybrid branch, which also includes the whistler waves (pink), fast-wave branches (yellow), and Alfvén branch (black). The effects of a finite temperature are discussed by André (1985). The resonance surfaces are for electrons with v = 0.3c and* $|\mu|$ *= 1.0 (left: upper n = 1, lower n = 0) and* ^4He *(right: middle n = 1) and* ^3He *(right: upper n = 1) ions with* $|\mu|$ *= 1.0 and v = 0.01c. The resonance surfaces for the latter two are the same when n = 0 (right: lower).*

$$(\omega/k)^2 = \frac{1}{2}\left[(v_A^2 + v_s^2) \pm \sqrt{v_A^4 + v_s^4 - 2v_A^2 v_s^2 \cos 2\theta}\right], \quad (6)$$

and the more general dispersion relation is modified in a more complicated way (see e.g., André 1985 or Swanson 1989). The finite temperature imparts an imaginary part to the wave frequency that gives the (Landau) damping rate of the wave (see e.g., Pryadko & Petrosian 1998, 1999 and below). But it changes the real part of the frequency slightly so that often the real part can be evaluated using the simpler cold plasma dispersion relation.

In principle, given the plasma parameters, n; B; T, the geometry of the region (represented by a size L here), the rate and scale of injection of turbulence $\dot{Q}^W$ (**k**,t),one can evaluate the coefficients of equations (1) and (2) and solve the coupled kinetic equations for determination of the resultant distributions N(E; t) and W(**k** ; t). However, as described next more simplifications are possible under many circumstances.

2.3.3 Turbulence Cascade and Damping

The physical processes involved in a full description of PWT, i.e. W(k; t), are its generation, cascade, damping, and spatial diffusion as represented by the four terms on the right hand side of equation (2). The turbulence most probably is generated through an instability, e.g., reconnection process in solar flares, but the particular scenario (see Priest & Forbes 2000, Biskamp 2000, Lazarian, Vishniac & Cho 2004, Shay et al. 2004) is not important for most studies. One may assume that the bulk of energy is injected within a narrow range of scales below the characteristic size L of the system and cascades down to smaller scales. Usually the effects of the escape term can also to be neglected because this equation is spatially integrated over a region that includes most of the turbulence. Consequently, one may focus on the cascade and damping processes.

The wave kinetic equation simplifies considerably at large scales (low k), where the cascade time $\tau_{cas} = k^2 D_{ij}^{-1} \ll \Gamma^{-1}$ and damping can be neglected, and because, in general, cascade time is also shorter than the dynamic time τ_{dyn}. Thus, in the so-called *inertial range*, the range between the injection $k\,\mathrm{min} > L^{-1}$ and k_{max}, where the damping becomes dominant, equation (2) reduces to

$$\partial(D_{ij}\partial W/\partial k_i)/\partial k_j = \dot{Q}^W(k,t).$$

This clearly is decoupled from the particle kinetic equation (1) and for a given (narrow) injection spectrum $(\text{say, } \dot{Q}^W \propto \delta[k - k_{\min}])$, depends only on the cascade rate Dij determined by the nonlinear wave-wave interactions. For example, for HD *turbulence* of an incompressible fluid $D(k) \propto k^{7/2}\hat{W}^{1/2}$ and the cascade time $\tau_{cas} \sim k^2/D$, the cascade results in a Kolmogorov spectrum, $\hat{W}(k) \propto k^{-5/3}$, where $\hat{W} = 4\pi k^2 W$ is the isotropic wave spectrum.

MHD *turbulence* is more complex because the frozen-in magnetic fields alter the dynamics of the fluid. Solar flares are magnetically dominated, $\beta_p = 8\pi n k_B T/B^2 < 10^{-2}$, and we need to consider also the Alfvén time-scale $\tau_A \sim (k_\parallel v_A)^{-1}$. As shown by Goldreich & Sridhar (1995) strong Alfvénic turbulence in an incompressible fluid undergoes a *scale-dependent* anisotropy with $k_\perp \sim k_\parallel^{2/3}$. Numerical studies of turbulence in a *compressible magnetically dominated* plasma by Cho & Lazarian (2002) show that Alfvén modes undergo an identical anisotropic cascade. Slow modes which are passively mixed up by Alfvén modes also show

anisotropic cascade but fast modes interact with Alfvén and slow modes only marginally and produce an isotropic cascade. Table 1 summarizes some relevant cascade characteristics and spectra in the inertial range for different modes.

The inertial range terminates at the critical damping scale where the damping rate is equal to the cascade rate, $\Gamma(k_c)=\tau_{cas}(k_c)^{-1}$. Beyond this $k>k_c$ the turbulence is heavily damped and its spectrum cuts off steeply. This determine the upper bound of the spectrum $k_{\max}=k_c$.Damping can be caused by the thermal background particles and by the accelerated non-thermal electrons and protons. It is through the latter process that the particle and wave kinetic equations are coupled. MHD damping is dominated by the TTD processes. Petrosian Yau & Lazarian (2006) (PYL06) compare various damping processes of the fast modes and found that for solar are conditions viscous damping can be neglected compared to collisionless damping (except at the largest scales, where damping is unimportant). The latter damping rate is proportional to the product of density and mean momentum of the particles. Thus, in most flares damping by background thermal particles is more important than that due to the non-thermal tails. *This again simplifies the problem because the non-thermal particle and wave kinetic equations can be decoupled, except now we must include the damping term* [2].

[2]However, the situation may be more complicated in large intense flares where the density N of non-thermal electrons (with energies above E0) may be $> n\sqrt{k_B T/E_0}$. In this case then the damping of the waves by the

Table 1: Scaling Cascade Characteristics of Turbulence in Magnetically Dominated plasma. (a-b) Goldreich & Sridhar 1995, Lithwick & Goldreich 2001, Cho & Lazarian 2002; Cho & Lazarian 2003, Beresnyak, Lazarian & Cho (2005) (c) ; Cho & Lazarian 2002; Cho & Lazarian 2003, (d) Biskamp et al. (1999), Cho & Lazarian (2004).

Mode	Isotropy	$\hat{W}(k)$	$\tau_{\rm cas}\propto$
Hydrodynamic	Isotropic	$k^{-5/3}$	$(kL)^{-2/3}$
Alfvén[(a)]	NO, $k_\perp \propto k_\parallel^{3/2}$	$k_\perp^{-5/3}$	$(k_\perp L)^{-2/3}$
Slow[(b)] [(a)]	NO, $k_\perp \propto k_\parallel^{3/2}$	$k_\perp^{-2}$	$(k_\perp L)^{-2/3}$
Fast[(c)]	Isotropic	$k^{-3/2}$	$(kL)^{-1/2}$
Whistler[(d)]	NO $k_\perp \sim k_\parallel^{1/3}$	$k^{-7/3}$	$(k_\perp L)^{-4/3}$

Figure 2 shows the cascade and damping time-scales for different angle θ between k and the B fields (or β^p). The damping time-scale has a strong θ dependence, $\Gamma \propto (kL)^{-1}\sin^2\theta/\cos\theta$ (see e.g., Ginzburg 1961), so that as shown in the right panel the critical scale varies significantly with θ. Thus, even the fast mode which undergoes an isotropic cascade will develop strong anisotropy at large k with quasi-parallel and quasi-perpendicular modes cascading to ranges well below the proton gyro radius which is beyond the MHD regime. The quasi-perpendicular mode may be affected by B field irregularities and be damped. Thus, it appears that only parallel propagating waves (PPWs) reach small scales and can accelerate low energy electrons.

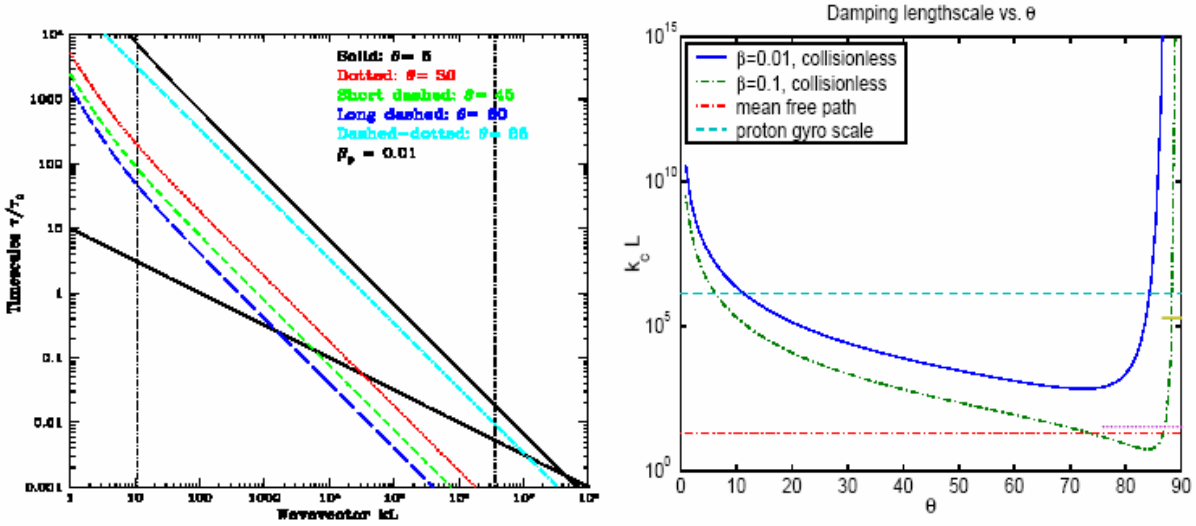

*Figure 2: Left panel: Variation with wave number k (in units of injection scale L^{-1}) of the cascade and damping time-scales (in units of $\tau_0 = L/v_A$) of fast modes for various angles θ between **k** and B and for plasma beta $\beta_p = 0.1$. Note the steepening at low values $kL < L/\lambda_{\rm Coul}$ due to emergence of viscous damping ($\lambda_{\rm Coul}$, the Coulomb mean free path, is represented by the left vertical dotted line). The critical damping wave vector k_c is given by the intersection of the two time-scales. The vertical dotted lines at the right side show the scale of the proton thermal gyro-radius $L/r_{q,p}$. **Right panel**: Normalized cutoff scales k_c of turbulence due to thermal damping vs. the angle θ. The horizontal dash-dotted and dashed lines represents the scales of the mean free path and the thermal proton gyro radius, respectively. The dotted lines show the effect of field wandering near 90^0 for β_p =0.1. Note that the critical scale is almost always smaller than the mean free path so that the viscous damping can play only a marginal role (PYL06).*

Gyro-resonance and other damping must be included at higher wave-numbers, where TTD may not be the dominant process and higher harmonics (n > 0) must be included in the evaluation of the resonances. In addition, as shown in Figure 1 the dispersion relation here deviates significantly from simple ideal MHD relations and can have profound effects on the cascade and damping processes. As in the case of the MHD modes, the damping in general, and that due to non-thermal particles specifically, can be evaluated through use of equation (3) (see PYL06). The collisionless thermal damping (most often the dominant process) can be evaluated as was done by Pryadko & Petrosian (1998 and 1999, see also Cramner & van Ballegoojian 2003). In this approach one uses the hot plasma dispersion relation (see e.g. Swanson 1989) and evaluates the imaginary part of the mode frequency θ. Again, when $\omega_i > \tau_{cas}^{-1}$ the waves are damped. In Figure 3 we demonstrate how one obtains the value of kmax and kmin for parallel propagating waves. Following the diffusion approximation waves in the proton cyclotron (PC) branch (upper solid line) is generated via its coupling with waves in the right-hand-polarized fast mode branch (dashed line). These can be repeated for other angles θ or obtained from the two dimensional description using a version of Figure 1 that includes the thermal effects (see Rönnmark 1983, André 1985).

2.3.4 Particle Transport and Radiative Processes

The accelerated particles escape the turbulent LT region with the spectral flux N(E)/Tesc. Their transport is described by an equation similar to (1), though the pitch angle dependence must be included (the $D_{\mu\mu}$ term in eq. [10] of appendix). This yields the energy spectrum N(E;μ; s) as a function of the distance s along the field lines. Some of the escaping particles travel out along open field lines, produce radio waves and are detected near the Earth as SEPs. Others travel down the legs of the loops and produce bremsstrahlung and synchrotron radiation along the loop and at its foot points (FPs). For example, the bremsstrahlung (with a differential cross section σ_b) emissivity J at photon energy ϵ and direction ϕ with respective to the particle beam is given by (see appendix)

$$J(\epsilon,\phi,s)=\int_{\epsilon}^{\infty} n(s)v\ N(E,\mu,s)\sigma_b(\epsilon,\phi,E,\mu)\mathrm{d}E d\mu. \quad (7)$$

For the LT source n (s) = n_{LT} , and N(E; μ; s) = N(E) is obtained from equation (1). The thick target emission (integrated over the loop outside the LT, mainly from FPs) is obtained with non-thermal electrons cannot be neglected and one must solve the coupled kinetic equations simultaneously.

$$n(s)N(E,\mu,s)=\frac{n_{LT}}{\dot{E}_L}\int_E^{\infty}\mathrm{d}E'\frac{N(E')}{T_{\mathrm{esc}}(E')}, \quad (8)$$

where $\dot{E}_L$ and n_{LT} T refer to the LT (see appendix).

In Summary all of the above mentioned processes depend only on the density, temperature, magnetic field of the medium and the level and scale of generate PWT. The acceleration of different charge particles and the plasma heating therefore are determined by the instabilities and the initial properties of the background plasmas, and only a few parameters are needed in a self-consistent treatment. Ultimately observations must determine the validity of the models. As described below we have made extensive comparisons of the results from the SA model with observations of solar flares (and other sources). To our knowledge, there have not been similarly detailed comparisons for electric field or shock acceleration.

3 Application to Solar Flares

3.1 Basic Model

Figure 4 presents a schematic diagram of three possible scenarios (left) for conversion of energy released by

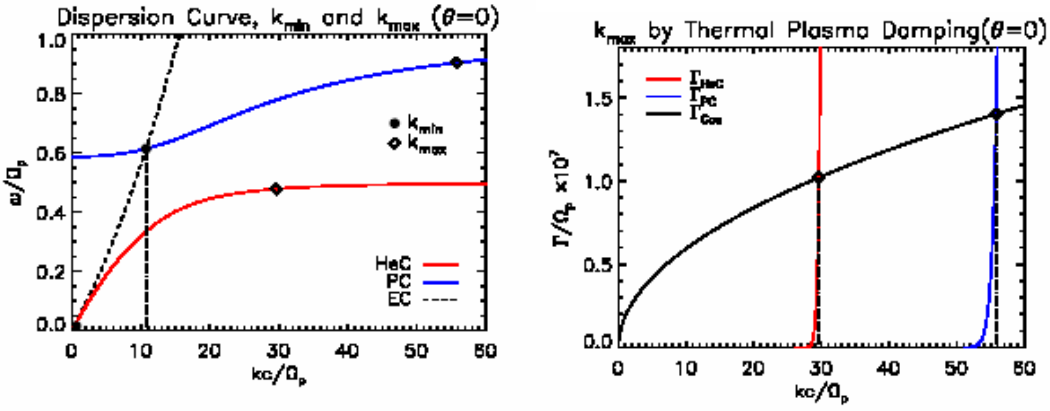

Fig.3. ***Left panel****: Dispersion relation [real part of the frequency* $\omega_r(k)$ *for PPWs and for a hot (*$T = 3\times10^6$ *K) fully ionized H and He (10% by number relative to H) plasma with* $\beta_A = 0.012$*, showing the determination of critical parameters of the SA model (under the diffusion approximation), namely kmin for the proton cyclotron (PC) branch.* $k_{\min}$ *for the electron cyclotron (EC) and He cyclotron (HeC) branches are determined by the injection scale. The dashed curve represents the right-hand-polarized waves and the solid curves represent left-hand-polarized. Right panel: Dependence of the cascade* $\Gamma_{cas} \equiv \tau_{cas}$ *and damping (*$\Gamma=\omega_i$*, the imaginary part of the wave frequency) rates on k and the determination of the* $k_{\max}$*'s. The turbulence intensity is chosen for typical solar flares.*

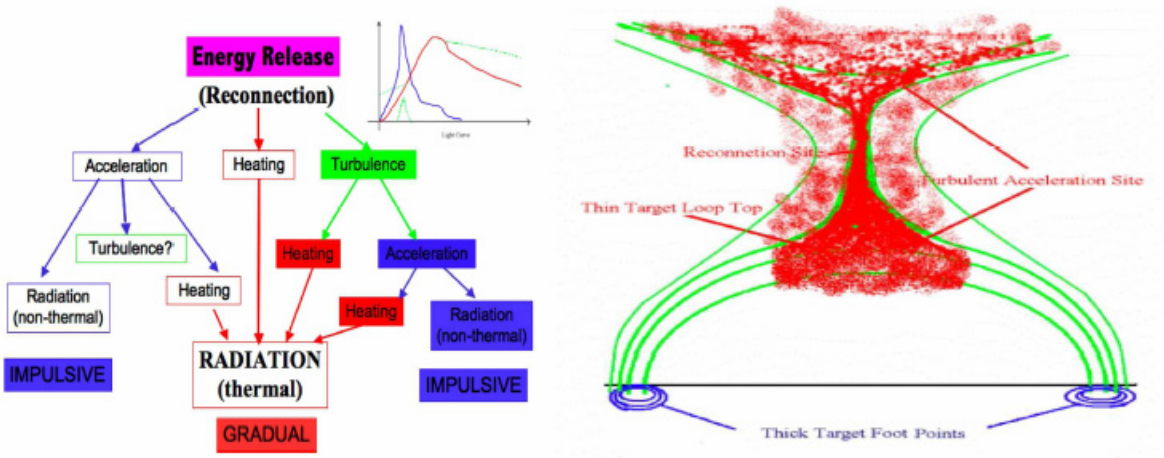

Fig.4. ***Left panel****: Energy flows in different scenarios for solar flares. Here we have ignored the energy fluxes associated with SEPs and CMEs. The blue, red, and green colors represent the energy content of the non-thermal, thermal, and the turbulence components. The inset on the upper-right is a schematic plot of the HXR (blue), SXR (red) light curves obeying the Neupert effect. The green curves show aspects of the SXR light curves which disagree with the scenario based on the left hand channel.* ***Right panel****: A cartoon of the structure of a simple flaring loop showing the reconnection and acceleration sites and the geometry of the field lines (green) and turbulence (red). The blue lines represent the HXR emitting FPs.*

reconnection to radiation, and a model for a simple solar are consisting of a single loop with an **X** reconnection configuration (right). When solar flares were first observed, the lack of a broad spectral information led to the simplest scenario where the emission is assumed to be thermal and the energy release during the are simply heats the plasma as shown by the middle channel in the left panel of Figure 4. However, the detection of high frequency radio, HXR, and gamma-ray emissions in solar flares indicate that some of the observed emission is non-thermal. Following the discovery of the rough correlation between the time derivative of the light curve of the thermal emission and first the light curve of the non-thermal microwave emission (Neupert 1968) and later the light curve of the HXR emission (Dennis & Zarro 1993), known as the Neupert effect, it was suggested that most of the are energy goes into non-thermal particles. Such particles on the newly closed field lines penetrate down the solar atmosphere and produce the non-thermal emission (e.g. HXRs), and heat the plasma which evaporates, fills the are loop and produces most of the thermal emissions (e.g. SXR). The left channel in Figure 4 shows the steps involved in this scenario. Presumably, the particles on open field lines give rise to SEPs observed near the Earth. However, the exact mechanism of the acceleration is not specified here.

Our assertion, based on theoretical arguments given above and the observations described below, is that most of the are energy arising from reconnection is dissipated via the right side channel of the diagram and produces the turbulence shown as red foam on the right panel. The turbulence heats the plasma and accelerates particles. In what follows we will deal with observations of such simple are loops. Large intense flares tend to more complicated consisting of many loops with a more complex evolution. We believe that the basic scenario applicable to simple loops can be generalized for more complex cases.

3.2 Basic Conditions

Dispersion Relation: As we have shown in § 2.3.3, plasma waves propagating obliquely to the magnetic field are subject to the TTD by the background particles. The damping likely results in a direct heating of the plasma by the turbulence. The PPWs, on the other hand, are not damped until they are near the particle gyro-frequencies and can play the dominant role of pulling out the particles from the thermal background and accelerating them to high energies. We therefore focus on the SA by PPWs. To simplify the model we assume the plasma is cold and the major elements are fully ionized. Thermal effects are expected to modify the quantitative results slightly. Figure 5 shows the dispersion relation for these waves and their resonant interactions with electron, proton, ^{3}He , and ^{4}He. As emphasized in PL04 and Liu, Petrosian, & Mason (2004 and 2006) the usage of the exact dispersion relation, including the effects of background α _particles play crucial roles in the model.

Turbulence Spectrum: A unified model for the evolution of turbulence from the MHD regime to the kinetic regime is still under-developing. However, as stated in §2.3.3, for most flares damping is dominated by thermal electrons so that wave and non-thermal particle kinetic equations are decoupled. Moreover, since the different terms in equation (2) dominate at different wave-number ranges, a broken power-law energy spectrum for each of the five wave branches provides a reasonable description of the properties of the turbulence:

$$\hat{W}(k) = (q-1)\frac{\mathcal{W}}{k_{\min}} \begin{cases} (k/k_{\min})^{q_l}, & \text{for } k < k_{\min}, \\ (k/k_{\min})^{-q}, & \text{for } k_{\min} < k < k_{\max}, \\ (k_{\min}/k_{\max})^{q}(k/k_{\max})^{-q_h}, & \text{for } k > k_{\max}, \end{cases} \quad (9)$$

where W is the total energy density of the specific plasma waves. We assume that $k_{\min} \sim 2\pi c/L\Omega_e$ for the EC and HeC branches. Waves in other branches are likely generated via their coupling with the EC and HeC waves. The $k_{\min}$

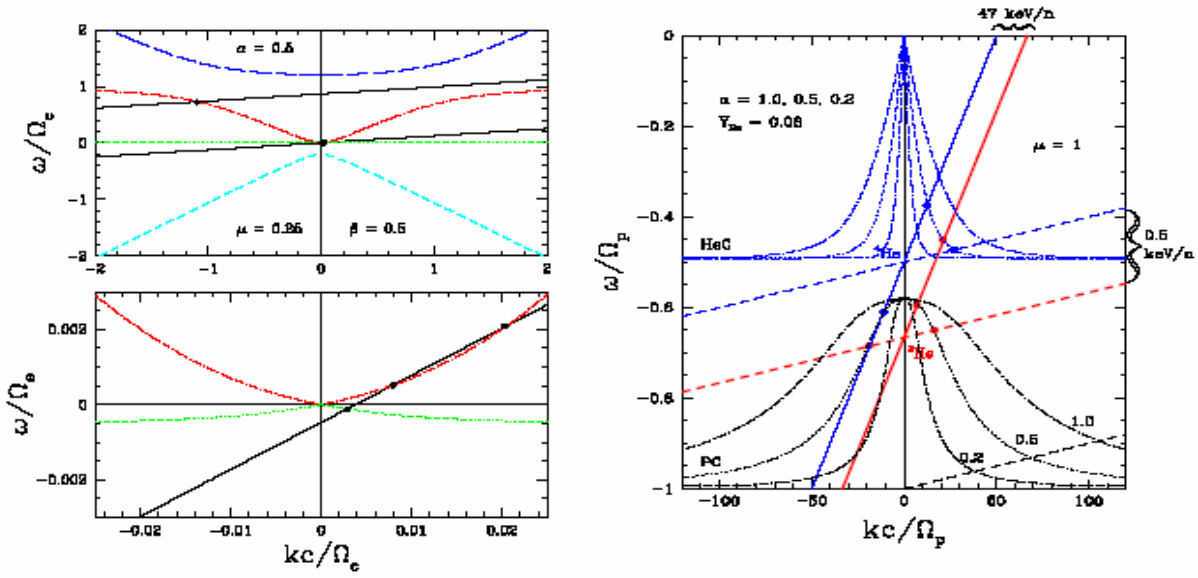

Fig.5. ***Left panel****: Dispersion relation of parallel propagating waves in a cold but fully ionized electron-proton* [4] *He plasma with* α_A *=1.0 or* β_A *=0.023 and the fractional abundance (by number relative to electrons) of α particle* Y_{He} *=0.08 The bottom panel is an enlargement of the region around the origin. The curves, from top to bottom, describe the EM (electromagnetic, long-dashed), EC (electron cyclotron,dot-dashed), HeC (helium cyclotron, green-dotted), PC (proton cyclotron, blue-dotted), and a second EM (short-dashed) waves. The upper and lower straight solid lines give, respectively, the resonance conditions for electrons and protons with velocity υ =0.5c and μ=0.12 Resonant interactions occur at the points where these lines intersect the curves which depict the waves (open circles). The crosses indicate the expected breaks in the turbulence spectrum as discussed in the text (PL04).* ***Right panel****: Dispersion relation of the HeC and PC branches for α=1.0;0.5;0.2. The four straight lines give the resonance condition for* [3] *He (red) and* [4] *He (blue) with μ=1 and energy of 47 (solid) and 0.5 (dashed) keV/nucleon (LPM04, 06). The lower (black-dashed) line is for a 0.5 keV proton.*

should be close to the point where two dispersion surfaces touch each other (see Fig. 1). For example the $k_{\max}$ for the PC branch should be comparable to $\Omega_p / 2\upsilon_A$. The $k_{\max}$ is determined by the Landau damping and is different for different wave branches. However, we assume that the spectral indexes and $\overline{\mathcal{W}} \equiv (q-1)\mathcal{W}(k_{\min})^{q-1}$ are the same for all branches so that the wave intensity only depends on the wavenumber k in the inertial ranges, i.e. , between $k_{\min}$ and $k_{\max}$. We choose q = 2.0 and q_h = 4.0, which are consistent with solar neighborhood observations (Bieber et al. 1994; Dröge 2003)[3]. For q = 2.0 the acceleration and scattering rates of relativistic particles are independent of energy (corresponding to the socalled hard sphere approximation), which gives rise to a power-law particle distribution that is cut off at an energy where the particle resonates with waves with $k < k_{\min}$, or where a loss process becomes dominant (PL04). Clearly the total turbulence energy density

$$\mathcal{W}_{\rm tot} \simeq 2\sum_{\sigma}\mathcal{W}^{\sigma} = [2\overline{\mathcal{W}}/(q-1)]\sum_{\sigma}(k^{\sigma}_{\min})^{1-q} \quad ,$$

where σ indicates the wave branches and the factor of 2 arises from the two propagation directions of the waves.

3.3 Particle Spectra:

Using this spectrum for the waves and the dispersion relation for PPWs we determine the coefficients of equation (1) and solve it to determine the steady state spectrum N(E) of different species. The steady state assumption is justified because usually the dynamic evolution time-scale of most characteristics of flares is longer than the microscopic time-scales like the acceleration, loss, or escape times. The spectral characteristics of N(E) arise from the interplay among these rates or time-scales associated with the terms in equation (1); these are the energy loss time τ_{loss} = E $/\dot{E}_L$, the energy diffusion time $\tau_{dif} \sim E^2 / D_{EE}$ or direct acceleration time τ_A=E/A(E), and the escape time $T_{\rm esc} = T_{\rm cross}(1 + T_{\rm cross}/\tau_{\rm scat})$ [4]. Figure 6 shows the energy dependences of these times (left panel) and the resultant electron and proton spectra at the acceleration site (LT) and the equivalent thick target spectra at the FPs (right panel). The model parameters are indicated in the figure, where T is temperature of the injected electrons and protons. Spectral breaks expected at critical energies where the time-scales cross or diverge (points) are evident in the right panel. In general, the SA by PWT always produces a \quasi-thermal" component and a harder non-thermal tail. In other words it both \heats' the plasma and accelerates particles. The LT spectra are softer and often dominated by the thermal component and have a steep non-thermal component, while the FP spectra are harder and have very

[3] The value of q_1 is unimportant as long as it is much larger than 1. We set $q_1 = 2$ in our calculation.

[4] The escape time T_{esc} is defined to account for the possibilities of τ_{scat} less or greater than $T_{cross} = L/\mathrm{v}$, time for particle to cross freely an acceleration site of size L.

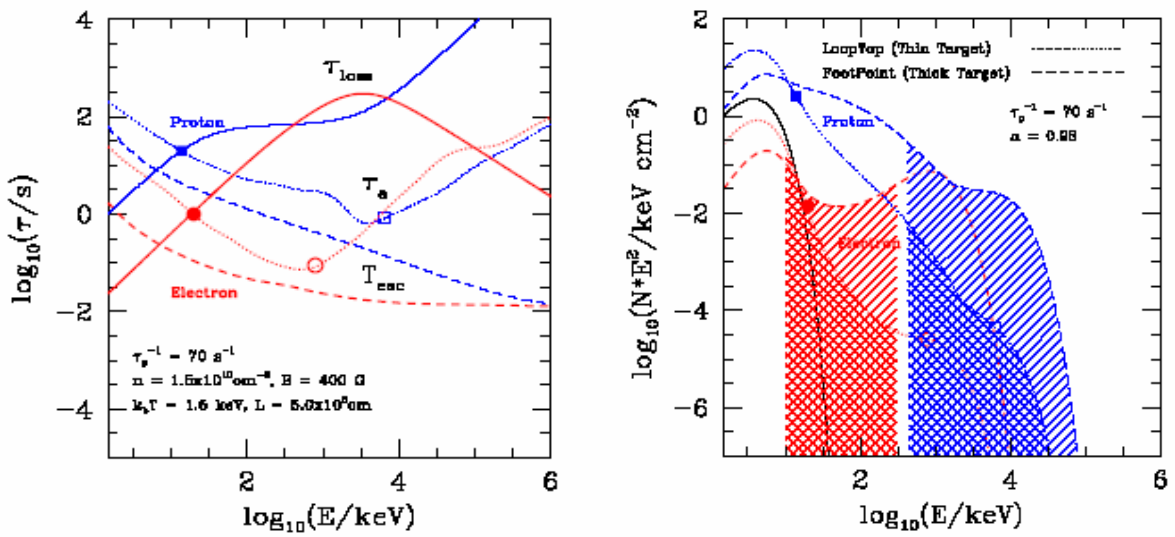

Fig.6. Left panel: Time scales for a SA acceleration model for solar are conditions and an assumed spectrum of PWT. Model parameters are indicated in the figure ($\tau_p^{-1} \sim \Omega_e W_{tot}/B^2$ and $\alpha \propto \sqrt{n}/B$). The acceleration, escape, and loss times are indicated by the dotted, dashed, and solid curves, respectively. The thick (red) curves are for electrons and thin (blue) curves are for protons. ***Right panel****: The corresponding steady-state spectra of accelerated electrons and protons. The dotted curves give N. The dashed curves indicate the thick target equivalent spectra of escaping particles (see § 2.3.4). The solid (black) line gives the shape of the background (injected) particle distribution. The hatched areas show the frequently observed ranges (see PL04). Spectral features occur at the intersections and divergences of these time-scales (circle and square signs). Using these spectra we can evaluate the emission characteristics at the acceleration site (thin target) and at the FPs (thick target) due to electrons escaping down along the closed lines, and the spectrum of particles escaping the sun along the open lines which are observed as SEPs. Below we compare some aspects of these results with observations of several flares.*

little or no thermal part. The relative importance of \heating" υs \acceleration" is most sensitive to the level of turbulence W or the model parameter τ_p^{-1} in the figure. As shown below these features agree with observations.

4 Comparison with Observations

We now compare the model results with some old and some new observations.

4.1 Radiative Signatures of Electrons

As an example of radiative signature of electrons in flares we consider the spectra of the HXRs emitted via the bremsstrahlung process. First evidence for importance of PWT came before the availibility of imaging spectroscopy from considerations of the overall non-thermal are spectra. Although the early HXR spectra observed over a narrow energy band could be fitted with a simple power-law model, later broader band spectra showed considerable deviations with several breaks and/or cutoffs. Spectral steeping below a few tens of keV, where Coulomb collisions dominate, and sharp cut offs around a few tens of MeV were observed in many flares (e.g. from SMM; Marschhäuser et al. 1994, and CGRO; Dingus et al. 1994 and Lin & Schwartz 1987; Park, Petrosian, and Schwartz 1997; Hamilton & Petrosian 1992). These breaks present in the so-called electron dominated

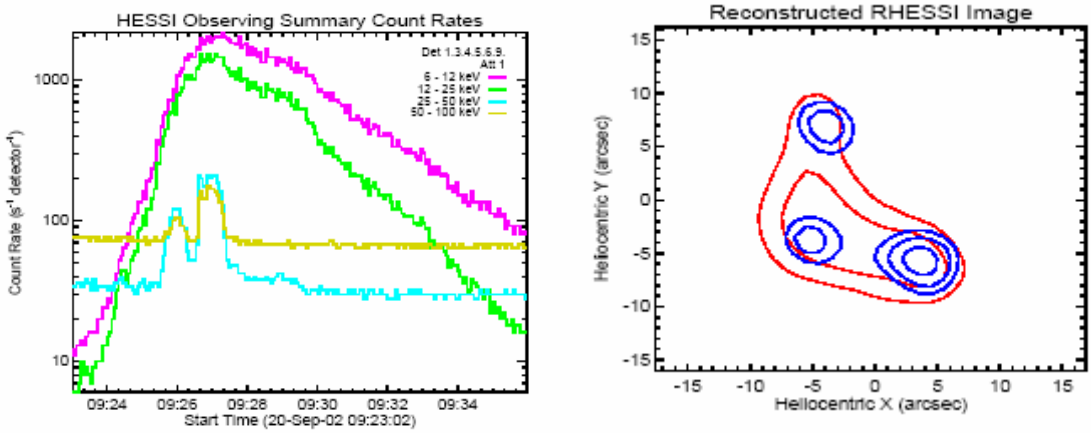

Fig.7. ***Left panel****: RHESSI light curves of flare 09/20/2002 at several energies showing the rise of the SXR emission well before the start of the impulsive phase determined by the higher energy HXR emission. The discrepancy during the decay phase mentioned in the text is discussed below.* ***Right Panel****: RHESSI image of the same are during the second HXR pulse (09:26:36 - 09:27:20 UT). The red contours are for 21.3-23.8 keV (at 20, 50% of the maximum brightness), showing the loop. The blue contours for 23.8-26.5 keV (at 30, 50, 80% of the maximum), showing the LT (the middle source) and two FPs (upper and lower sources).*

flares where the contribution from the nuclear lines is negligible, cannot be solely due to transport or optical depth effects (Petrosian 1994) and are natural consequences of the SA model with reasonable physical conditions (Park, Petrosian & Schwartz 1997). As described below *RHESSI* imaging spectroscopy has clarified this situation considerably.

The model described by the left side channel of left panel of Figure 4, where all the energy is released during the impulsive phase and goes directly to non-thermal electrons, has encounterd some difficulties. For example, it has also been known for sometimes that *pre- and post-impulsive phase* observations disagree with it. These are precursor SXR emission referred to as *preheating* and the slower than expected temperature decline in the decay phase, shown schematically by the green segments in the upper right corner of left panel of Figure 4 (see, e.g. McTiernan et al. 1993). *RHESSI* has provided considerable new evidence about this as well, an example of which is shown on the left panel of Figure 7. As described below these aspects are also consistent with the predictions of SA model.

Spatial Structure and Evolution: However, the most direct evidence for the presence of PWT is observations by *Yohkoh* of impulsive hard X-ray (10-50 keV) emission from a distinct LT source (Masuda et al. 1994, Masuda 1994). Further analysis of *Yohkoh* data (Petrosian, Donaghy &McTiern n 2002) and many RHESSI flares (Liu et al. 2003) show that this feature is the rule rather than exception. Moreover, Petrosian & Donaghy (1999) have also analyzed all the models proposed for this emission (Leach & Petrosian 1983, Leach 1984, Wheatland & Melrose 1995, Holman 1996a, and Fletcher & Martens 1998) and concluded that the successful models require an enhanced pitch angle scattering so that electrons are confined near the LT. Coulomb collisions cannot be this agent because of high losses they entail, and the most likely scattering agent is PWT, which can also accelerate particles. The right panel of Figure 7 shows a typical example of a flaring loop with distinct LT and FP sources.

RHESSI images of the LT and FP sources have revealed many new and interesting features which are consistent with the basic scenario outlined above and can constrain its parameters. In several flares with simple morphologies the LT source initially, for a short time period, dips down lower but then monotonically rises up into higher corona (Sui & Holman 2003, and Liu et al. 2004). In an large X-class are with a simple morphology we have discovered a correlated motion of the FPs sources (Liu et al. 2004). The separation between these sources increases as the LT sources rises exactly as expected from the drift of the reconnection upward along the middle stem (see Fig. 4) and excitation of larger overlying loops (Fig. 8, left panel).

Another interesting spatial evolution seen in the simple single loop limb are of 11/13/2003 is a systematic shift of the FP sources up along the legs of the loop towards an stationary LT source (Fig. 8, right panel). This drift starts first at lower energies then proceeds to higher energies, which could come about with a gradual increase of plasma density in the loop, presumably due to evaporation. We have shown that an order of magnitude increase in density moving upward with the sound (or slow magnetosonic wave) speed can describe the observations. This behavior also agrees with the general trend expected from the so called Neupert e_ect. It should however be noted that the Neupert e_ect is not present in all flares (Dennis & Zarro 1993) and a more accurate treatment of the effect in this are does not improve the correlation (see also Veronig et al. 2005). Thus, it seems that a more accurate HD treatment of this problem in required, which then can shed light on the response of the chromosphere to the energy input by PWT directly or via the accelerated particles (Liu et al. 2006).

Spectra and Their Evolution: In general, during the

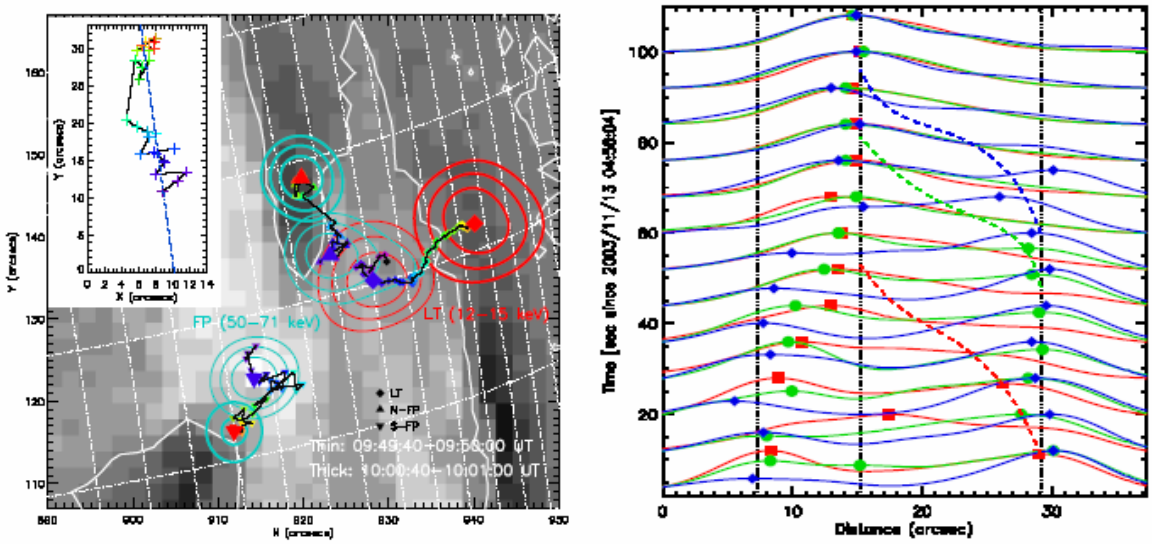

Fig.8. ***Left Panel****: Temporal evolution of HXR sources of a are observed by RHESSI on Nov. 3, 2003 over-plotted on an MDI magnetogram. The symbols indicate the source centroids and the colors show the time with a 20 second interval, starting from black (09:46:20 UT) and ending at red (10:01:00 UT) with contours at two different times indicated in the figure. The insert shows the relative positions of the N-FP with respect to the S-FP, which is fixed at the origin (Liu et al. 2004).* ***Right panel****: RHESSI observation of the evolution of the brightness profiles along the loop during the HXR peak of a are on Nov. 13 2003. The solid red, green, and blue curves show emission profiles at 12-15 keV, 15-20 keV and 20-30 keV, respectively. The corresponding dots show the loc al emission maxima. Their evolution suggests that FPs appear to move up and merge at the LT from low to high energies as depicted by the dashed lines (Liu et al. 2006).*

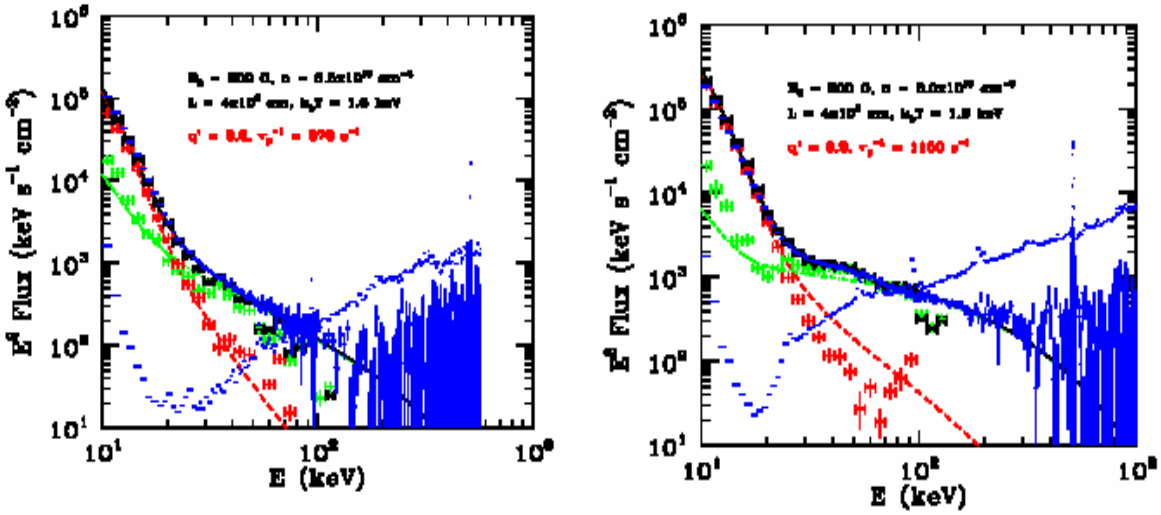

Fig.9. ***Left panel****: A fit to the total (black), FP (green) and LT (red) spectra of the first HXR pulse of the Sep. 20th 2002 are observed by RHESSI. Model parameters are indicated in the figure. The dashed and dotted lines are model spectra from equations (1) and (8) showing the presence of a quasi-thermal (LT) and a non-thermal (mostly FPs) component. The solid line gives the sum of the two. The blue dashes indicate the level of the background radiation (Petrosian et al. 2003). Right panel: Same as the left panel but for the second HXR peak. Note that compare with the model parameters for the first HXR pulse, both the gas density and the turbulence energy density increase during the second pulse, resulting more thermal emission and harder photon spectra.*

impulsive phase the spectra are dominated by a non-thermal component, with the LT always softer than the FPs, and sometimes there is a putative quasi-thermal component (mostly from the LT) that grows and becomes the dominant emission during the decay phase. This is in agreement with the general aspects of the electron spectra discussed above in connection with Figure 6, where it was shown that the SA model gives rise to both thermal and non-thermal components with softer spectra at the acceleration site or the LT and harder equivalent thick target spectra at the FPs. The relative strengths and spectra of these components and sources depend on the general parameters of the model. By adjusting the density, temperature, magnetic field, size and the turbulence spectrum and energy density, one can fit the observed LT and FP spectra. Figure 9 shows the observed and model spectra for the two HXR pulses of the Sept. 20, 2002 are which consisted of a single loop. The model parameters shown in the figure seem very reasonable. Note that the thermal component is more prominent and the FP spectra are harder during the second HXR pulse. This requires a higher gas density at the LT and a higher level of turbulence.

We have also found some inconsistency with the conventional models during the decay phase. In several limb flares we find that during the decay phase, when the non-thermal emission has all but disappeared, the (resolved) LT source continues to be confined; it does not extend to the FPs as one would expect if the evaporation fills the whole

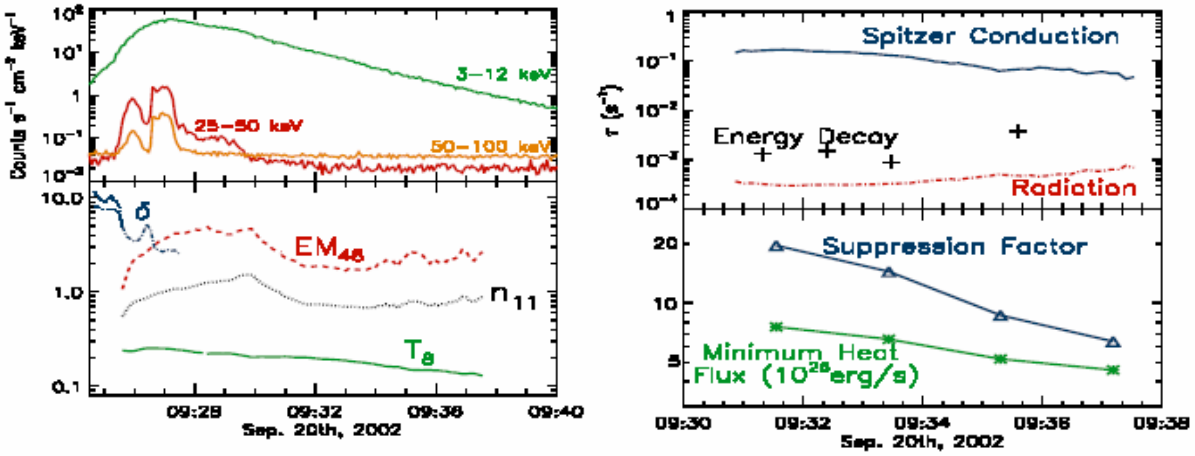

Fig.10. ***Left panel****: Light curve (upper panel) and spectral evolution of the Sep. 20, 2002 are. The total (LT+FPS) spectrum is fitted with a thermal plus a power-law mode. The lower panel shows the evolution of the spectral index δ, temperature T, emission measure EM, and density n. The preheating and early impulsive phases is dominated by a steep power law both for LT and FP (if any). The decay phase spectrum is dominated by the thermal LT source.* ***Right panel****: Top panel shows the observed energy decay rate and the calculated radiative cooling and Spitzer conduction rates. Bottom panle shows the required LT heating and suppression of conduction that can satisfy both the imaging and spectral evolution.*

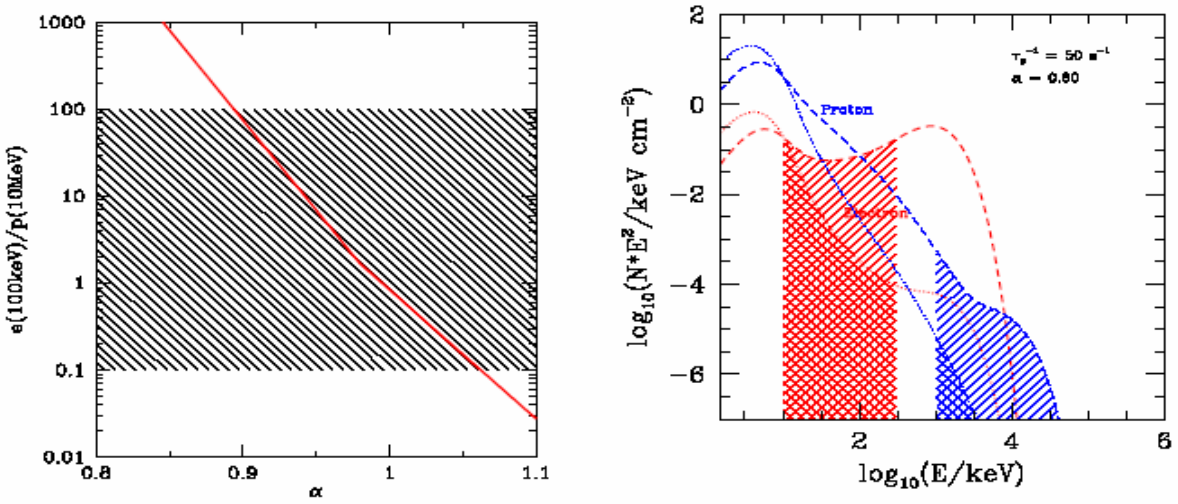

Figure 11: ***Left Panel****: Dependence of the ratio of the electron and proton flux density at 100 keV and 10 MeV, respectively, on the plasma parameter α. The shaded region corresponds to the observed region of some big flares where both fluxes were measured.* ***Right Panel****: Same as the right panel of Figure 6 except with different plasma parameter* $\alpha = \beta_{\rm A}^{-1}\delta^{1/2}$ *and* τ_p^{-1}*. All other parameters are the same. It shows clearly that electron acceleration is favored in strongly magnetized plasmas (with smaller values of α). See PL04 for details.*

loop with hot plasma. Figure 10 shows the temporal evolution of the temperature and emission measure of the thermal component and the spectral index of the non-thermal tail from spectral fitting, and the density from the observed source volume evolution for the 9/20/2002 are. The right panel shows that the observed energy decay rate is higher than the radiative cooling rate but much lower than the (Spitzer 1961) conduction rate. The latter discrepancy requires either suppression of the conduction and/or continuous energy input. The confinement of the LT source also requires a suppression of conduction in the LT region. We have shown (Jiang et al. 2006) that the observations require both energy input and suppression of the conduction (see lower portion of the right panel). PWT can be the agent for both. It can suppress the conduction rate by reducing the scattering mean free path, and can energized the plasma continuously during the decay phase (albeit at a low and diminishing rate). This behavior can be described as follows.

Because the acceleration time is proportional to the characteristic plasma time $\tau_p \propto \mathcal{W}_{\rm tot}^{-1}$, while the escape time behaves in the opposite manner, the relative strength of the quasi-thermal and non-thermal components seen in Figure 6 depends sensitively on the intensity Wtot of the PWT. For low Wtot, e.g. during the build up and decay phases, one gets only plasma heating with essentially no non-thermal component (see PL04 for details). This explains not only the postimpulsive decay phase behaviors described above but also the pre-impulsive SXR emission, during which the PWT being lower mainly heats the plasma without producing discernable non-thermal tails. This indicates that PWT play important role not only during the impulsive phase but are present before and continue to heat and confine the hot plasma in the LT regions well into the decay phase. In addition, the fact that harder spectra are obtained with higher levels of PWT can also explain the commonly observed soft-hard-soft evolution during the impulsive phase.

In Summary many of the radiative signatures of the electrons require the presence of the PWT and all observations are consistent with the general behavior expected with the basic scenario described in §2.

4.2 Relative Acceleration of Electrons and Protons

A second radiative signature of larger solar flares is the gamma-ray line emissions due to excitation of nuclear lines by the accelerated protons and ions. The SA model has been the working hypothesis here, stressed notably by Ramaty, Murphy, Share and collaborators. For these flares the ratio ofenergy of accelerated electrons to protons (in the shaded range of Fig. 6) ranges from 100 to 0.03 (Mandzavidze & Ramaty 1996) and is much larger in electron dominated flares. On the other hand, simple theoretical models, for example acceleration by Alfvén waves commonly used, favor acceleration of more protons and ions than acceleration of background thermal electrons. In PL04 we show that with a more complete treatment of the wave particle interaction, the number of accelerated protons in the observed energy range is reduced dramatically compared to that of electrons, and that the energy ratio is very sensitive to the plasma parameter $\alpha \propto n^{1/2}/B$ (Figure 11 left panel; also compare the hatched regions in the right panels of Figures 6 and 11). One consequence of this is that the proton acceleration will be more efficient in larger loops, where the B field is weaker, and at late phases, when due to evaporation n is higher. This can explain the offset of the centroid of the gamma-ray line emissions from that of HXRs seen by *RHESSI* (Hurford et al. 2003). It can also account for the observed delay of nuclear line emissions relative to HXR emissions seen in some flares (Chupp et al. 1990).

The result demonstrates how the characteristics of the accelerated particles|the relative acceleration of electrons and protons here|may be related to the properties of the background plasmas directly. This is one of the most powerful features of the SA acceleration model, which can

be used to infer the underlying high energy physical processes from the observed non-thermal emission.

4.3 Relative Acceleration of ^3He and ^4He

It is commonly believed that the observed abundance enrichment of high energy ions relative to their photospheric values favor a SA model (e.g. Mason et al. 1986 and Mazur et al. 1992). More recent observations have confirmed this picture (see Mason et al. 2000, 2002, Reames et al. 1994 and 1997, and Miller 2003). There are similarities and considerable differences among the spectra and abundances of different ions. One of the most vexing problems of SEPs has been the enhancement of ^3He in the so-called impulsive flares that sometimes can be 3 to 4 order ofmagnitude above the photospheric value. There has not been a satisfactory explanation for this phenomenon by the conventional treatment of the SA model or any other model of acceleration.

With a more complete treatment of ^3He and ^4He acceleration (in a manner similar to that of Fig. 6), Liu et al. (2004 and 2006) have demonstrated that SA by parallel propagating waves can solve this long standing problem. It is demonstrated that under certain reasonable conditions the model not only can account for the extreme enhancement of ^3He, but it can also reproduce the ^3He and ^4He spectra in several events with convex spectra (see Fig. 12, right). This is a major breakthrough in understanding of SEPs and may explain the acceleration of all charged particles in impulsive solar flares. Interestingly the high energy cutoff of the ^3He and ^4He He spectra are determined by the $k_{\min}$ of the PC branch and therefore the plasma parameter α. This, in combine with the dependence of the relative acceleration of electrons and protons on α, may lead several predictions that can be tested with future observations.

In summary, the radiative signatures of electrons and protons, and the spectra and abundances of the observed SEPs appear to require and are consistent with the basic ideas of §2.2.

5 Summary and Discussion

A significant fraction of information about distant astrophysical objects, especially those highly non-equilibrium systems, such as solar flares, AGNs, GRBs, Supernovae, is carried by non-thermal particles and the radiation produced by them. Understanding the origin of these non-thermal particles play an essential role in uncovering the underlying physics processes such as the acceleration mechanism, the energy release processes, and properties of the energized plasmas.

Turbulence is ubiquitous in the universe. When the Reynolds number of a system becomes much larger than one, turbulence develops, carrying an energy flow from the (large) generation scales, through an inertial range, and eventually reaching the (small) dissipation scales. The free energy associated with the large scale plasma motion and field fluctuations is converted into heat and production of non-thermal particles. In this paper we have argued that turbulence plays important roles in most of the astrophysical particle acceleration mechanisms and is likely the dominant energy transfer channel in solar flares, where the release of magnetic field energy via reconnection generates plasma wave turbulence, which consequently heats the plasma and accelerates most of the observed non-thermal electrons, protons, and ions via resonant wave-particle coupling. Understanding the details of wave-wave and wave-particle interactions that play major roles in all aspects of these process, is therefore very important.

An essential aspect of our approach is that we are interested in accelerating the thermal background plasma particles so that no injection of pre-energized particles is necessary. We have argued that SA of particles by plasma waves or turbulence is the most efficient mechanism under these circumstances. We review the cascade and damping of turbulent wave modes in the MHD regime. Obliquely propagating waves are damped at larger scales and dominate the plasma heating due to their strong coupling with the background particles via the TTD. The parallel propagating waves, on the other hand, can cascade freely to small scales and are mostly damped via the cyclotron-resonances. This suggests that waves propagating along the magnetic field line are the most important agents of accelerating the particles from the thermal background into a non-thermal tail. Ingeneral, one needs a self-consistent treatment of turbulence and particle acceleration theory valid from the

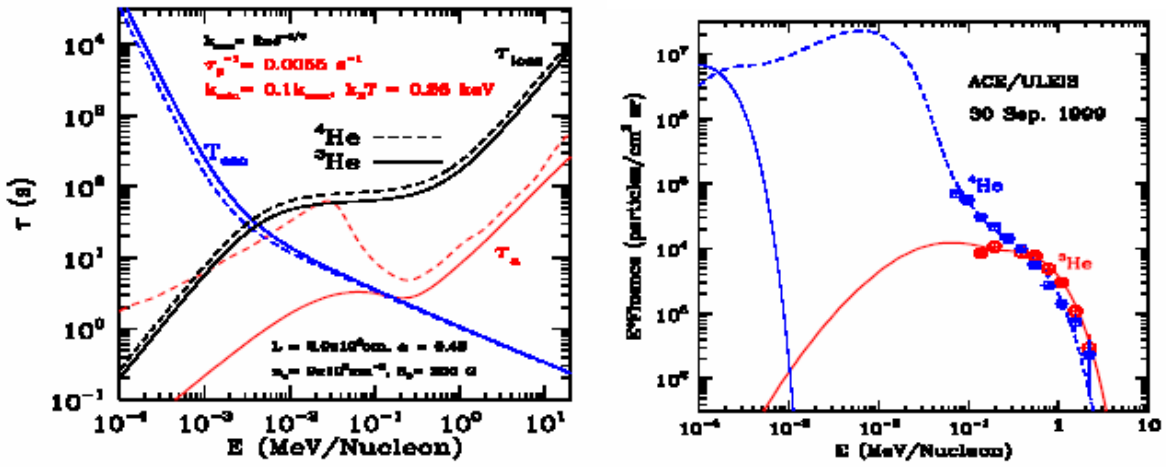

Fig.12. Same as Figure 6 but for the relative acceleration of 3He and 4He ions. The spectra flare for the escaping particles and the cutoff at a few MeV/nucleon is related to the $k_{\min}$ of the PC branch (See Liu et al. 2004, 2006).

MHD regime to the kinetic regime. However, we have argued that in most solar flares, where the total momentum of the non-thermal particles is less than that of the thermal background particles, the wave cascade and damping processes decouple from the non-thermal particle kinetic equation. In this case we use a power-law model for the spectrum of turbulence in the inertial range (from the wave generation to the dissipation scale) with sharp breaks beyond it. The cascade and thermal damping determine the characteristics of this broken power-law spectrum. This is then used to evaluate the diffusion coefficients and the spectrum of the non-thermal particles.

We demonstrate how the spectra and relative acceleration of different charge particles species depend on the temperature, density, magnetic field, size, and turbulence level of the flaring plasma with the last determined by the energy release rate of the are. The model successfully explains 1) the impulsive HXR emission from the LT source; 2) the breaks and cutoff of the electron spectrum in the impulsive phase; 3) the preheating observed in some flares and the confinement of the LT source and the slower than expected decay of the SXR emission in the decay phase; 4) the soft-hard- soft evolution pattern for most of the HXR pulses; 5) the relative acceleration of electrons and protons; and 6) the prominent enhancements of ^3He in some impulsive flares.

To simplify the model calculations, we assumed a cold and fully ionized background plasma and considered only the cases where damping by the thermal particles dominates. Thermal effects, such as the modification to the wave dispersion relation and the damping by different background particle species, need to be included self-consistently in a more complete treatment. Such a treatment in combine with a time-dependent approach is also required to address the plasma heating, which may have significantly implications on the heavy ion enrichments in impulsive solar flares. For large flares where non-thermal emission is prominent, one needs to take into account the damping by the non-thermal particles as well, which means that one needs to solve the coupled wave-particle kinetic equations for a complete treatment of the problem. The work was supported by NASA grants NAG5-12111, NAG5 11918-1, and NSF grant ATM- 0312344. The work performed by S. Liu was funded in part under the auspices of the U.S. Dept. of Energy, and supported by its contract W-7405-ENG-36 to Los Alamos National Laboratory.

APPENDIX

A BASIC EQUATIONS

In this section we describe some of the mathematical details required for investigation of the acceleration of all charged particles stochastically by turbulence and by shocks, their transport, and some of the electron radiation processes.

A.1 Particle Kinetic Equations

In strong magnetic fields, the gyro-radii of particles are much smaller than the scale of the spatial variation of the field, so that the gyro-phase averaged distribution of the particles depends only on four variables: time, spatial coordinate s along the field lines, the momentum p, and the pitchangle cosine μ. In this case, the evolution of the particle distribution, f(t; s; p; μ), can be described by the Fokker-Planck equation as they undergo stochastic acceleration (SA) by interaction with plasma turbulence (with diffusion coefficients D_{pp}; $D_{\mu\mu}$ and $D_{p\mu}$), direct acceleration (with rate $\dot{p}_G$), and suffer losses (with rate $\dot{p}_L$) due to other interactions with the plasma particles and fields:

$$\frac{\partial f}{\partial t}+v\mu\frac{\partial f}{\partial z}=\frac{1}{p^2}\frac{\partial}{\partial p}p^2\left[D_{pp}\frac{\partial f}{\partial p}+\right.$$
$$\left.+D_{p\mu}\frac{\partial f}{\partial \mu}\right]+\frac{\partial}{\partial \mu}\left[D_{\mu\mu}\frac{\partial f}{\partial \mu}+D_{\mu p}\frac{\partial f}{\partial p}\right]-$$
$$-\frac{1}{p^2}\frac{\partial}{\partial p}[p^2(\dot{p}_L-\dot{p}_G)f]+\dot{J}. \tag{10}$$

Here βc is the velocity of the particles and $\dot{J}$ is a source term, which could be the background plasma or some injected spectrum of particles. The effect of the magnetic field convergence or divergence can be accounted for by adding $(c\beta\mathrm{d}\ln B/2\mathrm{d}s)\partial\left[(1-\mu^2)f\right]/\partial\mu$ to the right hand side.

Pitch-angle isotropy: At high energies and in weakly magnetized plasmas with the Alfvén velocity $\beta_A\equiv v_A/c\ll 1$ the ratio of the energy and pitch angle diffusion rates $D_{pp}/p^2D_{\mu\mu}\approx(\beta_A/\beta)^2\ll 1$, and one can use the *isotropic approximation* which leads to the *Diffusion-Convection Equation* (see e.g. Dung & Petrosian 1994 or Kirk et al. 1988):

$$\frac{\partial F}{\partial t}-\frac{\partial}{\partial z}\kappa_1\frac{\partial F}{\partial z}=pv\frac{\partial\kappa_2}{\partial z}\frac{\partial F}{\partial p}-$$
$$-\frac{1}{p^2}\frac{\partial}{\partial p}\left(p^3v\kappa_2\frac{\partial F}{\partial z}\right)+\frac{1}{p^2}\frac{\partial}{\partial p}\left[p^4\kappa_3\frac{\partial F}{\partial p}-\right.$$
$$\left.-p^2(\dot{p}_L-\dot{p}_G)F\right]+Q(z,t,p)\,, \tag{11}$$

where

$$F(z,t,p)\equiv\frac{1}{2}\int_{-1}^{1}\mathrm{d}\mu f(\mu,z,t,p),$$
$$\dot{S}(z,t,p)\equiv\frac{1}{2}\int_{-1}^{1}\mathrm{d}\mu\dot{J}(\mu,z,t,p), \tag{12}$$

and

$$\kappa_1=\frac{v^2}{8}\int_{-1}^{1}\mathrm{d}\mu\frac{(1-\mu^2)^2}{D_{\mu\mu}}\,,$$
$$\kappa_2=\frac{1}{4}\int_{-1}^{1}\mathrm{d}\mu(1-\mu^2)\frac{D_{\mu p}}{D_{\mu\mu}}p^{-1}\,,$$
$$\kappa_3=\frac{1}{2}\int_{-1}^{1}\mathrm{d}\mu\left(D_{pp}-\frac{D_{\mu p}^2}{D_{\mu\mu}}\right)p^{-2}\,.$$

At low energies, as shown by Pryadko & Petrosian (1997), specially for strongly magnetized plasmas $(\alpha\ll 1)$, $D_{pp}/p^2\gg D_{\mu\mu}$, SA will be more efficient

than acceleration by shocks. In this case the pitch angle dependence may not be ignored, and we have

$$\frac{\partial f^\mu}{\partial t} + v\mu\frac{\partial f^\mu}{\partial z} = \frac{1}{p^2}\frac{\partial}{\partial p}p^2 D^\mu_{pp}\frac{\partial f^\mu}{\partial p} - \\ - \frac{1}{p^2}\frac{\partial}{\partial p}[p^2(\dot{p}_L - \dot{p}_G)f^\mu] + \dot{J}^\mu , \tag{13}$$

However, in our most recent study of this situation (PL04), we find that these dependences flare in general weak and one can average over the pitch angles. Furthermore, for solar are conditions

$$(n \sim 10^{10}\mathrm{cm}^{-3},\ B \sim 100\ \mathrm{G},\ L \sim 10^9\ \mathrm{cm})$$

Coulomb scatterings dominate and isotropize the distribution at low energies.

Spatial Homogeneity: If the acceleration region is homogeneous (i.e. $\partial/\partial s$ terms $\rightarrow$ 0), or if we are interested in spatially integrated results, then we can ignore the space gradient terms (or integrate equation [11] or [13] over z and μ), and describe the spatial diffusion by an escape term we obtain the well-known equation

$$\frac{\partial N}{\partial t} = \frac{\partial}{\partial E}(D_{EE}\frac{\partial N}{\partial E}) + \frac{\partial}{\partial E}[(A - \dot{E}_L)N] - \frac{N}{T_{\mathrm{esc}}} + \dot{Q},$$

whith

$$T_{\mathrm{esc}} = T_{\mathrm{cross}}(1 + T_{\mathrm{cross}}/\tau_{\mathrm{scat}}) , \tag{14}$$

where N(E; t) and $\dot{Q}$(E; t) are the total numbers of the accelerated particles and the source, and the escape time T_{esc} is defined to account for the possibilities of τ_{scat} less or greater than T_{cross} = L / υ, time for particle to cross freely an acceleration site of size L. The pitch angle averaged acceleration coefficient κ_3 can also be defined similarly (see PL04). Thus, it turns out that this most commonly used transport equation in astrophysical problems is a good approximation except for very strongly magnetized plasmas (α <<1).

A.2 Fokker-Planck Coefficients and the Dispersion Relation

It is clear that the determination of the coefficients in the above equations is an essential part of the task in determining the accelerated particle spectrum. For this we need the characteristics of the waves or turbulence.

Waves in a plasma are described by the dispersion relation. In a fully ionized (hydrogen and 10% He by number) but cold plasma this relation is given by

$$\tan^2\theta = \frac{-P(n_r^2 - R)(n_r^2 - L)}{(Sn_r^2 - RL)(n_r^2 - P)}, \tag{15}$$

where

$$S = \frac{1}{2}(R + L), \qquad D = \frac{1}{2}(R - L),$$

$$P = 1 - \sum_i \frac{\omega_{pi}^2}{\omega^2},$$

$$R = 1 - \sum_i \frac{\omega_{pi}^2}{\omega^2}\left(\frac{\omega}{\omega + \epsilon_i\Omega_i}\right),$$

$$L = 1 - \sum_i \frac{\omega_{pi}^2}{\omega^2}\left(\frac{\omega}{\omega - \epsilon_i\Omega_i}\right),$$

$$\omega_{pi}^2 = \frac{4\pi n_i q_i^2}{m_i}, \qquad \Omega_i = \frac{|q_i|B}{m_i c},$$

$$\epsilon_i = \frac{q_i}{|q_i|}.$$

Here θ is the wave propagation angle with respect to the large scale magnetic field, $n_r = kc/\omega$ the refractive index, and n_i, q_i, and m_i are the density, charge, and mass of the background particles (electron, proton and α particle), respectively. In most studies one considers waves propagating at a particular angle (commonly with θ = 0, and sometimes θ=π/2), in which case this expression simplifies and can be described by a few curves (standing for different modes) in the ω-k plane. In general, this relation is described by several surfaces (ω as a function of $k_\perp = k\sin\theta$ and $k_\parallel = k\cos\theta$) as shown in Figure 1. The particles couple strongly with waves when the resonance condition is satisfied:

$$\omega = k_\parallel v\mu + n\Omega_i/\gamma, \tag{16}$$

where γ is the the Lorentz factor and n stands for the harmonic number. This condition is indicated by the titled surfaces in the Figure 1 for n = 0 and 1. The intersection curves [*say* $k_{res}(\theta)$] of these surfaces with the dispersion surfaces satisfy the resonance condition. Only waves with such k and θ contribute to the Fokker-Planck coefficients. In general one can write [5]

$$D_{ij}(p,\mu) = \sum_l \int \sigma_{ij}^l(p,\mu,\mathbf{k}_{res}^l(\theta)) \\ W(\mathbf{k}_{res}^l(\theta))\mathrm{d}\theta, \tag{17}$$

where l represents different dispersion surfaces, and the integral is performed along the resonance lines $\mathbf{k}_{res}^l(\theta)$. For parallel propagating waves, the integral becomes a sum over a few resonant wave modes (Dung & Petrosian 1994). The pitch-angle averaged energy diffusion coefficient D_{EE} and the direct acceleration rate A_{sa} due to turbulence are then given by

[5] Here σ_{ij}^i stands for the wave-particle interaction rate which in general are sums of Bessel functions (see e.g. Jaekel & Schlickeiser 1992).

$$D_{EE} = \frac{E^2}{2}\int_{-1}^{1} \mathrm{d}\mu \left(\frac{D_{pp}}{p^2} - \frac{D_{\mu p}^2}{p^2 D_{\mu\mu}} \right), \qquad (18)$$

$$A_{SA} = \frac{\mathrm{d}\beta\gamma^2 D_{EE}}{\beta\gamma^2 \mathrm{d}E},$$

which means that the rate $\sum$ introduced in §2.1 is related to σ similarly, $\Sigma = \mathrm{d}\beta\gamma^2\sigma/\beta\gamma^2\mathrm{d}E$. The acceleration and all other rates are proportional to the inverse of the characteristic **PWT** timescale

$$\tau_p^{-1} \propto \Omega(\mathcal{W}/B^2) \qquad (19)$$

$$\mathcal{W} = \int \mathrm{d}^3 k W(\mathrm{k})$$

where is the total energy density of turbulence.

A.3 Particle Transport and Radiation

Solution of equation (14) gives the spectrum of the particles integrated over the acceleration (or turbulent) site (N) and the spectrum of particles escaping this site along open and closed field lines away and toward the chromosphere with a nearly isotropic pitch angle distribution (N/T_{esc}). The particles at the acceleration site which we identify with the loop top (LT) source interact with the background plasma and field and produce the LT emission. The escaping particles undergo further scattering and energy losses as they travel along the field lines. These transport effects are treated by an equation very similar to equation (10). However, most high energy particles lose bulk of their energy below the chromosphere within a short scale height. For these one can calculate the integrated thick target foot-point (FP) emission.

The observed hard X-ray spectrum of a solar are is a "convolution" of the non-thermal electron energy spectrum $\overline{N(E)}$ and the bremsstrahlung cross section $\sigma_b(k,\mathrm{E})$.

$$J(k) = \int_k^\infty nv\overline{N}(E)\sigma_b(k,E)\mathrm{d}E\,. \qquad (20)$$

For a **Thin Target** emission at the LT, $\bar{N} = N(E)$, N = N(E), the spectrum of the accelerated electrons.

On the other hand, for the **Thick Target** FP source $\overline{N}(E) = \dot{E}_L^{-1}\int_E^\infty N(E)/T_{\mathrm{esc}}\mathrm{d}E$. The last equality is for the SA model of equation [14] where the injected flux of particles is equal to the escaping flux from the acceleration site. The loss rate $\dot{E}_L$ for the nonrelativisitic electrons due to Coulomb collisions, is proportional to n: $\dot{E}_{\mathrm{L}} = 4\pi r_0^2 \ln\Lambda nmc^3/\beta$, where lnΛ is the Coulomb logarithm and $r_0 = e^2/m_e c^2$ is the classical electron radius. The total spectrum is obtained from the above equation with

$$\overline{N}(E) = N(E) + \frac{1}{\dot{E}_{\mathrm{L}}}\int_E^\infty \frac{N(E')}{T_{\mathrm{esc}}(E')}\mathrm{d}E'\,. \qquad (21)$$

The most common practice is to compare with observation the total photon model spectra and determine the best fit model $\overline{N(E)}$. There have, however, been several attempts of deriving the electron spectra by the "deconvolution" of the observed photon spectra (see e.g. Johns and Lin 1992). More recently, Kontar et al. (2004) have used generalized regularization techniques to deconvolve the observed photon spectrum J(k) for a given cross section σ(k;E) to obtain the volume integrated electron spectrum $\bar{N}(E)$.

Yohkoh and *RHESSI* observations have made abundantly clear that there may be several sources contributing to the observed X-ray spectrum. In simple flares one has a loop top (LT) and two footpoint (FP) sources. Consequently the relation between deconvolved spectrum $\bar{N}(E)$ and accelerated spectrum N(E) is complicated in principle this integral equation can be converted to a differential equation and solve for N. After some algebra one gets

$$\frac{\mathrm{d}(N/v)}{\mathrm{d}E} - \frac{1}{\dot{E}_{\mathrm{L}}T_{\mathrm{esc}}}\frac{N}{v} = \frac{\mathrm{d}(\overline{N}/v)}{\mathrm{d}E}, \qquad (22)$$

which has the formal solution

$$N(E) = \overline{N}(E) - v\int_{\eta(E)}^\infty \frac{\overline{N}}{v'}e^{\eta-\eta'}\mathrm{d}\eta'\,, \qquad (23)$$

$$\mathrm{d}\eta = \frac{\mathrm{d}E}{\dot{E}_{\mathrm{L}}T_{\mathrm{esc}}}\,.$$

Accelerated particle on open lines escape the Sun and reach the Earth where their spectra can be measured by space instruments. With our results we can determine the spectrum of these particles as well, which can then be compared with observations. As stated in § 2 we have carried such comparisons for ^3He and ^4He spectra. We can carryout similar calculations for other elements, specifically the electrons, where recent combined study of solar X-rays and SEP electrons show some discrepancies with the results from simple analysis (Krucker et al. 2004). The above formalism can be used to address this puzzle. This will also be very helpful to understand the correlation between the energetic electron events and ions in SEPs (Krucker et al. 1999, 2000; Ho et al. 2001; Wang et al. 2004, 2005).

We also note that there are other transport effects, which may be crucial to explain some of the observed are characteristics. For example, the electron flux from the LT to the FPs will induce an electric field that can both drive a return current and decelerate the injected non-thermal electrons, which may make the low-energy cutoff of the electron spectrum commonly invoked in model fitting of the observed photo spectra unnecessary and account for the broken power-law photon spectra observed in many flares (Holman et al. 2003). It also has the potential to explain the dominance of loop legs at intermediate energies observed during some intervals in the impulsive phase of a few flares (Liu et al. 2006).

REFERENCES

[1] André, M. 1985, J. *Plasma Phys*., 33, 1
[2] Biskamp, D. 1995, *Chaos, Solutions and Fractals*, 5, 1779
[3] Biskamp, D. 2000, *Magnetic Reconnection in Plasmas*, CUP

[4] Biskamp, D. 2003, *Magnetohydrodynamic Turbulence*, CUP
[5] Biskamp, D., Schwarz, E., Zeiler, A., Celani, A., & Drake, J. 1999, *Phys. of Fluids*, 6(3), 751
[6] Boris, J. P., Dawson, J. M., Orens, J. H., & Roberts, K. V. 1970, *Phys. Rev. Lett.*, 25, 706
[7] Cho, J., & Lazarian, A. 2002, Phys. Rev. Lett., 88, 245001; CL02
[8] Cho, J., & Lazarian, A. 2003, M.N.R.A.S., 345, 325; CL03
[9] Cho, J., & Lazarian, A. 2004, Ap. J. (*Letters*), 615, 41
[10] Cho, J., & Lazarian, A. 2006, Ap. J., in press; astro-ph/0509385
[11] Cho, J., Lazarian, A., & Vishniac, E. T. 2003, in *Turbulence and Magnetic Fields in Astrophysics*, Lecture Notes in Physics, eds, Falgarone, E., Passot, T., chapter "Scaling laws and Astrophysical Implications", p. 56
[12] Dennis, B. R., & Zarro, D. M. 1993, *Solar Phys*., 146, 177
[13] Dingus, B. L. et al. 1994, AIP Conf. Proc. eds. J. M. Ryan & W. T. Vestrand, 294, 177
[14] Dung, R., & Petrosian, V. 1994, Ap. J., 421, 550
[15] Fletcher, L., & Martens, P. C. H. 1998, Ap. J., 505, 418
[16] Goldreich, P., & Sridhar, S. 1995, Ap. J., 438, 763; GS95
[17] Hamilton, R. J. & Petrosian, V. 1992, Ap. J., 398, 350
[18] Higdon, J.C. 1984, Ap. J., 285, 109
[19] Ho, G. C. et al. 2001, Ap. J., 552, 863
[20] Holman, G. D. 1985, Ap. J., 293, 584
[21] Holman, G. D. 1996a, BAAS, 28, 939
[22] Holman, G. D. 1996b, AIP Conf. Proc. eds. R. Ramaty et al., 374, 479
[23] Holman, G. D. 1996, AIP Conf. Proc. eds. R. Ramaty et al., 374, 479
[24] Holman, G. D., Sui, L. H., Schwartz, R. A., & Emslie, A. G. 2003, ApJ, 595, 97
[25] Hurford, G. J. et al. 2003, Ap. J. (*Letters*), 595, L77 Jaekel & Schlickeiser 1992, Annales Geophysicae, 10, 541
[26] Jiang, Y. W. et al. 2006, Ap. J., 638, 1140; astro-ph/0508532
[27] Jokipii, R. J. 1987, ApJ, 313, 842
[28] Jones, F. C. 1994, Ap. J. *Suppl*., 90, 561
[29] Kirk, J. G., Schlickeiser, R. & Schneider, P. 1988, Ap. J., 328, 269
[30] Krucker, S. et al. 1999, Ap. J., 519, 864
[31] Krucker, S., & Lin, R. P. 2000, Ap. J. (*Letters*), 542, L61
[32] Krucker, S., Kontar, E. P., & Lin, R. P. 2004, AGU, #SH13A-1129
[33] Lazarian, A. & Vishniac, E. & Cho, J. 2004, Ap. J., 603, 180
[34] Lin, R. P., & Schwartz 1987, ApJ, 312, 462
[35] Lithwick, Y., & Goldreich, P. 2001, Ap. J., 562, 279
[36] Lithwick, Y., & Goldreich, P. 2003, Ap. J., 582, 1220
[37] Litvinenko, Y. E. 2003, *Solar Phys*., 212, 379
[38] Liu, S., Petrosian, V., & Mason, G. 2004, Ap. J. (*Letters*), 613, L81; LPM04
[39] Liu, S., Petrosian, V., & Mason, G. 2006, Ap. J., 636, 462; LPM06
[40] Liu, W. et al. 2003, SPD, 34, 1802
[41] Liu, W. et al. 2004, Ap. J. (*Letters*), 611, L53
[42] Liu, W. et al. 2006, astro-ph/0603510
[43] Marschhäuser, H. et al. 1994, AIP Conf. Proc. eds. J. M. Ryan & W. T. Vestrand 294, 171
[44] Mason, G. M., Reames, D. V., Klecker, B., Hovestadt, D., & von Rosenvinge, T. T. 1986, Ap. J., 303, 849
[45] Mason, G. M., Dwyer, J. R., & Mazur, J. E. 2000, Ap. J. (*Letters*), 545, L157
[46] Mason, G. et al. 2002, Ap. J., 574, 1039
[47] Masuda, S. et al. 1994, *Nature*, 371, 495
[48] Masuda, S. 1994, University of Tokyo, Ph.D. Thesis
[49] Mazur, J. E. et al. 1992, Ap. J., 401, 398
[50] Matthaeus, W. H., & Brown, M. R. 1988, *Phys. Fluids*, 31 (12), 3634
[51] Matthaeus, W.H., Ghosh, S., Oughton S., Roberts, D.A. 1996, *J. Geophys. Res.*, 51, 1484
[52] McTiernan, J. M. et al. 1993, Ap. J. (*Letters*), 416, L91
[53] Miller, J. A. 2003, Multi-Wavelength Observations of Coronal Structure and Dynamics eds. Petrus
[54] C.H. et al. (COSPAR Colloquia Series Vol. 13, 387
[55] Miller, J. A., LaRosa, T. N., & Moore, R.L. 1996, Ap. J., 445, 464
[56] Miller, J. M. & Reames, D. V. 1996, AIP Conf. Proc. eds. R. Ramaty et al., 374, 450
[57] Neupert, W.M. 1968, Ap. J. (*Letters*), 153, L59
[58] Norlund, A. et al. 1992, Ap. J., 392, 647
[59] Park, B. T., Petrosian, V., & Schwartz, R. A. 1997, Ap. J., 489, 358; PPS
[60] Passot, T., Pouquet, A., & Woodward, P. 1988, *Astr. & Astrophys*., 197, 228
[61] Petrosian, V., & Donaghy, T. Q. 1999, Ap. J., 527, 945
[62] Petrosian, V., Donaghy, T. Q., & McTiernan, J. M. 2002, Ap. J., 569, 459
[63] Petrosian, V., Liu, S., Liu, W., & Jiang, Y. 2003, ACE/RHESSI/WIND workshop at Taos, NM.
[64] Petrosian, V., & Liu, S. 2004, Ap. J., 610, 550; PL04
[65] Petrosian, V,, Yan, H. & Lazarian, A. 2006, Ap. J., , In press; astro-ph/0508567; PYL06
[66] Pouquet, A., Frish, U.,& L_eorat, J. 1976, *J. Fluid Mech*., 77, 321
[67] Priest, E. & Forbes, T. 2000, *Magnetic Reconnection*, CUP
[68] Pryadko, J., & Petrosian, V. 1997, Ap. J., 482, 774
[69] Pryadko, J., & Petrosian, V. 1998, Ap. J., 495, 377
[70] Pryadko, J., & Petrosian, V. 1999, Ap. J., 515, 873
[71] Reames, D. V., Meyer, J. P., & von Rosenvinge, T. T. 1994, *Ap. J. Suppl*., 90, 649
[72] Reames, D. V. et al. 1997, Ap. J., 483, 515
[73] R onnmark, K. 1983, *Plasma Phys*., 25, 669
[74] Shay, M., Drake, J. Swisdak, M., & Rogers, B. 2004, 35th COSPAR Scienti_c Assemply, p. 2390
[75] Shebalin, J. V., Matthaeus, W. H., & Montgomery D. C. 1983, *J. Plasma Phys*., 29, 525
[76] Spitzer, L. Jr. 1961, *Physics of Fully Ionized Gases* (New York: John Wiley & Sons)
[77] Sui, L., & Holman, G. D. 2003, Ap. J. (*Letters*), 596, L251
[78] Swanson, D. G. 1989, *Plasma Waves* (New York: Academic Press)
[79] Tsuneta, S. 1985, Ap. J., 290, 353
[80] Veronig, A. M. et al. 2005, Ap. J., 621, 482
[81] Wheatland, M.S. & Melrose, D.B. 1995, *Solar Phys*., 158, 283
[82] Wang, L., Lin, R. P., Krucker, S., & Mason, G. M. 2005, AGU #SH33A-01
[83] Wang, L., Mason, G. M., Lin, R. P., & Krucker, S. 2004, AGU #SH31A-1153
[84] Zhou, Y., & Matthaeus, W.H. 1990, J. *Geophys*. Res., 95, 14881

Highlights of the October - November 2003 Extreme Events

N. Gopalswamy

NASA Goddard Space Flight CenterGreenbelt MD 20771 USA, n_gopalswamy@yahoo.com

There was a high concentration of coronal mass ejections (CMEs), X-class soft X-ray flares, solar energetic particle (SEP) events, and interplanetary shocks observed during the episode the late October and early November 2003 period. The CMEs were very energetic and the consequences were also unusually intense. These extreme properties were commensurate with the size and energy of the associated active regions. This study suggests that the speed of CMEs may not be much higher than ~3000 km/s, consistent with the large free energy available in the associated active regions. The observations indicate that the CMEs may not have speeds much higher than ~ 3000 km/s implying that the Sun-Earth travel times of CME-driven shocks may not be less than ~0.5 day. Some of the CMEs were both geoeffective and SEPeffective, which are the most important from a space weather point of view.

Introduction

An extreme event is considered to be profoundly unique either in its occurrence or in its consequences. The October - November 2003 solar eruptive events (also known as the Halloween storms) qualify as extreme events on both counts: source properties at the Sun and their heliospheric consequences. Several aspects of theses events including active region size and potential energy flare occurrence rate and peak intensity, coronal mass ejection (CME) speed and energy, shock occurrence rate, SEP occurrence rate and peak intensity, and the geomagnetic storm intensity displayed extreme behavior. This period witnessed a high concentration of energetic eruptions including two CMEs that attained the level of a handful of historical events with an extremely short (less than a day) Sun-Earth shock transit time. The plasma, particle and electromagnetic consequences of the Halloween eruptions were observed not only in geospace but also at various locations in the heliosphere, thanks to the distributed array of space and ground based observatories that were available for observation. It was possible to compare the Halloween events with the rest of the events observed over the whole solar cycle to assess the severity of solar eruptions one should expect. For example, the Sun-Earth travel time of CME-driven shocks may not be less than about half a day. This paper highlights some of the key results obtained by analyzing the October-November 2003 CMEs originating from three solar active regions.

Overview

The October-November 2003 eruptions originated from three active regions, with NOAA numbers 484, 486, and 488. The white light image obtained on 2003 October 27 shows the relative locations of these events (see Fig.1). AR 484 and 488 were in the northern hemisphere, while AR 488 was in the southern hemisphere. The three regions produced a set of 143 well-observed flares (54 from AR 484; 60 from AR 486; 29 from AR 488). There were at least 80 CMEs during the two week period, most of them originating from the three active regions. AR 486 was the most prolific producer of CMEs, with the eruptions starting when it was behind the east limb. It continued to produce eruptions during disk passage and even behind the west limb. AR 488 emerged during the study period. The flares from AR 484 were observed between 18 and 26 October and returned as AR 501 to produce more energetic eruptions. The active regions were very big, with areas among the highest during solar cycle 23. The flare recurrence times were only a few hours (~4 h), while the CME recurrence time was a bit longer (~10 h).

Figure 2 provides an overview of flares, CMEs, SEP intensity, solar wind speed, and Dst index over an one-month interval in October and November 2003. The flare activity was very intense with the background intensity in GOES soft X-rays exceeding C1.0 level. The soft X-ray flux dropped dramatically when AR 486 rotated behind the west limb during early November 2003. The high concentration of CMEs is revealed by the height-time plots from the Solar and Heliospheric Observatory (SOHO) mission's Large Angle and Spectrometric Coronagraph (LASCO). There were a large number of halo CMEs (indicated by the solid lines in the height-time plots). The SEP intensity is plotted from GOES data in the >10 MeV channel. The intensity remained above the storm level (10 particle flux units) for about two weeks, representing a long interval of radiation hazard in the near-Earth space environment. The solar wind speed measured by the ACE spacecraft shows that the solar wind speed was close to an unprecedented 2000 km/s (see also Skoug et al., 2004). The Dst index shows three super-intense storms, the first two occurring around the time of very high solar wind speed and the third one occurring on

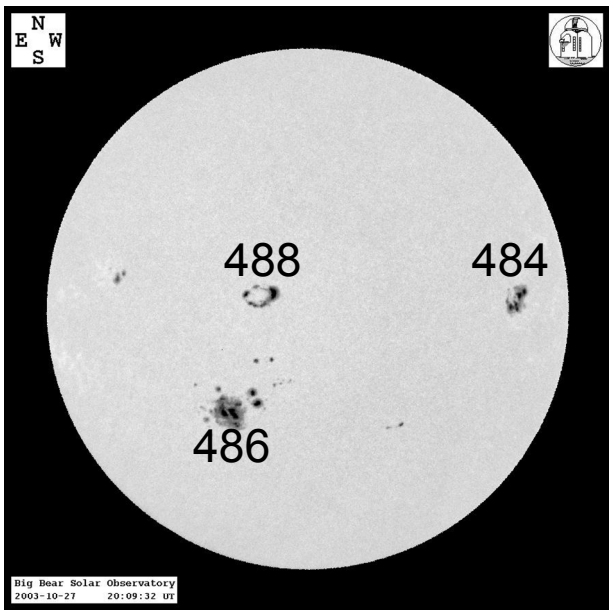

Fig.1. White-light image of the Sun showing the three active regions of interest (AR484, 488, and 486) taken on 2003 October 27 at 20:09 UT at the Big Bear Solar Observatory.

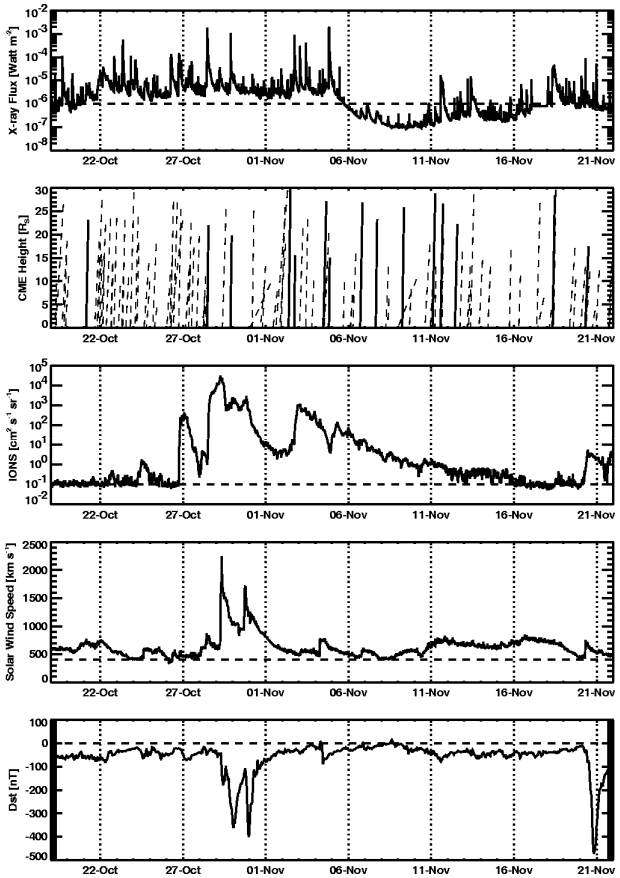

Fig.2. Overview plots (from top to bottom) of solar activity (GOES X-ray flares; CME height-time plots) and the heliospheric consequences (SEP intensity, solar wind speed, and Dst index). The horizontal dashed lines in each plot refer to approximate quiet conditions (GOES X-ray plot shows the C1.0 level; 0.1 pfu in the SEP plot; 400 km/s in solar wind speed; 0 nT in Dst index). The solid and dashed lines in the CME height-time plots represent halo and non-halo CMEs, respectively (from Gopalswamy et al., 2005b). The largest geomagnetic storm of the cycle occurred when AR 484 returned as AR 501 (see Gopalswamy et al. 2005a for details).

November 20, 2003. The last storm happens to be the largest storm of the cycle, associated with AR 501 (see Gopalswamy et al. 2005a for details).

The intensity of SEPs was so high that instruments on board the SOHO such as CDS (Coronal Diagnostic Spectrometer) and UVCS (UltraViolet Coronagraph Spectrometer) had to stop making observations and turn off the high voltage supply. Both instruments returned to normal observations two days later. The onslaught of SEPs resulted in severe degradation of white light and EUV images (the so-called "snowstorm"), making it difficult to detect new CMEs. The SEP event on October 28, 2003 resulted in significant ozone depletion between 50 and 80 km from the ground (Jackman et al. 2005). Awareness of the storms prompted safety measures to be taken for most of the space assets. About 59% of the reporting spacecraft and about 18% of the onboard instrument groups were affected by the Halloween SEP events (Barbieri and Mahmot, 2004). Electronic upsets, housekeeping and science noise, proton degradation to solar arrays, changes to orbit dynamics, high levels of accumulated radiation, and proton heating were observed. Most earth-orbiting spacecraft were put into safe mode to protect from the particle radiation.

Major impact also occurred on the society: about 50,000 people in southern Sweden (Malmoe) experienced a blackout, where the oil in a transformer heated up by 10 degrees. Surge currents were also observed in Swedish pipelines. Several occurrences of degradation and outage of GPS systems were reported. Interference in high-frequency radio communications were felt by several teams on Mount Everest. When the storms arrived at Mars, the MARIE instrument on board Mars Odyssey succumbed to the onslaught of radiation. The storms continued to the orbits of Jupiter and Saturn as detected by Ulysses and Cassini, respectively. Finally, the disturbances reached Voyager 2 after about 180 days, piled up together as a single merged interaction region (MIR), which led a large depression in cosmic ray intensity, lasting more than 70 days (Burlaga et al. 2005).

Because of the large armada of observing facilities available on ground and in space, a wealth of data has been accumulated on the October-November 2003 events. A first set of more than 70 scientific papers have already appeared in Journal of Geophysical Research (Space Physics), Geophysical Research Letters and Space Weather (see Gopalswamy et al. 2005a for a list of these papers). Further analysis is needed for obtaining a complete picture of the Halloween events. In the following we discuss mainly issues related to CMEs in the inner heliosphere.

CMEs

Figure 3 shows the daily CME rate and mean speed averaged over Carrington rotation periods from 1996 to the end of 2005. The CME rate had fallen to ~2 per day just before the Halloween CMEs and then increased to ~3.7 per day. Such local activity maxima are due to the passage of some very active ARs with copious production of CMEs. The Halloween spike in the CME rate is not spectacular compared to the two later spikes, but the corresponding peak in the CME mean speed is the largest one, thus distinguishing it as an extreme event.

There were 80 CMEs during Halloween period. This is much smaller than the 143 flares observed during the same interval. The actual number of CMEs is expected to be larger because some narrow CMEs originating from close to the disk center are not likely to be observed by the coronagraphs (see Gopalswamy et al., 2001a; Yashiro et al.,

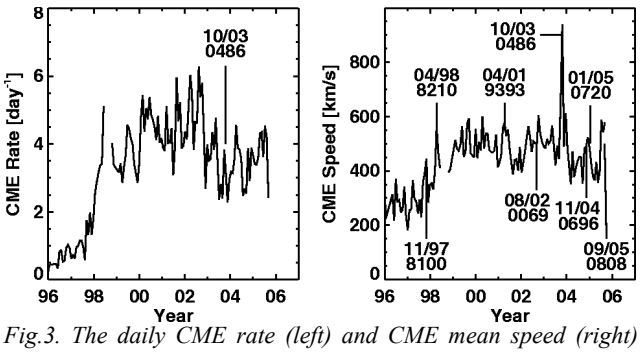

Fig.3. The daily CME rate (left) and CME mean speed (right) averaged over Carrington rotation periods from 1996 to the end of 2005. The peak in CME rate corresponding to the Halloween events is indicated by an arrow. The month and NOAA numbers of some CME-productive active regions are marked in the speed plot. The October 2003 period stands out, mainly contributed by AR 486.

Table 1. Comparison between the 2003 October November extreme events with the general population of CMEs observed until the end of 2003.

CME Property	Halloween CMEs	All CMEs
Average speed (km/s)	878	480
Average width (deg.)	50	47
Average mass ($x10^{14}$ g)	15	6.7
Average kinetic energy ($x10^{29}$ erg)	44	5.4
Fraction of wide CMEs (%)	48	37
Fraction of full halos (%)	12	3
Fraction > 900 km/s CMEs (%)	36	7
Fraction of >2000 km/s CMEs (%)	9	0.3
Fraction of fast and wide CMEs (%)	25	4
Fraction of CMEs with SEPs (%)	8	0.7
Fraction SEP events with GLEs (%)	50	25
Fraction of CMEs with DH type II	16	2.5
Fraction of CMEs with metric type II	21	10
Fraction of CMEs with mkm type II	8	0.8

2005). Most of the CMEs originated from the three active regions (ARs 484, 486, and 488). The Halloween CMEs clearly stand out when compared with the general population. Table 1 compares the properties of the general and Halloween populations. The Halloween CMEs were fast and wide on the average and hence were very energetic. There were 8 ultra-fast CMEs (speed ≥ 2000 km/s) during the Halloween period, compared to 37 over the entire cycle 23. The rate of full-halo CMEs was nearly four times the average rate during cycle 23. At least 19 shocks were observed near the Sun, while eight of them were intercepted by spacecraft along the Sun-Earth line. The Halloween CMEs were highly geoeffective: the resulting geomagnetic storms were among the most intense of cycle 23. The CMEs were associated with very large SEP events, including the largest event of cycle 23.

The Halloween CMEs contained a large fraction (12%) of full halo CMEs compared to the general population (3%). About half (48%) of the Oct/Nov 03 CMEs were wide events (width > 60^o), while only 37% of the general population were so wide. The masses were also accordingly higher, with a median value of $2.4x10^{15}$ g. This is more than 3 times larger than the median mass of the general population. The average kinetic energy of the Halloween CMEs was $4.5x10^{30}$ erg, which is an order of magnitude higher than the corresponding value ($5.2x10^{29}$ erg) for the general population. Thirteen CMEs had kinetic energy exceeding 10^{32} erg: 10 from AR 486, two from AR 484 and one from AR 488.

Shocks and SEPs

The abundance of fast and wide CMEs during the Halloween 2003 period (see Table 1) resulted in a large number of type II radio bursts in the corona and IP medium. Coronal and interplanetary shocks are inferred from type II bursts in the metric, decameter-hectometric (DH), and kilometric (km) wavelength domains. Shocks are also identified from in situ observations. During the October November 2003 period, 17 metric and 13 DH type II bursts were reported, with 11 of the DH bursts having metric counterparts. This represents an unusually large fraction (11/17 = 69%) of metric type II bursts having longer wavelength counterparts, compared to just 36% for the 1996-2002 period (Gopalswamy et al. 2004b). The type II association rate of Halloween CMEs was much higher than that of the general population: 21% vs. 10% for metric and 16% vs. 2.5% for DH type II bursts (see Table 1). Not all shocks observed near the Sun are observed at 1 AU, because weaker shocks decay before reaching 1 AU. Eight shocks were observed at 1 AU (roughly half of the shocks observed near the Sun)., which represent a higher concentration during the Halloween period.

One of the interesting aspects of the shocks observed during the Halloween period is their extreme transit times. There were only 15 shocks with a Sun-Earth transit time < 1 day since the time of the Carrington flare in 1859. The transit times were typically inferred from the flare onset to the sudden commencement (see Cliver and Svalgaard, 2004). Two of the 15 shocks were from the Halloween 2003 period with transit times of 18.9 (October 28, 2003 CME) and 19.7 h (October 29, 2003 CME). The historical events are shown in Fig. 4 along with two other SOHO events (not historical) for comparison: the 26 October 2003 event with a transit time of 31.8 h and the famous Bastille Day event (14 July 2000) with a transit time of 27 h. The solid curve is the empirical shock arrival (ESA) model (Gopalswamy et al. 2005c,e), which gives the shock transit time (T) in terms of the initial speed (V) of the driving CME: $T = ab^V + c$, where a = 151.002, b = 0.998625, and c = 11.5981. The ESA model curve suggests that a 3000 km/s CME would drive a shock that is expected to have a transit time of about 13.5 hours. A CME has to be launched with a speed of ~4300 km/s in order for its shock to have a transit time of ~12 h. The fastest CME observed by SOHO had a near-Sun speed of ~3387 km/s. There was only one other CME with speed exceeding 3000 km/s (2005 January 20 event, see Gopalswamy et al., 2005f). These results suggest that CMEs may not have speeds far greater than ~3000 km/s, which implies that CME-driven shocks take at least about

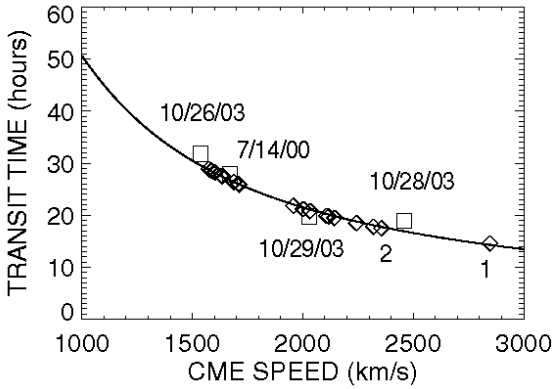

Fig.4. A plot of the Sun-Earth transit time (T) of shocks as a function of CME speeds (V) observed near the Sun. The solid curve is the empirical shock arrival (ESA) model: $T = ab^V + c$ with a = 151.002, b = 0.998625, and c = 11.5981). The travel times of historical events plotted as diamonds. The CME speeds of the historical events were inferred from the ESA model. For the three 2003 October events (10/26/03, 10/28/03, 10/29/03) and the Bastille Day event (07/14/00), the data points (squares) are from actual measurements of CME speeds (SOHO data) and shock travel times. The two fastest historical events are marked as 1 (1972 August 4) and 2 (1859 September 1).

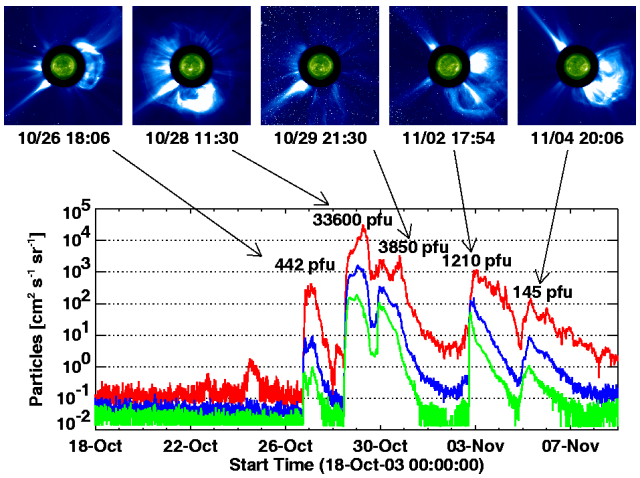

Fig.5. SEP events from GOES (>10 MeV, >50 MeV and >100 MeV channels in red, blue and green, respectively) and the associated LASCO CMEs from the October-November 2003 period. The peak SEP intensities are marked on the plot.

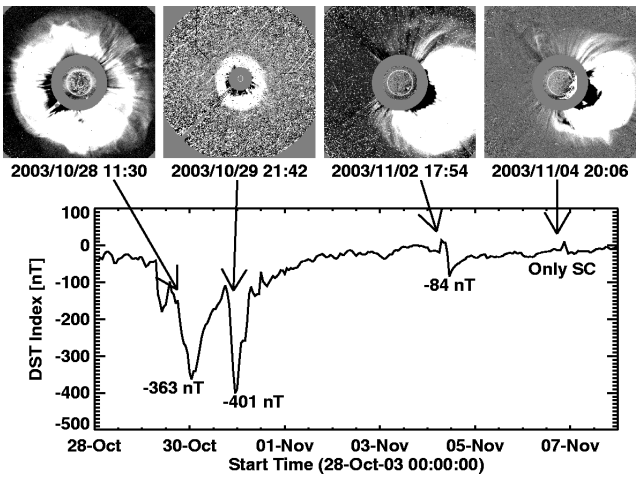

Fig.6. Snapshots of LASCO CMEs (top panel) associated with geomagnetic storms of the Halloween 2003 period as identified in the Dst index plot (bottom panel). The Dst responses of the four CMEs are marked. The last CME produced only a sudden commencement (SC).

half a day to reach Earth. The CME speed is ultimately linked to the amount of free energy available in active regions. AR486, which produced all the extreme events, had a maximum free energy of 4.6 x 10^{33} erg. One of the CMEs from AR 486 (the October 28 CME at 11:30 UT with a speed of ~2500 km/s) had a kinetic energy of 1.2 x 10^{33} erg, which represents ~ 26% of the free energy in the active region. It must be pointed out that active regions with spot areas twice as large as that of for the Carrington event (or AR 486) have been observed. This, along with the fact that only a small fraction of AR energy goes into the CME suggests that we may have yet to see the worst that the Sun has to offer. However, the limiting magnetic field in sunspots (~4500 G) suggests that the half-a-day transit time is a good limit for CME-driven shocks.

The strong shocks producing type II radio bursts also produce SEP events because the same shocks accelerate electrons (to produce the radio bursts) and ions (detected in situ). All the type II radio bursts that had counterparts at various wavelengths were associated with SEP events because the shocks are the strongest with consequences far into the heliosphere. Figure 5 shows that there were six large SEP enhancements (intensity >10 pfu in the >10 MeV channel) associated with five large CMEs: the first one was from AR484 on October 26 and the other four were from AR486. The two most intense events were from AR 486 on October 28 and 29. In both cases the energetic storm particle (ESP) event was larger. This is common for events originating from close to the disk center because of poorer magnetic connection (see e.g., Reames, 1999) early in the event. The October 28, 2003 SEP event was the most intense in solar cycle 23 in terms of >10 MeV flux and third largest in recorded history since 1976. The first and second largest events with 43,000 pfu and 40,000 pfu occurred in cycle 22 during March 1989 and October 1989, respectively. Three of the SEP events from the Halloween period (associated with the 2nd, 3rd, and 4th CMEs in Fig. 5) produced ground level enhancements (GLEs). In GLE events the SEPs penetrate all the way to Earth's atmosphere causing air showers detected by neutron monitors. There were only 14 GLE events in cycle 23 with 3 of them (21%) occurring during the Halloween 2003 period. Such a high concentration of GLE events were observed once during cycle 22 (19- 23 October 1989).

Geoeffectiveness and SEPeffectiveness

Two of the largest geomagnetic storms of cycle 23 occurred due to the two full halo CMEs from AR 486: on 28 October (Dst = -363 nT) and on 29 October (Dst = -401 nT. Figure 6 shows the evolution of the Dst index and the CMEs associated with the storms. Even though the four CMEs in Figure 5 were roughly homologous, their geoimpact were quite different. This is mainly a geometrical effect because CMEs originating from close to the disk center directly impact the magnetosphere while those ejected off to the Sun-Earth line result only in a glancing impact. The sheath of the November 2 CME impacted Earth's magnetosphere causing a modest storm (-84 nT), while the November 4 CME produced only a sudden commencement. Figure 6 demonstrates that only CMEs originating close to the disk center cause significant storms. The magnitudes of the storms are certainly consistent with the energy contents of the associated CMEs. However, there are other parameters that control the geomagnetic storms such as the inclination of the interplanetary CME with respect to the ecliptic among other solar and interplanetary parameters (see e.g., Srivastava and Venkatakrishnan, 2004). Comparison between Figs. 5 and 6 shows that the CMEs were also SEPeffective (producing large SEP events). The SEPeffective CMEs originate generally on the western hemisphere because the flux tubes carrying the SEPs need to be connected to an observer near Earth. On the other hand, geoeffective CMEs need to originate from close to the disk center for direct impact on the magnetosphere. Thus the center-west CMEs have the most important space weather consequences because they can be simultaneously geoeffective and SEPeffective (Gopalswamy, 2006).

Summary

The October – November 2003 CMEs and the associated events represent one of the best observed episodes of solar activity and hence provided information on several key

aspects of solar eruptions and their space weather effects (including active region size and potential energy, flare occurrence rate and peak intensity, CME speed and energy, shock occurrence rate, SEP occurrence rate and peak intensity, geomagnetic storm intensity). These events helped us assess the severity of solar eruptions for space weather. Some key results are: the largest soft X-ray flare (X28) of the cycle occurred during the October – November 2003 (X28) and was associated with an ultrafast CME (2657 km/s) on 2003/11/04. Fortunately, this CME occurred when the underlying active region was already at the west limb, so the CME was not Earth-directed. Other CMEs with comparable energy caused major geoeffects because they were ejected when the active region was close to the disk center. There was a high rate of energetic CMEs during this period. As a consequence, there was a high concentration of interplanetary shocks and CMEs that produced intense SEP events and super-intense (Dst = -363 and -401 nT) geomagnetic storms. The eruptions originated from active regions with largest areas reported for the current solar cycle. The large kinetic energies of CMEs are also consistent with the estimated free energy available in the active regions. One of the key results is that the Sun-Earth travel time of CME-driven shocks seems to be at least half a day, providing a practical limit for space weather applications.

Acknowledgement:

I thank S. Yashiro for help with figures. This research was supported by NASA's LWS TR&T and SR&T programs.

REFERENCES:

[1] Barbieri, L. P., and R. E. Mahmot (2004), October-November 2003's space weather and operations lessons learned, Space Weather, 2, S09002, doi:10.1029/2004SW000064.

[2] Burlaga, L. F., N. F. Ness, E. C. Stone, F. B. McDonald, and J. D. Richardson (2005), Voyager 2 observations related to the October – November 2003 solar events, Geophys. Res. Lett., 32, L03S05, doi:10.1029/2004GL021480.

[3] Cliver, E. W., and L. Svalgaard, The 1859 solar-terrestrial disturbance and the current limits of extreme space weather activity, Solar Phys., 224, 407, 2004.

[4] Gopalswamy, N., Coronal mass ejections of cycle 23, J. Astrophys. Astron., in press, 2006

[5] Gopalswamy, N., A. Lara, M. L. Kaiser, and J.-L. Bougeret (2001a), Near-sun and near-Earth manifestations of solar eruptions, J. Geophys. Res., 106, 25,261, 2001.

[6] Gopalswamy, N. S. Nunes, S. Yashiro, R. A. Howard, Variability of solar eruptions during cycle 23, Adv. Space Res., 34 (2), 391, 2004

[7] Gopalswamy, N., S. Yashiro, G. Michalek, H. Xie, R. P. Lepping, and R. A. Howard, Solar source of the largest geomagnetic storm of cycle 23, Geophys. Res. Lett., 32, L12S09, doi:10.1029/ 2004GL021639, 2005a.

[8] Gopalswamy, N., L. Barbieri, E. W. Cliver, G. Lu, S. P. Plunkett, and R. M. Skoug, Introduction to violent Sun-Earth connection events of October-November 2003, J. Geophys. Res., 110, A09S00, doi:10.1029/2005JA011268, 2005b

[9] Gopalswamy, N., S. Yashiro, Y. Liu, G. Michalek, A. Vourlidas, M. L. Kaiser, and R. A. Howard (2005b), Coronal mass ejections and other extreme characteristics of the 2003 October-November solar eruptions,

[10] J. Geophys. Res., 110, A09S15, doi:10.1029/2004JA010958, 2005c.

[11] Gopalswamy, N., E. Aguilar-Rodriguez, S. Yashiro, S. Nunes, M. L. Kaiser, and R. A. Howard, Type II radio bursts and energetic solar eruptions, J. Geophys. Res., 110, A12S07, doi:10.1029/2005JA011158, 2005d.

[12] Gopalswamy N., A. Lara, P. K. Manoharan, and R. A. Howard, An empirical model to predict the 1-AU arrival of interplanetary shocks, Ad. Space Res., 36, 2289, 2005e

[13] Gopalswamy, N., H. Xie, S. Yashiro, and I. Usoskin, Coronal Mass Ejections and Ground Level Enhancements, 29th International Cosmic Ray Conference, Pune, 00, 101-104, 2005f

[14] Jackman, C. M. et al., Neutral atmospheric influences of the solar proton events in October-November 2003, Journal of Geophysical Research, Volume 110, Issue A9, CiteID A09S27, 2005.

[15] Reames, D., Particle acceleration at the Sun and in the heliosphere, Space Sci. Rev. 90, 413, 1999.

[16] Skoug, R. M., J. T. Gosling, J. T. Steinberg, D. J. McComas, C. W. Smith, N. F. Ness, Q. Hu, and L. F. Burlaga, Extremely high speed solar wind: 29– 30 October 2003, J. Geophys. Res., 109, A09102, doi:10.1029/ 2004JA010494, 2004.

[17] Srivastava, N. and P. Venkatakrishnan, Solar and interplanetary sources of major geomagnetic storms during 1996-2002, J. Geophys. Res., 109, A10103, doi:10.1029/2003JA010175, 2004.

[18] Yashiro, S., N. Gopalswamy, S. Akiyama, G. Michalek, and R. A. Howard, Visibility of coronal mass ejections as a function of flare location and intensity, J. Geophys. Res., 110, A12S05, doi:10.1029/2005JA011151, 2005.

Long-term Prediction of Solar Extreme Events basing on the General Regularities of Energetic Particle Generation by the Sun

R. Nymmik

D.V.Skobeltsyn Institute of Nuclear Physics, M.V.Lomonosov Moscow State University,
nymmik@sinp.msu.ru

The solar energetic particle (SEP) generation by the Sun and the SEP event occurrences in the Earth orbit are of probabilistic nature. At the same time, certain regularities inherent to SEP fluxes and events can well be inferred from the present-day experimental results, which permit also the regularities to be used in predicting the probability for SEP events (the solar extreme events, in particular) to occur. The probability for the solar extreme events to occur within any definite period is shown to depend solely on the sum of mean-monthly sunspot (Wolf) numbers throughout that period. The concept of predominant extreme event occurrences during certain solar activity phases (maximum, ascending or declining phases) has been shown to be invalid.

Introduction

There exist some propositions about the extreme SEP event occurrence periods. As stated in [1], for example, "anomalously large events are somewhat more likely to occur early or late in the active phase of solar cycle". Ref. [2] claims: „it is the fact that major flare events are relative rare near the sunspot maximum and occur mostly in the ascending and declining phases of sunspot occurrence". Ref. [3] states: "there may be a tendency for the largest events to occur during the 2nd to 4th year after SA maximum". From the analysis of the cited papers it follows that all of such statements are of illusory, rather then physical, nature because they have never been supported by any mathematical or statistical argument.

There exist also fundamental propositions concerning the SEP event occurrences in general. Ref. [1] has introduced the concept of the maximum and minimum phases of solar cycles. It was stated repeatedly in Refs. [3, 4] that, if the maximum of a cycle is defined up to 0.1 year, the active Sun period is 7 years (2 years before and 4 years after the year of solar maximum) and the quiet Sun period is 4 years. Moreover, it was claimed in [3,4] that none of hazardous (that is, "extreme") SEP events could occur during the quiet Sun period. The last proposition is also a result of visual analysis of some figures and has not been founded statistically. Unfortunately, all the above assumptions underlie the most widespread JPL-91 [4] and ESP [5] SEP fluence and peak flux models, which are used to calculate the radiation effects in the space.

In the present work, we extend and specify the statistical analysis of the SEP distribution function properties initiated in [6]. According to [6], there exists a definite probability for the extreme SEP events to occur during the quiet sun period too.

The techniques for analyzing experimental data

We used and analyzed the experimental data on the ≥30 MeV SEP event proton fluences and peak fluxes measured by CPME instrument on IMP-8 from July 1974 to September 1986 and by TELESCOPE and DOME instruments on GOES-7,8,10, and 11 (so called uncorrected data) from October 1986 to September 2005. The reliability of the data has been confirmed by the thorough analysis made in [7].

The SEP event selection

The SEP events were selected from the monitoring sequences of interplanetary particle flux measurements in the differential channels of the above instruments that were also used to calculate the proton flux sizes. When selecting the SEP events, we rejected the commonly used technical criterion, namely, "the total fluence occurring over series of days, during which the proton fluence (or local peak flux) exceeded the selected threshold", is regarded as a SEP event [3]. We are of the opinion that the criterion cannot be used to study the physical phenomena relevant to SEP events. We selected the events basing on the concept that any increase of the ≥30 MeV proton flux signifies commencement of a new event, except for the cases where the increase is due to the arrival of bow shock protons. This simple criterion selects actually those same events that were selected in the SEP energy spectra catalogues [8,9,10] by the complicated criteria involving, first of all, observation of X-ray bursts on the Sun prior to arrival of SEP. The SEP event ≥30 MeV proton fluences and peak fluxes were calculated from the data of the IMP-8 and GOES instruments on assumption that the SEP event ≥30 MeV proton spectra are power-law functions of proton rigidity [11, 12]:

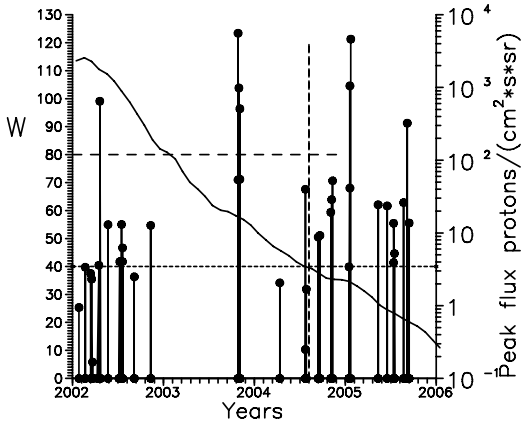

Fig.1. The smoothed sunspot (Wolf) numbers (the left-hand ordinate) and the SEP peak fluxes the declining phase of the last solar cycle. The range of W below 40 is the so-called quiet Sun period.

$$F(E)dE = F(R)\frac{dR}{dE}dE = C\cdot\left(\frac{R}{R_0}\right)^{-\gamma}\cdot\frac{dE}{\beta} \quad \textbf{(1)}$$

where $\beta = R/\sqrt{R^2+m^2c^2}$ is the relative particle velocity; $R=\sqrt{E(E+2mc^2)}$; R_0 = 239 MV.

Relation between the SEP event occurrence time and solar activity level

The SEP events were compared to sequences of smoothed mean-monthly Wolf numbers as interpolated to the day of SEP event commencement. Fig. 1 shows the smoothed numbers of SEP events and sunspots (the smooth curve and the left-hand ordinate) and the peak flux sizes in separate events (the right-hand ordinate) for the declining phase of sunspot occurrences during cycle 23.

It should be emphasized that the choice of the methods for selecting SEP events, determining the event sizes, calculating particle fluxes, and determining solar activity on the day of SEP event generation were applied solely to those experimental data and analysis techniques, whose reliability has been confirmed in quite a number of our works, including [7].

The distribution of SEP event particle fluences and peak fluxes

Fig.2 shows the integral distributions of SEP events with ≥30 MeV proton fluences measured on IMP-8 and GOES-7,8,11 from July 1974 to September 2005 and their approximation in the $10^6 < F_{30} < 4\cdot10^9$ protons/cm^2 range by a power law with an exponential rollover (Eq. 2)

$$\Psi(\geq F_{30}) = \frac{C\cdot F_{30}^{-\gamma}}{\exp\left(\frac{F_{30}}{F_e}\right)}, \qquad (2)$$

where γ=1.30±0.01 and Fe=(6.0±2.2)·109.

Below $F_{30}=10^6$, the experimental data distribution drooped due to threshold effect because the dataset includes all events with $F_{\geq30}\geq10^6$ and a fraction of events with $F_{\geq30}<10^6$ subject that the peak fluxes were $f_{\geq30}\geq1$ proton/(cm^2·s·sr). Basing on the results of [13], the function (Eq.2) was extrapolated down to $F_{\geq30}=10^5$. Against the galactic background, most of the events of such sizes pass unnoticed, or are observable only in the ≥10 MeV fluxes, for which the nature of the increase cannot be unambiguously identified in all cases. It should be noted that in [13] we found the distribution slope γ=-1.40 for the set of events of cycles 20-22, when we used the database from [14].

Fig. 3 shows the experimental data obtained during the above period for SEP peak fluxes. The distribution slope is the same as the slope of the SEP event distribution of fluences (γ=-1.32±0.01), while the exponent is $f_e=(1.6\pm0.8)\,10^4$. The slope of the displayed distribution is close to γ=-1.28±0.01 presented in [15], where, however, the evident rollover in the distribution at $f_{\geq30}>10^3$ protons/(cm^2·s·sr) was missed.

The distribution functions at different solar activity levels

We divided the entire SEP event dataset into three groups that occurred during periods of W≥80 (L), W<80 (M), and W<40 (S) (the "quiet" time period) and calculated the distribution functions for each of the groups. The results are displayed in Fig. 4 together with the distribution function calculated over the entire SEP event dataset. The forms of the resulting distribution functions prove to be alike.

To get a more convincing picture, we divided the distribution functions by the sums of the mean-monthly Wolf numbers during the solar activity periods when the SEP events were measured. The sums are $\sum W_{all}=27819$, $\sum W_{\geq80}=20189$, $\sum W_{<80}=7630$, and $\sum W_{\leq40}=3018$.

As the result, we have obtained the normalized distribution functions shown in Fig. 5, from which it follows that, within the statistical limits, the normalized distribution functions are the same.

This means that, when normalized to the sum of sunspot numbers over the measurement period, the SEP particle distribution functions are invariant with respect to solar

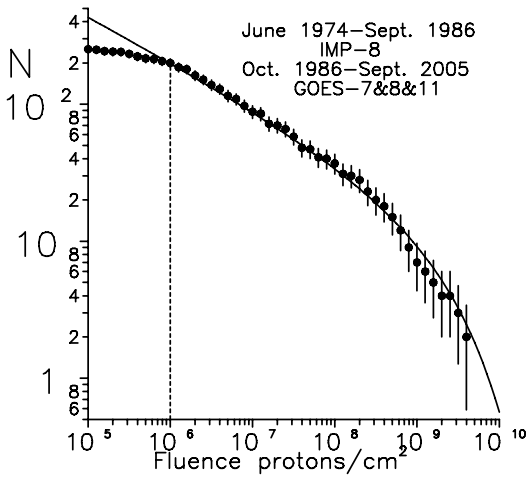

Fig.2. The distribution function of the SEP event fluences from June 1974 to June 2005. The line is the function according to Eq.(2). The vertical dashed line is the 100% detection limit

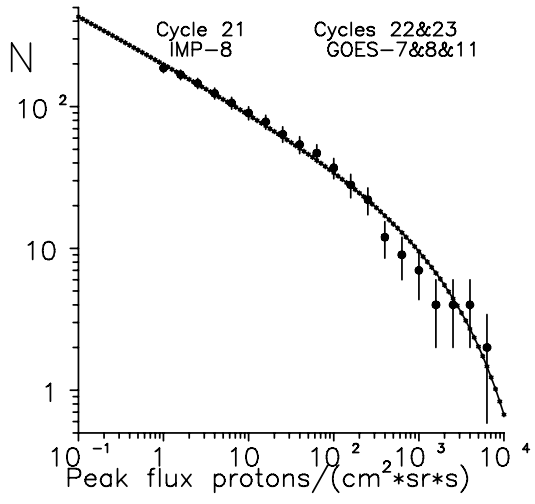

Fig.3. The distribution function of the SEP event peak fluxes from June 1974 to June 2005. The dotted line is the approximation of the experimental data by their interpolation to the range of peak fluxes <1 proton/(cm2 s·sr).

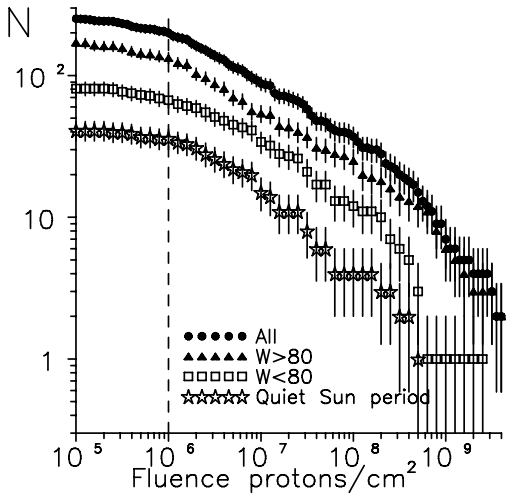

Fig.4. The SEP event distributions of proton fluences during different solar activity periods (W>80; W<80; W<40) and for all events.

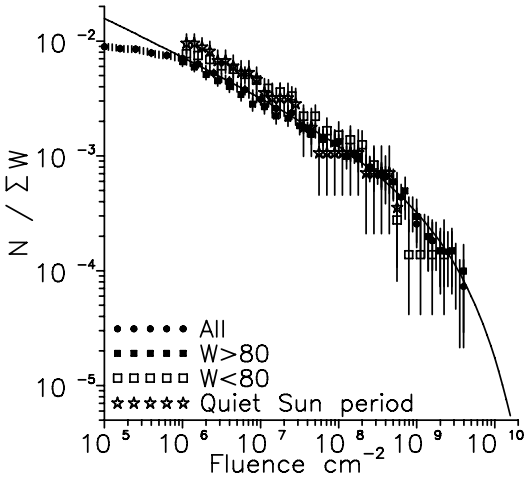

Fig.5. The distributions of the SEP events fluences as divided by the sums of sunspot numbers in the measurement periods for each of the event groups.

activity [6]. Therefore, the occurrence probability of identical large SEP events is the same for an annual period characterized by the mean-monthly sunspot number W=150 and for a 5-year period with W=30.

In other words, there exists a certain probability for the extreme large events to occur even during the quiet time period.

It is not difficult to demonstrate that this effect is due to the casual sum of random fluence sizes in the SEP events generated according to the distribution function (Eq. 2), but does not result from the differences in the physics of SEP event generation at different solar activity levels.

Table 1 presents some other characteristics of solar activity periods, namely, number of events (N) with ≥30 MeV proton fluences $F_{\geq 30} \geq 1 \cdot 10^6$ and $F_{\geq 30} \geq 4 \cdot 10^8$, as well as the cumulative fluences ($\sum F_{\geq 30\ MeV}$). It is seen that, having been divided by the sum of the sunspot numbers ($\sum W$), the numbers of SEP events are the same in any solar activity period. On the other hand, however, the cumulative fluences divided by the sum of the sunspot numbers seem to decrease with falling solar activity.

The distribution functions during different solar activity phases

First of all, we should define the ascending and declining solar activity phases and find out what is the solar maximum period. Solar maximum can be formally defined to be the maximum in the smoothed set of sunspot numbers for a given cycle or, more physically, the sign reversal period of the heliospheric magnetic field. We defined solar maximum to be an annual period symmetric around the month of the field sign reversal. The solar maximum periods were proposed to be 1979.96÷1980.96; 1989.46÷1990.46; and 2001.12÷2002.12 for cycles 21, 22, and 23, respectively. The ascending period is defined to extend from sunspot minimum to the beginning of the solar maximum period, and the declining period from the end of the solar maximum period to the next sunspot minimum. Fig.6 demonstrates the distribution functions for the ascending and declining solar

TABLE 1

The characteristics of the selected time periods, the SEP event numbers, and the cumulative fluences

1	SA period	All	W≥80	W<80	W<40
2	Duration [months]	379	162	217	140
3	$\sum W$	27819	20189	7630	3018
4	N ($F_{\geq 30} \geq 1 \cdot 10^6$)	194	133	61	30
5	$n(F_{\geq 30} \geq 1 \cdot 10^6)/\sum W$	(7.0±0.5) 10^{-3}	(6.6±0.6) 10^{-3}	(8.0±1.0) 10^{-3}	(9.9±1.8) 10^{-3}
6	N ($F_{\geq 30} \geq 4 \cdot 10^8$)	18	13	5	2
7	$n(F_{\geq 30} \geq 4 \cdot 10^8)/\sum W$	(6.5±1.5) 10^{-4}	(6.5±1.8) 10^{-4}	(6.7±3.0) 10^{-4}	(6.9±4.9) 10^{-4}

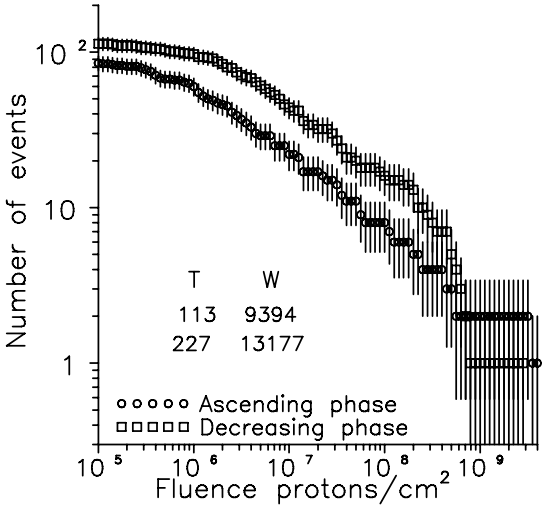

Fig.6. The SEP event distributions for ascending and declining solar activity phases.

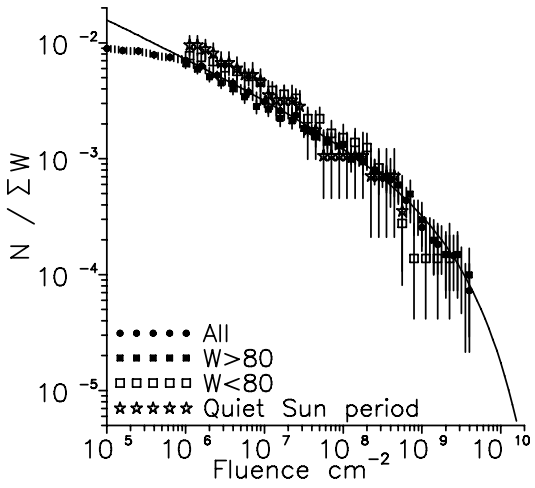

Fig.7. The Distributions of SEP event fluences divided by the sums of sunspot numbers during the ascending and declining solar activity phases.

activity phases according to the above-analyzed data. The distribution function of the declining phase runs above the function for the ascending phase. But, if we divide the functions by the sum of the annual sunspot numbers in the appropriate periods ($\sum W_a$=9394 and $\sum W_d$=13080), we come to the normalized distribution functions shown in Fig. 7.

These functions are close to one another, so the probability for extreme events to occur during both phases is alike within the statistical errors in experimental data.

Table 2 presents the SEP event numbers and the cumulative fluences in the SEP events observed during the periods analyzed.

Examine the Table 2 data. In row 6, we see the SEP event number divided by the sum of sunspot numbers throughout the measurement periods. The values are close to each other and to the data shown in row 5 of Table 1. From the row 7 data, we can conclude that the large SEP events did not avoid solar maximum and that, within the statistical errors, all 3 periods are alike as regards occurrences of large events. Two extremely large events of the periods analyzed occurred during the ascending and maximum solar activity (row 8).

It is not surprising that the cumulative fluences normalized by the sum of sunspot numbers are close to each other because their deviations are of random nature.

TABLE 2

The characteristics of time periods, the SEP event number n, and the cumulative fluences ∑F

1	SA phase	Ascending	Declining	Maximum
2	Duration [years]	9.4	18.6	3
3	$\sum W$	$\sum W_a$=9394	$\sum W_d$=13080	$\sum W_m$=5020
4	n ($F_{\geq 30} \geq 1 \cdot 10^6$)	60	90	43
5	n($F_{\geq 30} \geq 1 \cdot 10^6$)/$\sum W$	$(6.4 \pm 0.6) \cdot 10^{-3}$	$(6.9 \pm 0.6) \cdot 10^{-3}$	$8.5 \pm 1.3) \cdot 10^{-3}$
6	n($F_{\geq 30} \geq 4 \cdot 10^8$)	4	7	7
7	n($F_{\geq 30} \geq 4 \cdot 10^9$)	1	0	1
8	$\sum F_{\geq 30\ MeV}$ [protons/cm^2]	$9.7 \cdot 10^9$	$9.1 \cdot 10^9$	$1.3 \cdot 10^{10}$
9	$\sum F_{\geq 30MeV} / \sum W$	$1.0 \cdot 10^6$	$7.0 \cdot 10^5$	$2.5 \cdot 10^6$

The SEP events during the quiet Sun period

Thus, the above analysis has failed to demonstrate a preferable solar activity period for the extremely large SEP events to occur. Moreover, the analysis has demonstrated that the events of this kind may occur during any solar activity period, the so-called "quiet" Sun period included.

This fact is demonstrated in Fig.1, which shows the smoothed sunspot number curve for 4 years of the last solar cycle and the occurrence moments of SEP events, with their peak fluxes sizes represented by the vertical lines (the right-hand y-axis).

We can see that the large SEP events occurred at W=56 and even at W=35 and 28. As the quiet Sun periods are defined in [3, 4, 14] to coincide with W <40, Fig. 1 demonstrates how many SEP events (the large events included) can occur during those periods. So, the basic proposition, which underlies the JPL-91 SEP flux model described in [4,14] and the ESP model described in [5] and states that the SEP fluxes of the quiet Sun periods must be neglected, cannot withstand even the simplest criticism. From our analysis it follows that quite a definite probability exists for even the extremely large SEP events to occur in the Quiet Sun period.

The problem of the sizes of the extreme SEP fluxes

During the last decades, the problem of the extremely large events was resolved by the simplest method.

The author of [16] has declared possible limits of the peak fluxes in the extremely large events. However, none of analytical or mathematical arguments for the limits have been presented in [16]. Instead, he draws a subjective pictorial curve in the Figure that shows the set of SEP energy spectra measured since 1989.

The extremely large, or worst-case, events were declared in many works to be the largest measured SEP events. So, one of four events observed (23 February 1956, July 1959, 7 August 1972, September or October 1989) was declared to be an extreme SEP event. As the energy spectra of the events are different, while their fluxes often reached their maxima

at different energies, the authors of the SEP flux models constructed the artificial events to be sums of different events. In the CRÈME-81 model, for example, the authors of memorandum [17] constructed the extremely large peak flux energy spectrum by adding the artificial power-law spectrum above 150 MeV to the August 4 1972 event spectrum below 150 MeV. In the SPENVIS model [18, 19] intended for resolving the practical problems, the extremely high-energy spectra for 7-year space mission duration was proposed to be the August 4 1972 event spectrum multiplied by factor 5. All the propositions are arbitrary, rather than scientific. In our opinion, the problem of the extremely large events should be resolved in terms of the distribution functions and their extrapolation to the range of large events.

Fig. 8 shows the distribution function forms proposed by some authors. All the `functions have been calculated basing on the same experimental data as used in the present paper.

Curve (1) is the distribution function of the ESP model [5,20], based on the maximum entropy theory. This method is one and only that leads to a constant size of the extremely large fluxes. However, the constant size depends strongly on the experimental data set that underlies the method. The occurrence of even a single large event can markedly change the extremely large flux size. Curve 2 is the approximation (Fig. 2) used in the present work. In this case, the constant extreme flux is absent, but there are different probabilities for an extreme-size fluence to occur. To within a probability of about 10^{-4}, our model predicts the ≥30 MeV proton fluence F_{30}~$2\cdot10^{10}$ protons/cm^2. This is close to F_{30}~$1.2\cdot10^{10}$ predicted by the ESP model [20], which is 5 times the largest measured fluence and 3 times the fluence predicted by the ESP method using the distribution of the present work.

Curves (3) and (4) are the lognormal distribution functions used in the JPL-91 [3, 4, 14] SEP model. The two functions were constructed basing on different experimental data. Besides, different methods were used in the range of small fluences to select the SEP events.

In [13], we have demonstrated that the parameters of the lognormal function are partly determined by the SEP event detection threshold and selection criterion and, therefore, the lognormal functions are not the best to describe the extrapolation to the range of large SEP events.

From Fig. 8 it follows that the extrapolations of lognormal functions to the range of extreme fluence sizes depend primarily on the distribution function form in the range of small fluences. Therefore, the JPL-91 predictions of the extreme flux occurrences do not seem to be realistic (within the probabilities near 10^{-4}, the distribution predicts the fluences F_{30}~$10^{11}\div10^{12}$ protons/cm^2).

The extrapolations used in the ESP model and in the present work can hardly be preferred, but it is quite clear that the occurrence of a very large event can essentially alter the parameters of the distributions in the range of large events.

The same methods, using the distribution function of different-energy protons, are the best to determine the probability for the extremely large proton fluences and peak fluxes to occur at other energies (beside energies ≥30 MeV).

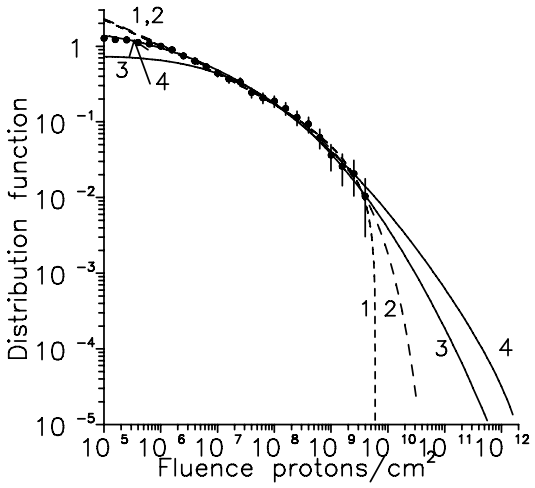

Fig.8. The experimental data on the distribution function of proton fluences and their approximations in terms of different models. Line 1 is the function by the ESP model (according to the maximum entropy theory). Line 2 is the approximation according to Eq. (2) Line 3 is the lognormal approximation of the experimental $F_{30}\geq10^6$ data. Line 4 is also the lognormal function, the $10^5\div10^6$ proton/cm^2 range included.

Conclusion

The analysis of the experimental data on the distribution of SEP event proton fluences (and peak fluxes) as dependent on solar activity periods has shown that, having been divided by sums of sunspot numbers of the measurement periods, the event distribution functions prove to be invariant. This relates to both the events observed at different solar activity levels and the Sun-generated events during the ascending and descending activity phases.

The fundamental conclusion drawn from the analysis is that the extremely large SEP events can well occure during any solar activity phase and that the probability for them to occur is the same in the periods of identical sums of smoothed mean-monthly sunspot numbers.

The results of the present work disprove quite a number of widespread fallacies, first of all the claimed negligible SEP fluxes during quiet Sun that underlie the JPL-91 [3,4,14] and ESP [5,18] SEP flux models.

From the invariance of the normalized distribution function it follows also that the extremely large SEP events can occur during any solar activity phase.

The distribution function, which results essentially from the casual set of random-size fluences, though governed by a general regularity of the type of (2), has been shown to bring about so large fluctuations of cumulative fluences that the search for a correlation between solar activity (separate cycles, for instance) and cumulative fluences gets absolutely senseless, considering the set of the present-day experimental data,.set of random-size fluences, though governed by a general regularity of the type of (2), has been shown to bring about so large fluctuations of cumulative fluences that the search for a correlation between solar activity (separate cycles, for instance) and cumulative fluences gets absolutely senseless, considering the set of the present-day experimental data.

Acknowledgements

The author is indebted to Professor M.Panasyuk for his support and to Dr. D.Mottl for his assistance in developing the SEP database.

REFERENCES

[1] J.H. King, "Solar proton fluences for 1977-1983 Space Missions", J. Spacecraft and Rockets, vol.11, No.6, 1974, pp.401-409

[2] J.N.Goswami, R.E.McGuire, R.C.Reedy, D.Lal, and R.Jha, "Solar flare protons and alpha particles during the last three solar cycles", JGR, vol.93, No.A7, 1988, pp.7195-7205

[3] J.Feynman, T.P.Armstrong, L.Dao-Gibner, and S.Silverman, "Solar proton events during solar cycles 19, 20, and 21", Solar Physics 126, 1990, pp.385-401

[4] J.Feynman, G.Spitale, and J.Wang, "Interplanetary Proton Fluence Model: JPL 1991", JGR, 98(A8), 1993, pp.13281-13294

[5] Xapsos M.A., Summers G.P., Shapiro P., and Burke E.A. "New techniques for predicting solar proton fluences for radiation effects applications", IEEE Trans. on Nuclear Science, vol. 43(6), 1996, pp.2772-2777

[6] R.Nymmik, "Relationships among Solar Activity, SEP occurrence frequency, and solar energetic particle event distribution function", Proc. 25th ICRC,vol. 6, 1999, pp.280-283

[7] [7] D.Mottl and R.Nymmik, "The issues of reliability of solar energetic proton flux data bases and models", Adv. Space Res. (in press), 2005

[8] G.A.Bazilevskaya, E.V. Vashhenyuk., V.N.Ishkov et al., "Catalogue of Energy Spectra of Solar Proton Events of 1970-1979", IZMIRAN, Moscow, 1986

[9] G.A.Bazilevskaya, E.V.Vashhenyuk, V.N.Ishkov et al., "Solar Proton Events, Catalogue for 1980-1986", Inter-agency Geophysical Committee, Moscow, 1990

[10] A.I.Sladkova, Bazilevskaya G.A, V.N.Ishkov et al., "Catalogue of Solar Proton Events, 1987-1996", Ed. Yu.I.Logatchov, Moscow University, 1998

[11] R.A.Nymmik, "|Averaged energy spectra of peak flux and fluence values in solar cosmic ray events", Proc. 23-rd ICRC, Calgary , vol.3, 1993, pp.29-32

[12] D.A.Mottl, R.A.Nymmik, A.I. Sladkova., "Spectra of solar energetic protons derived from statistical analysis of experimental data on large set of events", Proc. of 27th ICRC, vol.8, 2001, pp3185- 3188

[13] Kurt Victoria and R.A.Nymmik, "Distribution of solar cosmic ray events over proton fluences", Cosmic research, vol.35(6), 1997, pp598-609

[14] J.Feynman, T.P.Armstrong, L.Gao-Gibner and S Silverman, "New interplanetary proton fluence model", J.Spacecraft vol. 27(4), 1990, pp.403-410

[15] Kurt Victoria, H.Mavromichalaki, M.Gerontidou, "Energy dependence of the solar proton events at 1 AU", in Proc. "Magnetic Coupling of the Solar Atmosphere Euroconference and IAU Colloquium 188", Santorini, Greece, 11-15 June2002, (ESA SP-505, October 2002) pp473-476

[16] L.I.Miroshnichenko, "Upper intensity-energy limits and utmost spectrum for solar cosmic rays", Proc. 23th ICRC, 1995,pp. 62-65

[17] J.H.Adams, R.Silberberg and C.H.,Tsao, "Cosmic ray effects on microelectronics, Part I: The near-earth particle environment", NRL Memorandum Report 4506, 1981

[18] C.Tranquille, E.J.Daly, "An evaluation of solar-prpton models for ESA missions", ESA Journal, vol.19, 1992, pp.275-295.

[19] http://www.spenvis.oma.be/spenvis/help/background/flare/flare.html

[20] M.A.Xapsos, G.P.Summers, J.L.Barth, E.G.Stassinopoulos, E.A.Burke, "Probability model for worst case solar proton event fluences", IEEE Trans. on Nuclear Science, 46(6), 1999,pp.1481-1484

Energy Spectrum of Solar Cosmic Rays in Large Events

G.A. Bazilevskaya

Lebedev Physical Institute of RAS, Leninsky prospect, 53, 119991, Russia, bazilevs@fian.fiandns.mipt.ru

Energy spectrum is one of most important features of solar energetic particles. It is connected to acceleration, propagation, and loss mechanisms, as well as time and site of particle generation and propagation. On the other hand, energy spectrum is a measurable feature, however loaded with many signatures of above mentioned processes. It is hardly possible to disentangle and identify all factors of the spectrum formation from the observational data. The purpose of this paper is to outline the processes involved in the spectrum formation. The giant event of 20 January 2005 is chosen to test the modern concepts of the particle acceleration and transport.

Introduction

During more than half of a century the observers residing at the Earth try to understand the origin of high-energy particles connected with explosion-like releases of energy on the Sun. These particles were named "the solar cosmic rays (SCRs)" because enhancement of particle intensity was observed after powerful solar flares against the background of galactic cosmic rays. Nowadays, the customary name is "the solar energetic particles (SEPs)" or "the solar protons" since more than 90% of SEPs are protons. The lower energy limit of SEPs is not strictly determined being at least less than ~100 keV/n, but it is rather conventional to consider for large SEP events particles with more than several MeV/n. The higher energy limit of SEPs is certainly above several GeV/n, and there are some indications that even above 500 GeV protons were observed during some SEP events [1]. However, particles with energies not more than several hundreds MeV/n are detected during majority of SEP events. The SEP energy spectrum cannot be measured by a single device. At energies below 100 MeV, SEPs do not penetrate deeply in the Earth's atmosphere and can only be observed by the spacecraft spectrometers. SEPs with energies above ~ 1 GeV interact in the atmosphere and contribute to the count rate of the ground-based neutron monitors and muon telescopes. Therefore, the most powerful SEP events containing the relativistic protons are called the ground level enhancements (GLEs). The energy spectrum of relativistic solar protons can be derived from the ground-based installations. In the intermediate range of 100 – 500 MeV, the SEP energy spectrum is measured on balloons in the atmosphere and on the satellites. SEPs intrusions are sporadic events when particle intensity increases and after a while return to the galactic cosmic ray background forming a SEP intensity-time profile. In some events, SEPs of different energy come to the Earth and reach the maximum of intensity according to their velocity dispersion, in other events the intensity-time profiles are synchronous for different energy channels. It is customary to characterize a SEP event by the energy spectrum composed from particle intensity in the maximum of the SEP time history (TOM spectrum, [2]). In the case of an instant source near the Sun and diffusive propagation of energetic particles in the interplanetary space, such a spectrum reflects the spectrum in the source and may be indicative of the particle acceleration process. The fitting of the spectrum shape by a power-law, exponential or more complicated function was widely used to draw conclusions on the acceleration mechanism. From analysis of ~60 spectra of solar protons and alphas with energies up to 400 MeV Ref. 2] stated that the best fit was a modified Bessel function of the 2nd kind in momentum per nucleon with a parameter αT, where α is acceleration efficiency and T is escape time. This function was considered as an argument for stochastic acceleration. Ref. [3] found the best approximation of energy spectra of solar protons and electrons to be a power law with exponential turnover at high energies and explained this by a diffusive shock acceleration with a shock of finite spatial extent. Although SEPs observed at the Earth's orbit are subject of numerous processes of acceleration and transport affecting their energy distribution, every observer wishes to know if it is possible to make any conclusion about particle acceleration on the Sun from the observed SEP energy spectrum shape. This question is closely connected with the long-standing discussion in the cosmic ray community about origin of SEPs. After publishing the works [4, 5], many scientists hold the opinion that SEPs of the large so called gradual events are a product of acceleration in the space by the CME-driven shocks. There are energetic particles accelerated in the flare site, but they are mainly trapped in the closed magnetic loops in the Sun's lower corona. These particles interact with the ambient solar matter and generate secondary emission, for example, X-rays, gamma-rays, and neutrons which are detected after some solar flares [e.g. 6]. It is believed that only minor part of the flare originated particles escapes into space and produce so called impulsive SEP events. Most of events with solar proton intensity J(E>10 MeV) $\geq$ 10 $cm^{-2}s^{-1}sr^{-1}$ (*pfu*) including all extreme events pertain to the gradual events and are of utmost interest from both fundamental and practical points of view.

The SEP transport in corona and interplanetary space also influences the energy spectrum and should be accounted for when trying to find the acceleration conditions. The main processes are the pitch angle diffusion, focusing in the diverging interplanetary magnetic field, and convection and adiabatic cooling in the solar wind. In the last decade, it becomes clear that energetic particles themselves change the space properties by means of the Alfvén waves generation/amplification.

Here is an attempt to clarify a question: what information on the generation processes can be extracted from the energy spectra observed at 1 AU? First, the conventional acceleration mechanisms are outlined. Second, the energy spectra for the extreme SEP event of 20 January 2005 as observed by various authors are presented. Conclusion is drawn that the first arriving relativistic particles in this case could hardly be accelerated by the CME-driven shock, so they brought information on the solar sources. However, a

shock probably contributed in the particle flux and spectrum later in the event.

The main processes of particle acceleration on the Sun and in the inner heliosphere

Although particle acceleration is a ubiquitous process throughout the universe there are few mechanisms widely considered in SEP production. The main are stochastic acceleration, shock acceleration, and acceleration by the DC electric fields in the process of magnetic reconnection.

The stochastic acceleration

The stochastic acceleration takes place in the turbulent plasma, where particles gain or lose energy while scattering, but they systematically gain energy over long times. This is because the head-on, energy-gaining, collisions happen more often than the overtaking, energy-losing, collisions. The scattering centra are turbulent perturbations, typically fast mode MHD waves, randomly distributed throughout the plasma. The turbulence is presumably generated during the magnetic reconnection or other energy input as a large-scale disturbance and proceeds though the cascading rapidly to smaller length-scales. Thus the broad range of the wave lengths provides effective particles and waves coupling via a resonance process, which occurs when the frequency of rotation of the wave electric field is an integer multiple of the particle gyration frequency [7]. The oblique Alfvén waves and the fast-mode magnetosonic waves are considered in the wave-particle interaction, the condition of resonant wave-particle interaction can be expressed as $k_{//}/B \approx R^{-1}$, where B is magnetic field strength, $k_{//}$ is the magnetic field-aligned component of the wave vector, R is a particle rigidity [8]. The momentum gain dP/dt is proportional to $(u/v)^2$, where u is the plasma flow velocity and v is the particle velocity, i.e. it is a second order Fermi process. This process can be treated as diffusion in the momentum space. The injection problem is very important for stochastic acceleration. It was found that turbulence with the energy density of ~10 erg/cm^3 could accelerate protons from quasi-thermal to relativistic energy during ~ 1 – 10 s [9]. This requires B~1000 G which is reasonable condition for an active region. However, the thermal electrons cannot resonate with Alfvén and fast-mode magnetosonic waves, therefore the seed population of deka-keV electrons is necessary. The injection problem for electrons can be overcome by several ways [7, 10]. The energy spectra of particles are determined by the energy dependence of acceleration and escaping from the acceleration region and may have a power-law or exponential forms [10-12]. Stochastic acceleration is often considered as the main acceleration mechanism in impulsive solar flares [e.g., 12]. For instance, it occurs in the high turbulent sites emerging near the magnetic reconnection in current sheets of a flaring region.

The shock acceleration

The shock acceleration may be drift and diffusion. In the first case particles acquire energy drifting along the shock front in the electric field $E=-[u\times B]/c$, where u is the shock velocity, B is magnetic field strength [13]. Acceleration is effective only for the perpendicular shocks and can hardly contribute much in SEPs [7]. The diffusive shock acceleration occurs due to the turbulent regions ahead and behind a shock front, which serve as multiple scattering centra allowing a particle to be accelerated by a first order Fermi process. It is like walls moving toward each other (in the rest frame of the shock), so a particle gains energy at each collision with a wall similar to the elastic ball [14, 15]. The particles gain energy from the bulk plasma motion near the shock front. Diffusive shock acceleration occurs in the quasi-perpendicular and quasi-parallel shocks. The momentum gain dP/dt is proportional to u/v, where v is the particle velocity. The spectrum has a power form

$dN/dP \propto P^{-\delta}$,

where $\delta = (\sigma + 2)/(\sigma - 1)$,

$\sigma = u_1/u_2$ is the compression ratio, u is the bulk plasma flow velocity in the shock rest frame, sub indices 1 and 2 relate to the upstream and downstream plasmas, respectively [e.g., 13]. The spectrum becomes steeper at the higher energy edge because of finite shock life time and/or particle escape from a shock of finite spatial extent. This leads to the energy spectrum of the form $dN/dE \propto E^{-\gamma} \exp(-E/E_0)$ [3, 16].

Like in the stochastic acceleration, ions may be accelerated beginning from the thermal state, electrons must be injected at energies at or above the thermal energy by a factor of the ratio of proton to electron mass since electrons need to be relativistic in order to be scattered by the Alfvén turbulence associated with the shock [7, 10]. The typical time of acceleration is <1 s for 100 MeV/n [3].

Diffusive shock acceleration is believed to be the main source of SEPs in the so called gradual events [e.g. 5]. The shocks are driven by fast coronal mass ejections (CMEs), the upstream turbulence is generated by heated shock plasma and by energetic particles themselves, the downstream reflection is provided by magnetic perturbations in the post-shock region. The process is operative high in the solar corona (above 2 – 4 Rs) and in the interplanetary (IP) medium, even beyond the Earth. The shock expands over a wide span of solar longitudes, so particles are accelerated throughout broad angular width and need not special coronal propagation. Actually, the SEP transport is coupled with the Alfvén wave generation, which is important for effective diffusion shock acceleration and the diffusion of SEP in space. There are strong observational evidences of the SEP-wave interaction in the interplanetary space, such as peculiar temporal variations of SEP elemental composition, streaming-limited intensities, and the spectral knee position [16]. It is clear that the transport effects can modify the spectral shape, especially in the low energy range [8].

In spite of success of the acceleration model based on the CME-driven diffusive shock acceleration coupled with processes of wave-particle interaction it is currently not known if such models can explain behavior of very energetic (relativistic) particles in powerful SEP events. Early arrival of first particles to the Earth in large SEP events requires development of a strong shock very close to the Sun (<10Rs) during very short time. However, near the Sun, the ambient Alfvén speed is so high, due to strong magnetic fields there, that a strong shock is difficult to achieve.

The SEP acceleration during magnetic reconnection

Magnetic reconnection in the solar corona is thought to release energy stored in solar magnetic fields and give rise

to solar flares [e.g., 17]. Dynamics in the large-scale coronal magnetic fields often results in the close disposition of the fields with opposite polarity giving origin to a current sheet. The plasma with the freezing-in magnetic field flows toward the neutral line and causes the opposite polarity magnetic field to collide and reconnect. The reconnection electric field in the current sheet is determined by the plasma inflow speed to the sheet u and the local magnetic field B: $E = -[u \times B]/c$. For the inflow speeds of $10^5 - 10^7$ cm s^{-1} and the magnetic fields of 10^2 - 10^3 G, the electric field can be as strong as a few hundred V cm^{-1}. This electric field can accelerate particles from the thermal up to relativistic energies provided their acceleration length (the particle displacement along the electric field in the current sheet) is $10^8 - 10^9$ cm for time less than 1 s. The spectral form, efficiency of acceleration, and the upper energy limit depend on the magnetic field topology [e.g., 18]. The energy spectrum of SEPs can be obtained from the particle trajectories modeling with resulting exponential [19, 20], power-law [18, 21], and more complicated shape [22]. It should be noted that both turbulence and shocks are generated during magnetic reconnection, i.e. conditions for shock and stochastic acceleration are also created near the reconnecting flux tubes in the solar flare region. Most probably, in majority of SEP events several mechanisms contribute to the SEP generation. Even widely accepted statement that impulsive events origin in a flare region whereas gradual events are product of coronal/interplanetary shock acceleration is valid only to a certain extent. The models are proposed that incorporate and combine various sites and mechanisms of acceleration [e.g., 23-29]. It is clear that the observed SEP energy spectrum is produced by many factors. Is it still possible to deduce any information on solar acceleration mechanisms from the observations? Since the mean free path of SEPs in the interplanetary space changes depending on time and distance from the Sun [8] the observed spectrum is distorted in comparison with the source one. Moreover, acceleration continues in the interplanetary space unless a shock becomes too weak, so the coming SEPs can actually be not of solar origin. However, the turbulence generated by SEP themselves ahead of a shock should depend on the SEP intensity. Weak SEP events are observed in reality, and these SEPs may not be accelerated by a shock, they generate only weak turbulence and their mean free part does not change during the transport from the Sun to the Earth. Then SEPs in weak events may be not very affected by a shock [26]. As was mentioned above, there is also no clear understanding if relativistic SEPs can be accelerated by the SME-driven waves promptly enough to match observational data. Therefore, it is worthwhile to examine the extremely SEP events and test them for various modes of SEP generation.

Extreme SEP event of 20 January 2005

In the following the powerful SEP event of 20 January 2005 is examined with the aim to derive information of the sources of observed SEPs There are rather many SEP observations during this extreme event. Here, the results presented at the last International Cosmic Ray Conference (the 29th ICRC, Pune, India, 2 – 10 August 2005) are overviewed (note, that the results are preliminary!). The main contribution to this ground level enhancement (GLE) observations was one from the world network of neutron monitors (NMs). Fig. 1 presents the minute values of count rate enhancement during the 20.01.2005 GLE at the NMs with different geomagnetic cut-offs *Rc* expressed as a percentage of the pre-event background. The neutron monitors situated in Antarctica (South Pole with enhancement of~5000%, and McMurdo with enhancement

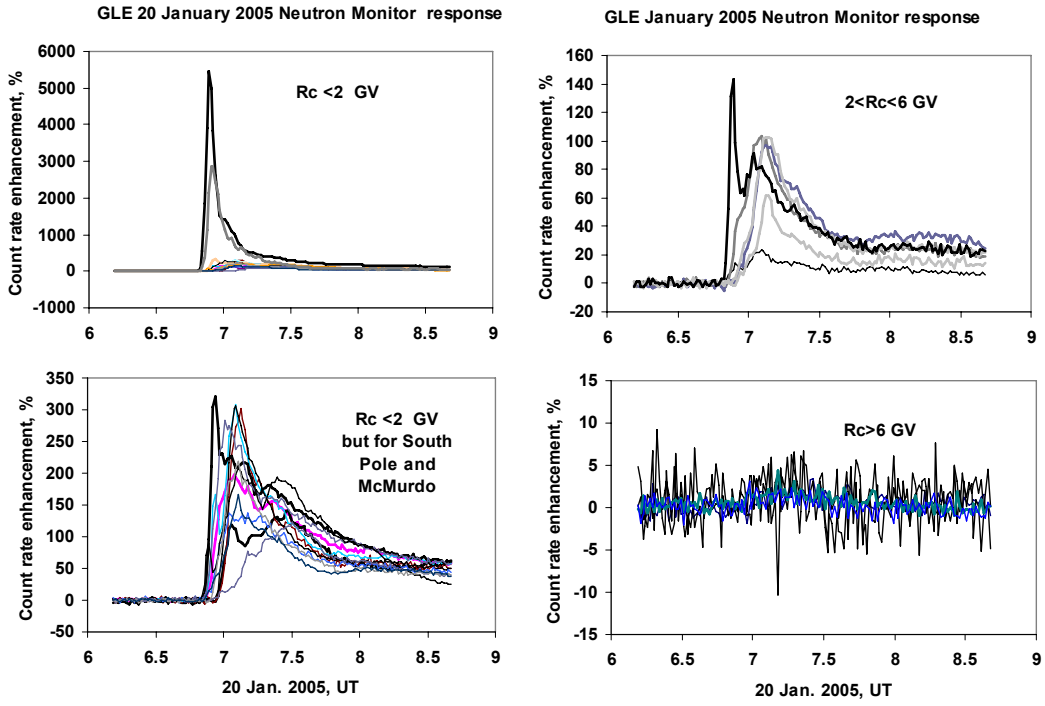

Fig.1. Count rate enhancement during the 20.01.2005 GLE at the neutron monitors with different geomagnetic cut-offs Rc expressed as a percentage of the pre-event background.

of~3000%) were the first to get a very sharp and highly anisotropic signal [30]. It is seen from Fig. 1 that the other NMs with low *Rc* demonstrated significantly lower (although still high comparatively with majority of SEP events) amplitude because of very narrow solid angle of SEP arrival in the beginning of event. Strong anisotropy was observed during almost one hour. The NM stations with *Rc* > 6 GV showed hardly discernible signal. However, using the Carpet detector of an extensive atmospheric shower (EAS) installation at Baksan (*Rc*=5.7 GV) allowed Ref. [31] to obtain the amplitude of enhancement 43.30±0.03%.

Reconstruction of SEP fluxes, energy spectra and anisotropy was done on the basis of methods [32] by several groups and is given in Table 1. It appeared that SEP features changed rapidly during first 10 – 15 minutes. Energy spectra as estimated by different authors are in reasonable agreement. The first solar protons arrived in narrow beam and had unusually hard energy spectrum which became rather typical during about 5 minutes. Simultaneously, the cone of particle arriving became rather wide as it can be seen in Fig. 1 at the enhancement time-profiles. A direction to the bulk particle source seems also not to be constant, although results of different authors are not quite consistent (see Table 1).

Ref. [33, 34] found two SEP sources, their contributions being changed during the event. A prompt coming component (indicated by "P" in Table 1) with an exponential spectrum form was interpreted as accelerated in the reconnecting current sheet in a low coronal magnetic field, whereas a delayed component ("D" in Table 1) with a power-law spectrum, as accelerated by a stochastic mechanism at the MHD turbulence in expanding flare plasma. The apparent direction to the SEP source was different for the prompt and delayed components.

Ref. [35] analyzed temporal and directional features of 20 January event using numerical solutions of the Fokker-Plank equation for particle transport. It appeared possible to reconcile all the observed GLE characteristics assuming that there was a single source on the Sun, but the particle transport conditions in the interplanetary space changed rapidly. The mean free path value started as $\lambda = 0.9 \pm 0.1$ AU and decreased during several minutes to $\lambda = 0.6 \pm 0.1$ AU. This corresponded to the change in the solar wind turbulence spectral index from $q \approx 0.5$ to $q \approx 1.5$. The dramatic wave excitation was caused by the first SEPs themselves because of their extraordinary ample quantity in according with models of the wave-particle interaction [8]. Even in this case, the first arriving SEPs were not distorted by the changing conditions of the interplanetary transport.

TABLE 1

Feature of relativistic solar particles in GLE of 20 January 2005

Time, UT	Apparent source coordinates	Energy spectrum form	Ref.
0650 – 0655 Later	60±3°S, 69±7°E (GEO)	$\sim E^{-0.7\pm0.2}$ $\sim E^{-4}$	[36]
0650-0655 after 0730		$\sim P^{(2.5\text{-}5.7)}$ $\sim P^{-5}$	[30]
0653 – 0655 0655 – 0657 0657 - 0659 0659 – 0701	40°S, 310°E 50°S, 320°E 40°S, 320°E 50°S, 310°E (GEO)	$\sim P^{-4.5}$ $\sim P^{-7}$ $\sim P^{-7}$ $\sim P^{-6.5}$	[37]
	40°S, 320°E (GEO)		[38]
0700 0710 0730 0800	26°S, 242°E (P) 45°S, 332°E (D) 24°S, 243E°E (P) 67°S, 340°E (D) 17°S, 283°E (P) 7°S, 0° (D) 35°S, 9°E (D) (GSE)	~exp-(E/0.95 GeV) (P) $\sim E^{-4.8}$ (D)	[33, 34]

The parent flare of the GLE of 20 January 2005 was X7.1/2B at N12W58 from the active region 10720. The time history of the event is given in Table 2 together with solar time of phenomena occurrence. The solar wind velocity according to ACE measurement was around 800 km/s (taken before 0656 UT since there is no data during several hours after that), so the path along the Archimedean spiral was around 1.05 AU. Given the bulk of relativistic protons had energy of ~3 GeV, they travelled from the Sun to Earth during ~9 min. It is seen from Table 2 that the first relativistic protons left the Sun very soon after the start of high-energy gamma rays emission. So, the first SEPs were

TABLE 2

Timing of the solar events relevant to GLE of 20 January 2005

Phenomenon	Time on the Earth, (start-max-end), UT	Time on the Sun, UT	Reference
Soft X-rays (1-8Å)	0636-0701-0726	0628-0653-0718	http://sec.noaa.gov
Gamma rays 4-7 MeV (RHESSI)	0644-0646	0636-0638	[39]
Gamma rays 25-100 MeV (SONG, CORONAS-F)	0645	0637	[40]
Relativistic protons (South Pole, ~3 GeV)	0648.5-0653.5	0639.5-0644.5	[35, 39]
Type II	0644	0636	[41]
CME, height 3.48 Rs above the photosphere	0654	0645	[41]

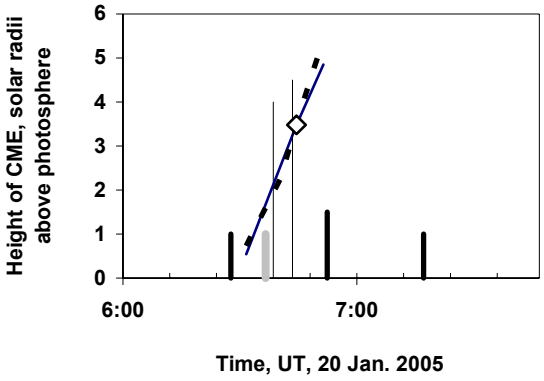

Fig.2. The CME trajectory on 20 January 2005 as reconstructed by Refs [41]- slanting line, and [41, 42] –dotted line. Vertical bars indicate solar time of the X ray burst start, maximum, and end (black thick); start of the 20-100 MeV gamma-ray emission (gray thick) [40]; solar times of the first arrival and flux maximum of SEPs as recorded by the South Pole NM [30] . Diamond shows the only direct measurement of the CME leading edge by LASCO.

very probably accelerated simultaneously with energetic particles interacted in the Sun. There was only one direct LASCO image of CME at 0654 with leading edge at 3.48 Rs above the photosphere. References [39, 41, 42] reconstructed the CME position vs. solar time which is plotted in Fig. 2 alongside with time of the first SEP departure and solar time of the flux maximum at the South Pole station. It is seen that CME was at the heights of ~ 2 Rs and ~ 3.5 Rs above the photosphere at the moments when a great amount of relativistic protons were emitted and reached the maximum flux value, respectively. According to Ref. [41], the average CME height values for these moments are ~3.4 Rs and ~11 Rs (above the photosphere). In addition, the intensity-time profiles show that bulk of relativistic particles was accelerated very rapidly and during short time. These features do not seem to be consistent with the CME-driven shock acceleration. Still, Ref. [41] argues for this acceleration mode as a source of the 20 January GLE. However, they took data of the Oulu NM for the time of the GLE onset which was 2.5 min later than onset at the South Pole.

The energy spectrum of SEPs is shown in Fig. 3. The solid lines give the "time-of-maximum" spectrum; the dots reflect the spectrum in the first stage of the event according to [33]. The first SEPs of the 20 January GLE were probably generated on the Sun simultaneously with particles interacted in the solar atmosphere and they were little, if at all, influenced by trapping and propagation effects in corona and interplanetary space. Rapid changes in the energy spectra during the first tens of minutes argue for evolution of the particle source and/or conditions of the SEP transport. Only the energy spectrum of the first arriving particles could provide information on the acceleration on the Sun (before 7000 UT). There is a consensus about hardness of this spectrum (see Table 1). However, Refs. [33, 34] fitted it by an exponent, whereas other authors defined it as a power-law. It is hardly possible to choose between the stochastic and magnetic reconnection mechanisms from these observations. The spectrum in the maximum of the intensity-time profile at 0715 UT (solid lines in Fig. 3) has probably little in common with the solar source of SEPs. Nevertheless, a TOM spectrum is a valuable SEP event characteristic especially for the applied aspects.

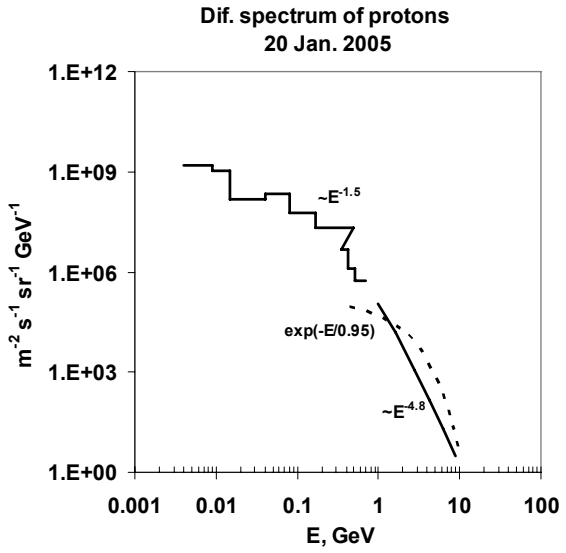

Fig. 3. Energy spectrum of solar protons on 20 January 2005 as measured by GOES11 at 0715 UT (broken line), and derived from the neutron monitors observations in the beginning of event at 0700 UT (dots, [33, 34]) and at 0715 UT (straight line [31]).

Conclusions

Both processes in the flare region during impulsive energy release (acceleration by DC electric fields and stochastic acceleration by fast shock waves or Alfvén waves generated at the magnetic reconnection site) and in the corona/interplanetary space (diffusive shock acceleration) contribute to the SEP energy spectrum formation. Moreover, SEP interaction with ambient plasma leads to Alfvén wave amplification, change in the particle mean free path, and spectrum distortion. Therefore, at time of the intensity maximum energy spectrum may include signatures of several episodes of acceleration and of diverse interplanetary conditions. It is hardly correct to induce the flare acceleration modes from the "time-of-maximum" spectrum, especially for the non relativistic particles. On the other hand, the first arriving energetic (especially relativistic) particles are little, if at all, influenced by the interplanetary transport and can give an insight into the solar processes. Timing is very important from both observational and modeling points of view. For example, the spectrum of the first particles in the 20 January 2005 event is likely a result of the acceleration in the flare region on the Sun, although it is hardly possible to choose a proper acceleration mechanism as yet. The "time-of maximum" spectrum in the large SEP events seems not to reflect acceleration on the Sun. However it is important as a convenient event characteristic, especially for the applied aspects. For a comprehensive analysis of the SEP sources, it is not enough to analyze energy spectrum alone; information on elemental and charge composition is necessary to be used [e.g., 5, 23]. Unfortunately, concerning the extreme SEP events and the most energetic energy range, such information is now scarce.

Acknowledgment

I would like to express my sincere gratitude to all the authors whose results were used for this overview. Valuable comments of A.I. Sladkova are highly appreciated. This work is partly supported by the Russian Foundation for Basic Research, grants 04-02-17380 and 05-02-16185 and partly performed for WG1/WP13000 of COST 724 Action.

REFERENCES

[1] Karpov S.N., Miroshnichenko L.I., Vashenyuk E.V. "The muon bursts with energy >200 GeV during GLE events of 21- 23 solar activity cycles" Proc. 29th ICRC, Pune, 2005, vol 1, pp197-200.

[2] McGuire R.E., von Rosenvinge T.T., "The energy spectra of solar energetic particles" *Adv. Space Res*., vol.4,2-3,1984,pp117-125

[3] Ellison D.C., Ramaty R. "Shock acceleration of electrons and ions in solar flares" Astrophys. J., vol.298,1985,pp400-408

[4] Gosling J.T "The solar flare myth" J.Geophys. Res. vol. 98,1993,pp18937-18949

[5] Reames D.V. "Particle acceleration at the Sun and in the heliosphere" Space Sci. Rev. vol.90,1999,pp413–488

[6] Lin R.P. "New RHESSI results on particle acceleration and energy release in solar flares" Proc. 28th ICRC, vol. 8,2004,pp335-345

[7] Miller J. A., Cargill P.J., Emslie A.G., et al. "Critical issues for understanding particle acceleration in impulsive solar flares" J. Geophys. Res. vol.102,A7,1997,pp14631-14659

[8] Ng C.K. Reames D.V., Tylka A.J. "Modeling shock-accelerated energetic particles coupled to interplanetary Alfvén waves" Astrophys. J., vol.591,2003,pp461-485

[9] Mazur J.E., Mason G.M., Klecker B., McGuire R.E. "The energy spectra of solar flare hydrogen, helium, oxygen, and iron: evidence for stochastic acceleration" Astrophys. J., vol.401,1992,pp398-410
[10] Selkowitz R., Blackman E.G. "Stochastic Fermi acceleration of subrelativistic electrons and its role in impulsive solar flares". Mon. Not. R. Astron. Soc., vol.354,2004,pp870-882.
[11]Tverskoy B.A. "On the theory of statistical Fermi acceleration", JETP, vol.52,2,1967, pp483-497 (in Russian)
[12]Petrosian V., Liu S. "Stochastic acceleration of electrons and protons. I. Acceleration by parallel-propagating waves" Astrophys. J., vol.610,2004,pp550-571
[13] Berezhko E.G., Elshin V.K., Krymsky G.F. Petukchov S.I. *Cosmic ray generation by shocks*. Nauka publ. house, Novosibirsk, 1988, 182 p. (in Russian).
[14] Axford W.I., Leer E., Skadron G. "The acceleration of cosmic rays by shock waves" Proc. 15th ICRC, vol.11,1977,pp132-137
[15] Krymsky G.F. "A regular mechanism for the acceleration of charged particles on the front of a shock wave" Doklady Akad. Nauk. vol.234,1977,pp1306-1308 (in Russian)
[16] Tylka A.J. "New insights on solar energetic particles from Wind and ACE" Journ. Geophys. Res., vol.106,A11,2001,pp25333-25352
[17] Sakai J.-I., de Jager C. "Solar flares and collisions between current-carrying loops", Space Sci. Res., vol.77,1-2,1996,pp1 – 192
[18] Litvinenko Y.E. *Energy conversion and particle acceleration in solar corona.* Ed. by L.Klein, Lecture Notes in Physics, vol.612,2003,pp.213-229
[19] Bulanov S.V., Sasorov P.V. "Energetic spectrum of particles accelerated in the vicinity of the zero line of a magnetic field" Astronomichesky J., vol.52,4,1975.pp763-771 (in Russian)
[20] Balabin Y.V., Vashenyuk E.V., Mingalev O.V., Podgorny A.I., Podgorny I.M. "The spectrum of solar cosmic rays: observational data and model computations", Astronomichesky J., vol.82,10, 2005,pp940-949 (in Russian).
[21] Wood P. and Neukirch T., "Electron acceleration in reconnecting current sheets", Solar Physics, vol.226,2005,pp79-95
[22] Zharkova V., Gordovskyy M. "Energy spectra of particles accelerated in a reconnecting current sheet with the guiding magnetic field", Mon. Not. R. Astron. Soc., vol.356,2005,pp1107–1116, doi:10.1111/j.1365-2966.2004.08532.x.
[23] Cane H.V. "Are there two classes of solar energetic particle events?", Proc. 27th ICRC, 2001,3231-3234
[24] Cane, H. V., T. T. von Rosenvinge, C. M. S. Cohen, and R. A. Mewaldt "Two components in major solar particle events", Geophys. Res. Lett., vol. 30,12, SEP5,2003,pp1-4,8017, doi:10.1029/2002GL016580
[25] Kocharov L., Torsti J., Latinen T., Tettinen M. "Post-impulsive-phase acceleration in a wide range of solar longitudes", Solar Physics, vol.190,1999,pp295-307
[26] Kocharov L., Lytova M., Vainio R., Laitinen T., Torsti J. "Modeling the shock aftermath source of energetic particles in the solar corona", Astrophys. J., vol.620,2005,pp1052-1068
[27] Li G., Zank G.P. "Mixed particle acceleration at CME-driven shocks and flares" Geophys. Res. Lett., vol.32,2,L02101,2005,pp1-4, doi;10.1029/2004GL021250.
[28] Livshits M.A., Belov A.V. "When and where are solar cosmic rays accelerated most efficiently?", Astronomichesky J., vol.81,8,2004,pp732-745 (in Russian).
[29] Turkmani R., Vlahos L., Galsgaard K., Cargill P.J., Isliker H. "Particle acceleration in stressed coronal magnetic fields", Astrophys. J., vol.620,2005,L59-L62
[30] Bieber J.W., Clem J., Evenson P., Pyle R., Duldig M., Humble J., Ruffolo D., Rujiwarodom M., Sáiz A. "Largest GLE in Half a Century: Neutron Monitor Observations of the January 20, 2005 Event", Proc. 29th ICRC, Pune, 2005, vol. 1, pp.237 -240.
[31] Karpov S.N., Karpova Z.M., Balabin Yu.V. and Vashenyuk E.V. "Study of the GLE events with use of the EAS-arrays data", Proc. 29th ICRC, Pune, 2005, vol. 1, pp.193 -196.
[32] Shea M.A., Smart D.F. "Possible evidence for rigidity-dependent release of relativistic protons from the solar corona", Space Sci. Rev., vol.32,1982,pp251-271
[33] Vashenyuk E.V., Balabin Yu.V., Bazilevskaya G.A., Makhmutov V.S., Stozhkov Yu.I., Svirzhevsky N.S. "Solar Particle Event 20 January, 2005 on stratosphere and ground level observations", Proc. 29th ICRC, Pune, 2005, vol.1, pp.213-216.
[34] Vashenyuk E.V., Balabin Yu.V., Gvozdevsky B.B., Karpov S.N,. Yanke V.G., Eroshenko E.A, Belov A.V., Gushchina R.T. **"**Relativistic solar cosmic rays in January 20, 2005 event on the ground based observations", Proc. 29th ICRC, Pune, 2005, vol.1, pp.209-212.
[35] Sáiz A., Ruffolo D., Rujiwarodom M. , John W. Bieber J.W. , Clem J., Evenson P. , Pyle P. , Duldig M.L. , Humble J.E. "Relativistic Particle Injection and Interplanetary Transport during the January 20, 2005 Ground Level Enhancement", Proc. 29th ICRC, Pune, 2005, vol.1, pp.229-232..
[36] Belov A.V., Eroshenko E.A., Mavromichalaki H., Plainaki C., Yanke V.G. "Ground level enhancement of the solar cosmic rays on January 20, 2005", Proc. 29th ICRC, Pune, 2005, vol.1, pp.189-192.
[37] Flückiger E.O., Bütikofer R., Moser M.R., Desorgher L. **"**The Cosmic Ray Ground Level Enhancement during the Forbush Decrease in January 2005" Proc. 29th ICRC, Pune, 2005, vol.1, pp.225-228.
[38] Moraal H., McCracken K.G., Schoeman C.C., Stoker P.H. **"**The Ground Level Enhancements of 20 January 2005 and 28 October 2003" Proc. 29th ICRC, Pune, 2005, vol.1, pp.221-224.
[39] Simnett G.M., E.C. Roelof E.C. "Timing of the relativistic proton acceleration responsible for the GLE on 20 January, 2005".Proc. 29th ICRC, Pune, 2005, vol.1, pp.233-236.
[40] Kuznetsov S.N., Kurt V.G., Yushkov B.Yu., Myagkova I.N., Kudela, K., Kaššovicová J., Slivka, M. "Proton acceleration during 20 January 2005 solar flare: CORONAS-F observations of high-energy gamma emission and GLE". Proc. 29th ICRC, Pune, 2005, vol.1, pp.49-52.
[41] Gopalswamy N., Xie H., Yashiro S., Usoskin I. "Coronal Mass Ejections and Ground Level Enhancements". Proc. 29th ICRC, Pune, 2005, vol.1, pp.169-172.
[42] Mewaldt R.A., et al., **"**Solar-Particle Energy Spectra during the Large Events of October-November 2003 and January 2005" Proc. 29th ICRC, Pune, 2005, vol.1, pp.111-114.

Evolution and Flare Productivity of Active Region with Solar Extreme Events of the Current 23 Solar Cycle

V.N. Ishkov

Institute of Terrestrial Magnetism, Ionosphere and Radio Wave Propagation of Russian Academy of Sciences, Troitsk,Russia,ishkov@izmiran.ru

The current solar cycle under all characteristics fall in cycles of average size. However and in such cycles we have an opportunity to observe solar extreme flare events. First of them was observed in the beginning of April, 2001 when extreme flare activity was occurrences in two, carried almost on 180° of heliolongitude, sunspot groups AR9393 (N20L152) – X>17.5 2 April 2, 2001, and AR9415 (S22L359) – X14.4 April 15, 2001. But in a current solar cycle flare activity has reached the greatest concentration during 19.10 - 05.11.2003 when a visible disk of the Sun there passed at once three greater and flare-active sunspot groups. Solar extreme flare events are connected with AR10486 (S16L286) that has developed in greater sunspot group on the visible hemisphere of the Sun. In that active region has occurrence the powerful solar flares of X17.3/4B 28.10 and X10/2b 29.10. The following period flares realization in given sunspot groups has begun 02.11 flare of X8.3/2B and has proceeded 4.11 most intensive on a flux of soft x-ray radiation in a current cycle flare of important X>17.5 (X28)/3B. Last flare has occurred near to western limb the Sun and essential influence on geomagnetic conditions have not rendered, however solar proton events of class S3 and S2 were carried out (maxima 2 and 4.10 accordingly). On September 7, 2005 the next flare-active region has appear on a visible disk of the Sun and the same day in it there was a fourth superflare on x-ray importance X17.1/3B. Till 17.09 in it was realized 11 large flares of a importance of X. Similar powerful burst of flare activity in 5.5 years after a maximum of a solar cycle were carried out was observed only second time: first such case was observed in solar cycle20 in July, 1974.

Introduction

Solar Cycle 23 began in June 1996 and its evolution has shown that our knowledge of long–duration active processes in the Sun is insufficient to confidently predict the next 11-year cycle. The basic stages of development the current 23 cycles of solar activity the following [1]:

– the minimum of 22 solar cycle - May 1996 (W* = 8.0);

– the beginning of a growth phase 23 (current) cycles of solar activity – September, 1997;

– the maximum of relative number of solar spots - April, 2000;

– the epoch of global solar magnetic sign reversal – July – December, 2000;

– the secondary maximum of the solar spots relative number – November, 2001;

– a maximum of a radio emission flux on a wave of 10.7 cm – February, 2002;

– phase of a maximum 23 (current) solar cycle – October 1999 – June, 2002;

– the beginning of a phase of decrease of the current solar cycle – July, 2002;

– the probable point of a minimum of the current solar activity cycle – November 2006.

The active regions with solar extreme events

The aim of this paper was to study of active regions characteristic in which solar extreme events has occurrence and it's compared with similar events in other solar cycles.

Definition of solar extreme events entirely and completely depends on those effects in Earth's environment or in any points of a heliosphere, which makes the solar active phenomenon. The history of observation of the active phenomena on shows, that in absolutely overwhelming majority of cases is powerful flare event. Now terrestrial disturbances can be estimated in the following kinds of his reaction to powerful solar influence [2]:

1. R: on electromagnetic shock – "electromagnetic impact", is inherent only in solar flares, develops at the moment of realization of solar flare and is estimated on influence on an ionosphere (R1 – R5).
2. S: on intensity of a stream of the charged particles (basically of protons with E>10 MeV) – in overwhelming number of cases significant fluxes of protons are consequence of processes in solar flare event (flare) (S1 – S5).
3. G: on geomagnetic disturbance which develops through 1 – 4 day after solar flare events (flares, filaments ejection) which develops in reply to arrival to the Earth the disturbance structures of a solar wind from this event or passage of high-speed fluxes by the Earth from solar coronal holes (G1 – G5).

Therefore it is natural to define solar extreme events as large powerful flare events, disturbances from which maximal influences by all three classes of disturbances (R, S, G). However 2 and 3 phenomena essentially depend on localization solar flare events and at adverse, for example, solar limb localization even the most powerful flare events, consequences of his realization for environment will be expressed or only in an "electromagnetic impact" (R) for E-limb flare event, or in R and S – for W-limb flare event.

For 9.5 years of development of the current solar cycle it is registered only six flares with a X-ray importance X≥10 (for example, 1 – 15 June, 1991 only, its was 6). Three of them were the main one during the concerned of greatest flare activity in current solar cycle that occurred for a full 15 days in October and November 2003. In table 1 we result the list of the most intensive solar flares in a range (1 – 8 Å = 12.5 – 1 keV) of the current solar cycles. Here the situation even more gets confused, as the X-ray detectors established on various US GOES satellites for measurement of a fluxes of soft X-ray radiation in the range (1 – 8 Å), had a different threshold of saturation. Till 1976 the threshold of saturation corresponded to X ≥ 5.4 and consequently the well-known flares on August 4 and 7 1972 had a formal

point X≥ 5.4, then up to 1996 – X≥12.5. After 1996 the threshold of saturation has grown up to X ≥ 17.5. In this case the X-ray importance is defined for flares proportionally time of saturation of X-ray detectors.

Table 1. The most powerful solar flares on X-ray

№	y/m/d	Imp.	τ	Localization	AR
1	*2003/11/04*	*X>17.5*	*11m (X28)*	*S19W83L286*	*10486*
2	*2001/04/02*	*X>17.5*	*~5m (X22+)*	*N19W90L152*	*9393*
3	*2003/10/28*	*X17.2*		*S16E08L286*	*10486*
4	*2005/09/07*	*X17.1*		*S12E89L229*	*10808*
5	*2001/04/15*	*X14.4*		*S20W85L001*	*9415*
6	*2003/10/29*	*X10.0*		*S15W02L286*	*10486*
7	1997/11/6	X9.4 γ GLE		S18W63L352	8100
8	*2003/11/02*	*X8.3*		*S14W56L286*	*10486*
9	2005/01/20	X7.1 γ GLE		N15W56L177	10720
10	2001/12/12	X6.3		S09E16L020	9727
11	*2005/09/09*	*X6.2*		*S10E58L229*	*10808*
12	2000/07/14	X5.7 γ		N22W07L320	9077
13	*2001/04/05*	*X5.6 γ*		*S21E31L001*	*9415*
14	*2003/10/23*	*X5.4*		*S21E88L286*	*10486*
15	2001/08/25	X5.3 γ		S17E34L296	9591
16	*2005/09/08*	*X5.4*		*S14E74L229*	*10808*

Italics allocates flares in active regions (AR) with extreme flare events: AR9393 March, 2001, AR9415 April, 2001, AR10486 October - November, 2003 and AR10808 September, 2005; Imp – X-ray importance of the solar flare; τ - time of soft x-ray detector saturation.

Therefore would be to characterize an X-ray importance of such flares with saturation not only threshold value of the X-ray detectors, but also duration of a time interval of saturation of X-ray detectors more objectively. Unfortunately, in the literature not for each powerful flare it is possible to find these data, and in most cases for such flares the estimated soft X-ray importance is underlined. Extrapolation of an X-ray importance for very large flares with long saturation is hardly justified.

In table 2 the list of the current cycle most powerful flares on a total integrated fluxes in a range of soft X-ray radiation in a range (12.5 – 1 keV) are resulted.

Table 2 The most powerful solar flares on total integrated fluxes

Date	to	Imp.	Localization	AR	∑Φ (J/m²)
07.09.2005	1717	X17.1/3B	S12E89L229	10808	2.60
04.11.2003	1929	X>17.5/2B	S19W83 L286	10486	2.30
28.10.2003	0951	X17.2/4B	S16E08 L286	10486	1.80
09.09.2005	1913	X6.2/2B	S10E58L229	10808	1.70
02.04.2001	2132	X>17.5/–	N19W90 L152	9393	1.50
28.12.2001	1934	X3.4/–	S28E90L018	9767	1.3
20.01.2005	0635	X7.1/3B	N15W56L177	10720	1.3
02.11.2003	1703	X8.3/2B	S14W56L286	10486	0.91
29.10.2003	2037	X10/2B	S15W02L286	10486	0.87
17.01.2005	0659	X3.8/2B	N15W25L179	10720	0.84
25.08.2001	1623	X5.3/3B	S17E34L296	9591	0.82
14.07.2000	1003	X5.7/3B	N22W07L320	9077	0.75

The first superflare of a current solar cycle has occurred in the large, second-largest area, sunspot group AR9393 (N18L151), when it has practically passed a visible disk of the Sun. Emergence of a powerful new magnetic flux in this sunspot group has begun on March, 26th and, by March, 29th, the area of sunspot group has increased in 2.3 times, having reached size 2440 m.v.h. But the bulk of flares in the given active region occurred April 2nd when for 21 hour 3 flares of importance X among which there was a extreme flare of importance X> 17.5 have been registered. In view of soft X-ray detector time saturation for GOES-9 (τ ~5m), a calculated importance the flare reach of X22. Localization of flare on a visible disk of the Sun practically excluded significant influence on a geomagnetic field and influence on space environment it was limited to powerful electromagnetic impact (R5) and solar proton event by intensity S3. However disturbance from the large flare of importance X1.7/1N on March 29th, 2001 has caused in environment severe magnetic storm (G5) 31.03 - 1.04.

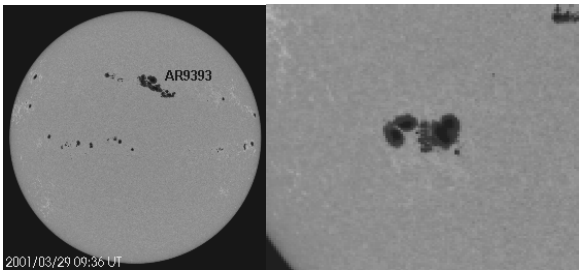

Fig 1 Sunspot groups 2001, March – April: AR9393 29.03 (left) and AR9415 06.04.2003 (right), (SOHO MDI).

The April 1st, 2001 on a visible disk of the Sun there was active region AR9415 (S22L359), in which during passage it was carried out three flare-active periods. During last of them near to western limb at April 15th there was a powerful solar flare X14.4/2B, which in environment has caused disturbances R5 and S2. In total for 18 days in these two active region 13 large flares were carried out, 9 from which had importance X. In the sum these carried on 200° active regions a distance, given powerful heliospheric storm of the end of March – the beginnings of April 2001. Only in space environment during of period 25.03 - 10.04 was arrival of 6 interplanetary shocks, 5 magnetic storms and 7 solar proton event are registered.

Starting on October 18th, 2003 solar activity increased gradually due to the apparition of AR 10484 (N05L353 – 2nd rotation AR10464) at the east solar limb. This sunspot group, with gamma-beta-delta magnetic configuration, started its first major flaring sequence on October, 19th with an M1.9 at 0626, an X1.1 flare at 1650 and an M1.0 flare at 1926, the start of period of extreme solar and space weather activity. A partial halo CME on October 19th, 2003 was first seen in northeast quadrant at 1708 after X1.1 flare. Both an EIT wave and coronal dimming were observed in conjunction with this event. This halo CME resulted in a minor geomagnetic storm on Oct. 22. After of the new powerful magnetic flux emerges 26.10 its area increased up to 1700 m.v.h., and two more large flares (X1.2/2N and M7.6/2N) was occurrences. Then 29.10 this active region passed the western limb in full development. After 21.10 on a visible disk of the Sun of the large sunspot group AR10486 (S16L286) appearances [3]. 23.10 in it there were flares X5.4/1B and X1.1/1N and 24.10 – flares M7.6/1N was occurrences. A full halo CME on October 23rd observed at 0854 after X5.4 flare. The mean plane-of-sky speed for this event was 1110 km/s. A very large EIT wave and coronal dimming were observed in association with this event. This event caused a major geomagnetic storm on 24.10 after arrival of a shock. October, 24th-25th in this AR there was a first observable emergence of the powerful magnetic flux increased the area of sunspot group on 800 m.v.h. (Sp=2200 m.v.h.), which consequence were flares X1.2/3B (26.10), M5.0/1F and M6.7/1F (27.10). Emergence of the following new magnetic flux (27 – 28.10), increased the area of sunspot group up to record value for the current cycle – Sp=2610 m.v.h. (>0.25% of the solar disk), it has

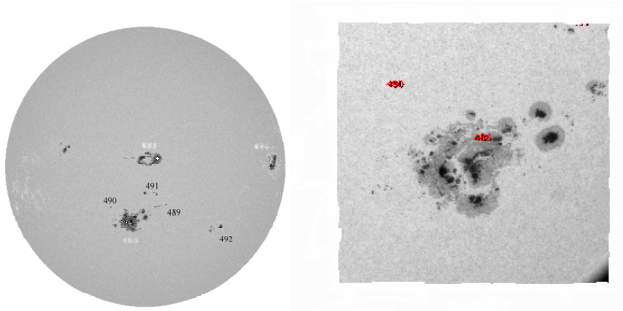

Fig.2. Sunspot groups 2003, October: the view of the Sun on 28.10.2005 (left), AR 10486 at 30.10.2003 (right) (SOHO MDI.)/

allowed to be carried out to flare X17.3/4B 28.10 and X10.0/2B 29.10.

The following period flares occurrence in the given AR began 02.11-flare X8.3/2B, coronal dimming and EIT wave were observed in association with this event. Although this event occurred close to the western limb, the accompanying CME developed into a full halo with estimated plane-of-the-sky speed about 2100 km/s. The most buoyant day, however, was Nov 4, when AR 10486 generated extremely intensive flare X> 17.5/3B that was later estimated to have reached an X28 peak of soft X-ray flux. Last flares have taken place near to western limb the Sun and essential influence on geomagnetic conditions have not made, however solar proton events of class S3 and S2 were carried out. Six distinct proton events can be discerned during this stormy period. The largest was the 29 500 p.f.u. (E>10-MeV) proton event Oct. 28-29 following the X17 flare (S4). This severe storm was the second largest proton event in current solar cycle.

On HESSI [4] and KORONAS-F [5] data for the given period 8 hard X-ray bursts in a range 7 - 200 MeV were registered. Super hard burst observed in limb flare X5.4/1B 23.10/0819, flare M1.2/2N 25.10/0415, large flare M6.7 27.10/1227 and a third on intensity of X-ray flare X8.3/2B 2.11. All listed flares have taken place in AR10486. Three γ-ray bursts are registered during flare X17.2 28.10 and generation of gamma radiation began in an hour (08:50:48) prior to the beginning of flare in optics and soft X-ray ranges.

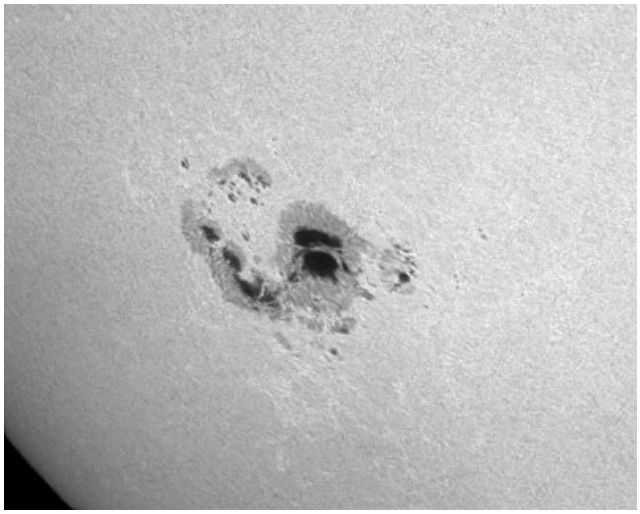

Fig. 3. Sunspot groups AR 10808 of September 9, 2005 (SOHO MDI)

On October 27th, 2003 on a center of visible solar disc has born AR 10488 (N08L291). This active region was with very rapid developing. For the third day of the existence the AR has reached the area 1750 m.v.h., class FKC and δ – a magnetic configuration that has allowed it 3.11 to occur two large flares (X2.7 and X3.9). In total for 16 day in these 3 active regions 16 large flares were carried out, 11 from which had x-ray importance X.

In the beginning of September, 2005 helioseismology methods had been certain passage of the big sunspot group on an invisible hemisphere of the Sun. On September 7th it has appear on a visible disk of the Sun and the same day in it there was a fourth superflare on importance X17.1/3B. Active region 10808 has been a big surprise: this region, has presented us in a 10-day period with 11 X-class flares and 19 M-class flares. Similar powerful burst of flare activity in 5.5 years after a maximum of a solar cycle were carried out was observed only second time: first such case was observed in solar cycle20 in July 1974 (Table 4,).

The basic development of sunspot group AR10808 has occurred near east solar limb, therefore it is impossible to describe parameters of a magnetic flux which has given such power output, but possible to assume, that its capacity and speed of emergence was we shall compare to a magnetic flux in active region AR9393 of March, 2001. Table3 give the basic characteristics considered above flare-active regions.

For the characteristic of sunspot group gives its serial number in system of Service of Sun NOAA; localization (N, S for heliolatitudes and L absolute heliolongitudes); the area of spots (Sp max); evolutionary and magnetic classes in a maximum of development. Further are resulted flares the characteristics including flare potential of AR: – X-ray flare index; – the total quantity of flares of X-ray importance X+M+C, the bottom index shows quantity of flares of the given importance, and the top index shows importance of the largest flare on intensity soft X-ray; total quantity of flares of optical importance; – the periods of large and middle flare concentration in dates, hours and the quantity of flares, the top index gives importance of greater flares.

TABLE 3 Evolutionary and flare characteristics of active regions with extreme solar flares in the current 23 solar cycle

AR 9393 (N17L151, ПЦМ 28,0.03.2001); Sp max = 2440 м.д.п., FKC, δ; *XRI=>25.74 (30.24):* $X_4^{>17.5}+M_{24}+C_{28}$; $2_2+1_{15}+S_{101}$; *ПВЭ I* (43^h) – *28 – 29.03* – $X_1^{1.7}+M_{11}$; *ПВЭ II* (21^h) – *02.04* – $X_3^{22}+M_4$;
AR9415 (S22 L359, ПЦМ 9.04.2001) Sp max= 880 м.д.п., EKI, δ; *XRI=28.73:* $X_5^{14.4}+M_7+C_{15}$; $3_1+2_4+1_4+S_{34}$; *ПВЭ I* (64^h) – *3 – 5.04:* X_2+M_2; *ПВЭ II* (65^h) – *9 – 12.04:* X_2+M_3; *ПВЭ III* (20^h) – *14 – 15.04:* $X_1^{14.4}+M_1$;
AR 10486 (S17L283, ПЦМ 29,3.10.03); Sp max = 2610 м.д.п., FKC, δ; *XRI>62.56:* $X_7^{>17.5}+M_{16}+C_{16}$; $4_1+3_2+1_7+S_{49}$; *ПВЭ I* (59^h) – *22 – 24.10* – $X_2^{5.4}+M_6^{9.9;7.6}$; *ПВЭ II* (59^h) – *27 – 29.10* – $X_2^{17.4;10}+M_4^{5;6.7}$; *ПВЭ III* ($63^h$) – *02 – 05.11* – $X_2^{8.3;>17.5}+M_6^{5.3}$;
AR 10808 (S09L229, ПЦМ 14,4.09.05; R2; Sp max = 1430 м.д.п., EKC, δ; *XRI =49.21:* $X_{11}^{17.1}+M_{24}+C_1$; $3_1+2_9+1_{12}+S_{70}$; *ПВЭ I* (91^h) – *7 – 10.09* – $X_7^{17.1}+M_{12}^{6.2}$; *ПВЭ II*(94^h) – *12 – 16.09* – $X_4^{1.7}+M_7^{6.1}$

Table 4. Mostly flare productive active regions 1970 – 2003 .

№	CMP	AR	Φ°	L°	Sp max	R, S, G	XRI	M±y
1	09 VI 1991	6659	N31	248	2300	R5/S4/G4	>86.5	+2
2	***29 X 2003***	***10486***	***S17***	***354***	***2610***	***R5/S4/G5***	***>62.56***	*+3.5*
3	12 III 1989	5395	N34	257	3600	R5/S4/G5	57.0	-0.5
4	***14 IX 2005***	***10808***	***S09***	***229***	***1430***	***R5/S3/G3***	***49.21***	*5.5*
5	08 VI 1982	3763	S08	086	1270	R4/S2/G2	42.4	+2.5
6	04 VII 1974	0433	S14	156	1334	R4/S3/G5	≥41.4	+5.5
7	16 XII 1982	4025	S06	089	500	R4/S2/G3	36.7	+3
8	23 III 1991	6555	S23	188	2530	R4/S5/G4	32.6	+1.5
9	15 VII 1982	3804	N14	322	2960	R4/S4/G5	31.6	+2.5
10	14 VII 1978	1203	N18	170	1600	R5/S2/G2	29.7	-1
11	***10 IV 2001***	***9415***	***S22***	***359***	***880***	***R4/S3/G4***	***28.73***	*+1*
12	08 VIII 1989	5629	S17	076	1320	R5/S4/G4	≥26.8	-0.5
13	04 VIII 1972	0331	N12	010	1330	R5?/S4/G5	≥26.0	+3.5
14	11 XI 1980	2779	S11	098	2000	R3/S1/G4	25.9	+1
15	***28 III 2001***	***9393***	***N20***	***152***	***2440***	***R5/S2/G5***	***>25.74***	*+1*
16	17 V 1990	6063	N34	321	940	R3/S3/G2	23.1	+1
17	12 I 1989	5312	S31	308	1800	R3/S1/G2	22.4	-0.5
18	***15 I 2005***	***10720***	***N13***	***179***	***1630***	***R4/S3/G4***	***21.5***	*+4.7*
19	28 IV 1984	4474	S13	334	2160	R5/S3/G3	21.2	+5
20	18 VI 1982	3776	N13	312	3300	R4/S1/G1	18.8	+3

CMP - time of the central meridian active region passage; AR - number of active region in system NOAA; Φ° - average heliolatitudes of active region; L° - average a Carrington longitude of active region; XRI - the X-ray flare index (XRI); R, S, G - classes of the maximal events from flares in the given active region in the Earth's space environment; M±y - distance in years from a point of a solar cycle maximum (accuracy 0.5). Bold and italic allocates lines represents of the current 23 solar cycle active regions.

How can we compare this impressive solar region with other regions observed over the past thirty years? One method of comparison is to calculate the total output of X-ray flares by the region. This index, known as the X-ray flare index (XRI), adds together all the M and X class flares produced by the region with M1 flares counting as 0.1; M2 flares as 0.2; X1 flares as 1.0 and so on. Patrick McIntosh, a solar physicist with the NOAA SEL in Boulder Colorado, has compared the solar regions observed since August 1972. The following table 4 is based on his data.

Just the same, it is probable, that at such estimation the most intensive for all time of observations were X-ray flares on June 1991. Activity on the Sun during June 1991 was very impressive with a number of particularly energetic solar flares being observed. These powerful flares arose from one sunspot region – a large one that appeared on the eastern edge of the sun on June 01. This region, numbered AR6659, rotated across the visible disk of the Sun leaving the western edge on June 17. During of this time interval, AR 6659 produced some outstanding solar flares, including 5 flares, which were large enough to saturate the X-ray detectors satellites (June 1 and 6 the time of saturation was 26^m and yet at three flares of it was $\geq 17^m$). The region also produced an X10 flare, not far from this limit. Whilst previous solar regions have produced flares, which have saturated these detectors, no other region has produced more than one such flare. In producing 5 such flares, it is possible active region 6659 can, with justification claim to be the most important solar region in the last century.

Conclusion

Quantity of flare-active regions in a solar cycle of average size (23) remains approximately same as well as in high solar cycles (21, 22).

Intensity extreme flare events in a range (1 – 8 Å) does not depend on size of a solar cycle.

During too time a full flux for extreme flare event in the same range of radiation in a solar cycle of average size is much less, than in similar events high solar cycles. Let's notice, that the greatest integrated flux for all time of observation of soft x-ray radiation is registered from flare of importance X> 12.5 9 (X20) on August, 16th, 1989 - 6.70 J/m^2. In the lead flare (in table 2) 07.09.2005 (X17.1) borrows only 8 place in the full list of flares for 1972 – 2005.

The rule proves to be true, that as a rule solar extreme events and the most significant flare-active regions appear on a phase of a solar cycle decrease. On the given statistics exception is 22 solar cycle in which such flare-active regions and extreme flare events were carried out in a phase of a maximum.

Acknowledgments

The author thanks the SOHO/MDI consortium for white-light MDI data and the HESSI team for data of flare catalog. This research supported by the grant of Russian Foundation for Basic Research 03-02-16384. and RAS Program No.30 "Solar activity and physical processes in the Solar-Terrestrial system".

References

[1] V.N. Ishkov . The Current 23 Cycle of Solar activity: Its Evolution and Principal Features, Proc. of ISCS 2003 "Solar Variability as Input to the Earth's Environment, Tatranska Lomnitsa Slovakia (ESA SP-535, Sept. 2003), p. 103-104.

[2] http://sec.noaa.gov/scale

[3] I.S Veselovsky, M.I. Panasyuk, M.I., et al., // Solar and Heliospheric Phenomena in October – November 2003: Causes and Effects, Cosmic Research, v.42, N5, 2004, p. 435 – 488.

[4] http://hercules.ethz.ch:8081/www/index.html

[5] S.N Kuznetsov, V.G. Kurt, I.N. Myagkova, B.Yu. Yushkov, K. Kudela, "High energy neutral emissions of large solar flares in the end of October, 2003", *Solar Extreme Events of 2003, Programme and Abstract Book, УНЦ ДО Москва 2004*, p33

Coupling of the CME Acceleration and the Flare Energy Release

D. Maričić[1], B. Vršnak[2], D.Roša[1], A. Veronig[3]

[1]*Astronomical Observatory Zagreb, Opatička 22, HR-10000 Zagreb, Croatia*

(e-mail: darije.maricic@zg.htnet.hr, drosa@hpd.botanic.hr*)*

[2]*Hvar Observatory, Faculty of Geodesy, Kačićeva 26, HR-10000 Zagreb, Croatia (e-mail:* bvrsnak@geodet.geof.hr*)*

[3]*Institute for Geophysics, Astrophysics and Meteorology, University of Graz, A-8010 Graz, Austria*

(e-mail: asv@igam.uni-graz.at*)*

We studied the relationship between the kinematics of coronal mass ejections (CMEs) and the energy release in the associated flares. For the analysis we have chosen ten events in which the basic CME structure was clearly recognizable already in the low corona during the pre-eruption slow-rise phase. Combining the data gained by the Mauna Loa Solar Observatory, the Large Angle and Spectrometric Corona-graphs and the Extreme Ultraviolet Imaging Telescope on-board the Solar and Heliospheric Observatory, we were able to measure the CME kinematics from the very beginning of the eruption up to the post-acceleration phase.

In summary, out of ten cases, five events (50%) showed a relatively good overlap of the CME acceleration phase and the impulsive phase of the flare. Such synchronization indicates that in these events, the CME acceleration and the flare energy release are strongly coupled physical pheno-mena. In two cases there was an obvious mismatch: in one of these event the CME acceleration took place before the impulsive phase of the flare, and in second one event the impulsive phase occurred before the CME acceleration. In three cases (30%) there was no noteworthy soft-X-ray enhancement.

Our analysis indicates that in the some events the CME acceleration and the flare energy release are strongly coupled physical phenomena, but in some events the relationship is less prominent.

Introduction

An interesting aspect of coronal mass ejections (CMEs) is their relation to solar flares. In particular, dynamical flares are a direct consequence of large-scale disruptions of the coronal magnetic field. Dynamical flares are caused by fast magnetic field reconnection that takes place in the current sheet formed in the wake of the CME [1].

A close relationship between a CME and a flare indicates that there is a coupling between the energy release in the flare and the bulk mass acceleration on the large scale. The energy release in flares is caused by the magnetic field reconnection of the field lines stretched by the eruption. The reconnection provides acceleration of nonthermal particle beams, and when the energetic particles precipitate into the transition region and chromosphere, they produce hard X-ray (HXR) emission through the Bremsstrahlung mechanism. The heated chromo-spheric plasma expands and fills up coronal loops, giving rise to the thermal soft X-ray (SXR) emission. As a result, the HXR curve is similar to the time-derivative of the SXR curve (the phenomenon known as "Neupert effect"; see, e.g., [6]).

The CME-flare relationship was recognized in several case studies. In [2], [4], [5], [7], [8], [9], and [10], the velocity of CME was compared with the flare energy release. In the case described in [5], the rapid CME acceleration occurred simul-taneously with the onset of the 1-8Å SXR burst. A similar situation was found in the event studied in [8]. Two out of three events presented in [4], showed the CME acceleration phase quite well correlated (±10min) with the rise of the 0.5-4 Å SXR burst, whereas in the third one the situation was not conclusive. In [9] and [10] a very detailed comparison of the CME acceleration and the corresponding SXR light-curves is presented. In the cases of the impulsive and the intermediate CME acceleration the time-derivate of the SXR light-curve was well-correlated with the impulsive phase of the associated flare. In the gradual cases, no associated SXR enhancement was recognized.

In this paper we present observations of ten well observed CME events, utilizing observations of the Mauna Loa Solar Observatory (MLSO), combined with the Large Angle and Spectrometric Coronagraphs (LASCO) and the Extreme Ultraviolet Imaging Telescope (EIT) onboard the Solar and Heliospheric Observatory (SOHO). The energy release in the associated flares was inspected using the data from the Geo-stationary Operational Environmental Satellite (GOES) and Yohkoh.

Observations

The FeXII 195Å images of EIT were employed to measure the height of the EUV coronal structures overlying the prominence in the early stages of the eruption. The data from the Soft X-Ray Telescope aboard the Yohkoh satellite were used to obtain additional information about the morphology of the hot component of the pre-eruption structure. The evolution of SXR flares was followed using images gained by the Soft X-Ray Telescope on board the Yohkoh satellite and the SXR flux measurements in the 1-8 Å and 0.5-4 Å channels of GOES.

The leading edges of CMEs were traced utilizing the white-light images gained by the MK-IV K-coronameter of MLSO and by LASCO onboard SOHO. Combining the field-of-view of the EIT, MK-IV, and LASCO, enables the investigation of the full kinematics of CMEs, including initiation, acceleration, and propagation phase.

In all events EIT images reveal a coronal arch-like structure overlaying the prominence. Seven out of the ten CMEs showed the regular three-part structure. Direct measurements of the initial CME evolution in the low corona were possible for all events, without applying any interpolation or extra-polation.

The propagation of the leading edge of CMEs was traced by measuring the plane-of-sky heliocentric distance, r. The value of r was determined from images gained by different instruments, so the data were first joined, and then smoothed. From the smoothed data we have evaluated the velocities by taking two successive smoothed data points, as described in [3]:

$$v(t_{vi}) = (r(t_{i+1})-r(t_i))/(t_{i+1}-t_i) \quad , \quad (1)$$

where $t_{vi} = (t_{i+1}+t_i)/2$.

In the next step we estimated the accelerations by taking two successive velocitiy data-points, by applaying:

$$a(t_{ai}) = (v(t_{vi+1})-v(t_{vi}))/(t_{vi+1}-t_{vi}), \quad (2)$$

where $t_{ai} = (t_{vi+1}+t_{vi})/2$.

In Figs. 1-5 and Table I we show the results for five out of ten studied events, in order to to illustrate different types of the relationship between the CME kinematics and the energy release in the associated flares. Results for the remaining five events are given only in Table I, where we provide the SXR peak flux (*SXR*), the duration of the SXR growth (T_{SXR}), the maximum CME velocity and acceleration (v_{max}, a_{max}), the duration of acceleration (T_{acc}), and the offset between the acceleration peak and the maximum of the SXR-derivative ($\Delta t = t_{acc} - t_{dSXR}$).

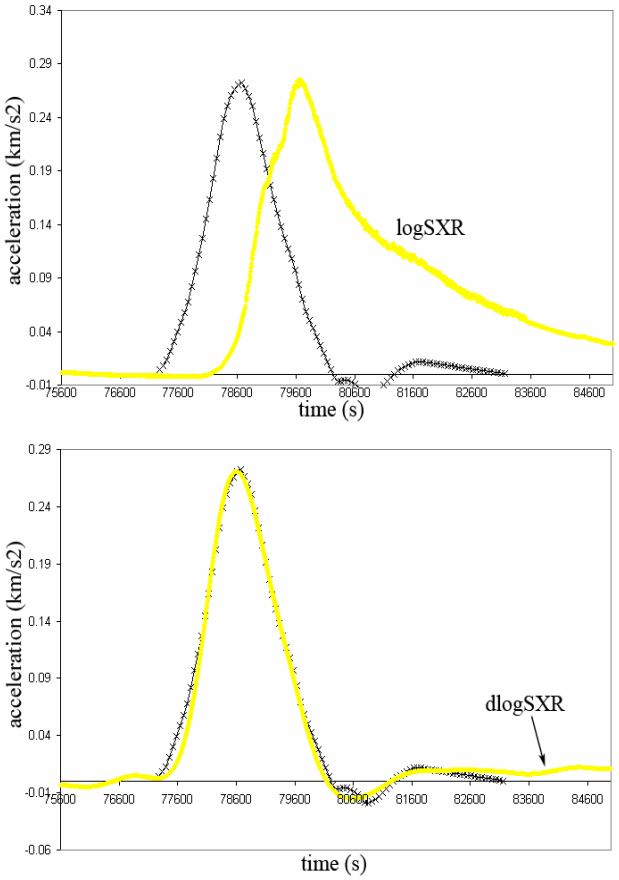

Fig. 1. Upper panel: The acceleration time-profile of the CME of 2002 March 09 and the flare time-profile of GOES X-ray flux (0.5-4Å channel). Lower panel: The logarithmic derivative of the smoothed SXR flux compared with the acceleration of the leading edge. There is a very good correlation between the CME acceleration and the SXR time-derivative. The acceleration maximum and the SXR time-derivative peak are contemporaneous to within a few minutes, indicating that the CME acceleration and the flare energy release are strongly coupled phenomena.

Figures 1-5 present the temporal correlation between the CME acceleration and the SXR flare bursts recorded in the GOES 0.5-4Å channel. In the upper panels of Figs. 1-5 we display the CME acceleration time-profile (solid line with crosses), together with the GOES X-ray logarithmic light-curve (bold gray line). In the lower panels we display the CME acceleration together with the logarithmic derivative

TABLE I

date	*SXR (1-8 Å)*	T_{SXR}*(h)*	v_{max} *(km/s)*	a_{max} *(ms^{-2})*	T_{acc} *(h)*	Δt *(min)*
23 Apr 2001	*/*	*/*	*370*	*40*	*6.5*	*/*
25 May 2001	*/*	*/*	*1050*	*300*	*1.9*	*/*
08 Jan 2002	*M0*	*1.9*	*450*	*120*	*2.7*	*12*
06 Jun 2002	*/*	*/*	*750*	*90*	*4*	*/*
09 Mar 2002	*M1.3*	*0.5*	*380*	*270*	*1*	*3*
16 Feb 2003	*C1.4*	*0.8*	*500*	*270*	*1.8*	*25*
18 Feb 2003	*B7.2*	*1.7*	*820*	*180*	*2.8*	*20*
15 Mar 2003	*B9.6*	*2.2*	*620*	*50*	*4*	*13*
15 Jul 2003	*B8.4*	*0.5*	*590*	*135*	*2*	*>3*
26 Oct 2003	*X2.1*	*1*	*1350*	*760*	*0.9*	*>2*

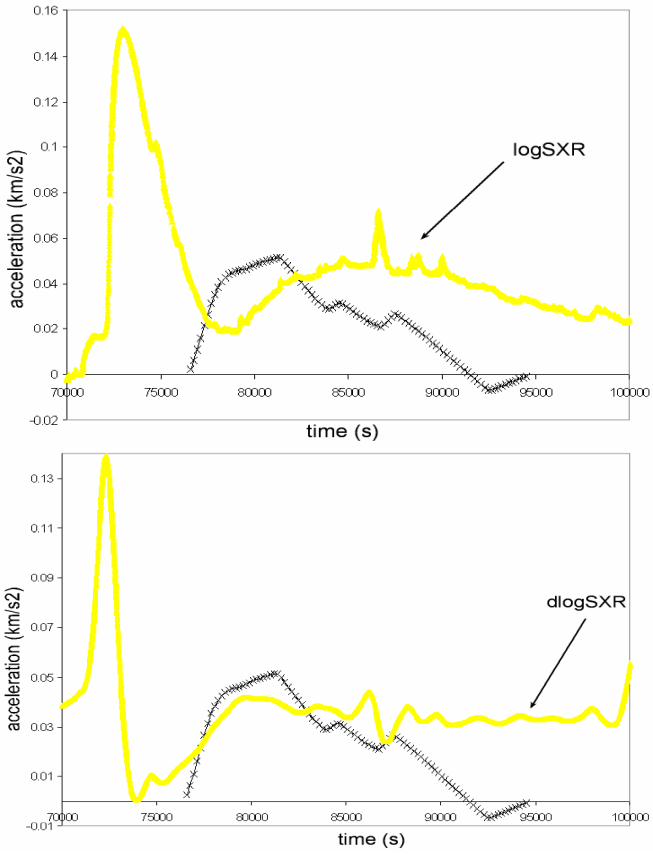

Fig. 2. The event of 2003 March 15. A relatively good correlation between the CME acceleration and the time-derivative of the SXR light-curve (peaks are separated by a few min) is somewhat obscured by presence of an earlier impulsive flare.

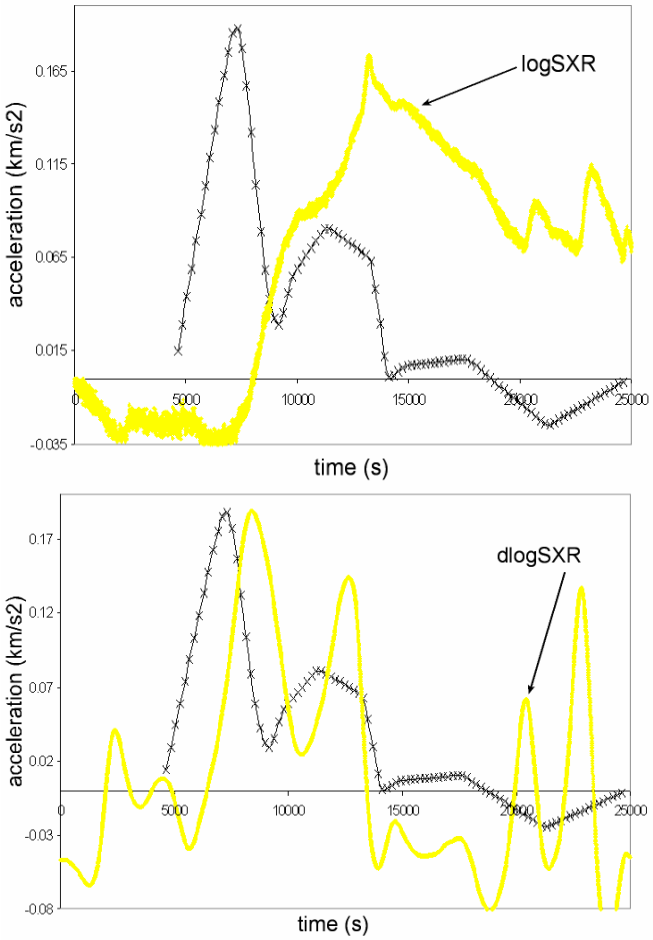

Fig. 3. The event of 2003 February 18. Note two peaks of acceleration and two peaks of SXR-derivative. Temporal difference between the main acceleration peak and the main SXR-derivative peak amounts to ≈ 20 min.

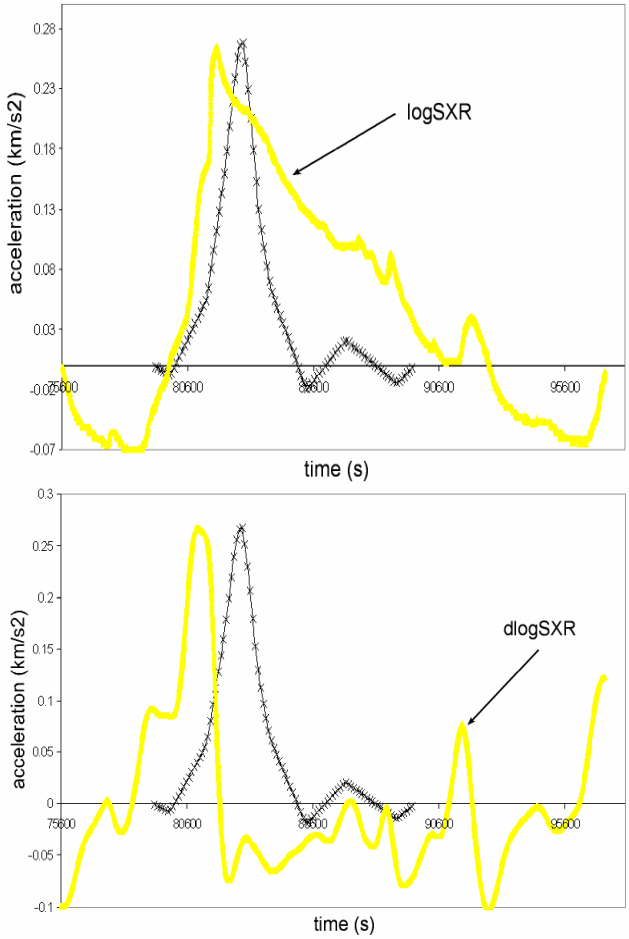

Fig. 4. The event of 2003 February 16. The SXR-derivative peaks about 25 min before the acceleration peak. The acceleration time-profile is similar to the SXR burst.

of the smoothed SXR flux, d(log*SXR*)/d*t*, (for details see [8]).

In Fig. 1 we present the event of 2002 March 09 to illustrate an almost perfect synchronization of the CME/flare evolution. The acceleration phase lasted for about 1 hr showing a rapid velocity increase from about 10 kms^{-1} at 21:30 UT to the peak value of 380 kms^{-1} at 22:20 UT. The CME attained the maximum acceleration a_{max}= 270 ms^{-2}, when the leading edge was at the height $h = 0.45r_{sun}$ above the limb.

In Fig. 2 we show another example of a rather well synchronized CME/flare evolution (2003 March 15). This was a gradual CME, characterized by very weak acceleration and low velocity throughout the LASCO field-of-view. The leading edge attained the velocity about 620 kms^{-1} after accelerating for more than 4 hours. The peak acceleration, a_{max}= 50 ms^{-2}, was attained when the leading edge was at the height $h = 2r_{sun}$. The CME was associated with a gradual flare of the GOES class B9.6.

In Fig. 3 we present the event of 2003 February 18, which showed a somewhat larger offset between the acceleration curve and the SXR-derivative, amounting to about 20 min. However, note that the acceleration exposes two peaks, consistent with the two peaks in the SXR-derivative.

In the event of 2003 February 16, presented in Fig. 4, we find a considerable difference between the CME acceleration and the SXR-derivative. The CME attained acceleration maximum of a_{max}= 270 ms^{-2} at the height $h = 0.8r_{sun}$, and was delyed for about 25 min after the SXR-derivative peak. The acceleration phase lasted for about 1.8 hours. Note that the acceleration time-profile is similar to the SXR light-curve.

In Fig. 5 we present the gradual CME event of 2001 April 23, characterized by very weak acceleration that lasted for about 6.5 hours. The frontal edge attained acceleration maximum of only a_{max}= 40 ms^{-2} at height $h = 0.8r_{sun}$. In this event there was no significant enhancement in SXR flux. SXR enhancement in the GOES data was not associated with eruption of this CME.

Out of the five remaining events (for details see Table I), the events of 2003 July 15, and the 2003 October 26 showed highly synchronized CME/flare evolution. Moreover, the former one showed a double-peaked acceleration and SXR-derivative (similar to that shown in Fig. 3, just with a considerably smaller delay). The event of 2002 January 08 can also be considered as an event of a relatively good synchronization, very similar to that shown in Fig. 2. In sum-mary, five out of ten events showed a CME/flare synchro-nization. The events of the 2001 April 23 and the 2003 March 25 did not show any noteworthy SXR enhancement.

Conclusion

The presented analysis we summarize as follows:

- The analyzed CMEs were characterized by accelerations ranging from several tens ms^{-2} up to almost a thousand ms^{-2}. The acceleration phase lasted from less than an hour to several hours.
- In five of ten events (50%) the acceleration of the CME is strongly correlated with the energy release in the associated flare. This is directly revealed by the close correlation of the CME acceleration time profile and the time derivative of the SXR burst light curve. In other words, the CME acceleration and the SXR burst show the Neupert-type of relationship. The average offset between acceleration and time-derivative SXR peaks in these five events adds up to approximately 6 min.
- In two out of ten events, there was an obvious mismatch. In one of these, the acceleration peak occurred much before the SXR-derivative peak. (e.g., in the CME of 2003 February 18 the acceleration peak occurred around 20 min before the SXR-derivative maximum). In the remaining case the SXR-derivative peak occurred before the acceleration peak.
- In the event of 2003 Feb 16, the acceleration time profile is similar to the SXR light-curve.
- In the event of 2003 February 18, the two acceleration peaks are accompanied by two peaks in the SXR-derivative, but the latter is delayed by some 30 min.
- Three out of ten events (30%) were not associated with any noteworthy SXR enhancement in the GOES data.

We would like to thank the GOES, MLSO, SOHO, and Yohkoh teams for developing and operating the instruments and we are grateful for their open data policy.

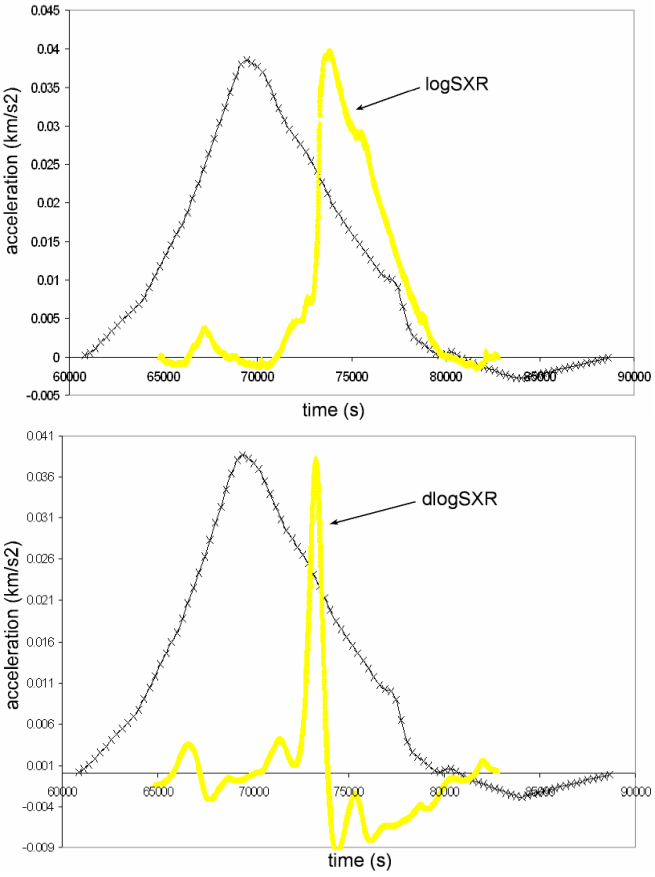

Fig. 5. The event of 2001 April 23. In this event there was soft-X-ray enhancement, but his connected with different active area on the opposite side of sun. This event was not associated with any noteworthy SXR enhancement in the GOES data.

REFERENCES

[1] Forbes, T. G.: 2000, *J. Geophys. Res.* 105, 23153.
[2] Kahler, S. W., Moore, R. L., Kane, S. R., and Zirin, H.: 1988, Astrophys. J. 328, 824.
[3] Maričić, D., Vršnak B., Stanger, A., and Veronig, A.,: 2004, *Solar Phys.* 225, 337.
[4] Neupert, W. M., Thompson, B.J., Gurman, J.B., and Plunkett, S.P.: 2001, *Geophys. Res.* 106, 25215.
[5] Subramanian, P., Ananthakrishnan, S., Janardhan, P., Kundu, M.R., White, S.M., and Garaimov, V.I.: 2003, *Solar Phys.* 218, 247.
[6] Veronig, A., Karlicky, M., Vršnak, B., et al.: 2005, *Astron. Astrophys.*, in press
[7] Vršnak B., Klein, K.-L., Warmuth, A., Otruba, W., and Skender, M.: 2003, *Solar Phys.* 214, 325.
[8] Vršnak B., Maričić, D., Stanger, A., and Veronig, A.,: 2004, *Solar Phys.* 225, 355.
[9] Zhang J., Dere, K.P., Howard, R.A., Kundu, M.R., and White, S.M.: 2001, *Astrophys. J.* 559, 452.
[10] Zhang J., Dere, K.P., Howard, R.A., and Vourlidas, A.: 2004, *Astrophys. J.* 604, 420.

Coronas-F observations of the Sun and Extreme Solar Events

V.D.Kuznetsov

N.V.Pushkov Institute of Terrestrial Magnetism, Ionosphere and Radio Wave Propagation Russian Academy of Sciences, Troitsk, Moscow Region , Russia, kvd@izmiran.ru

In this paper, we provide a review of some results of solar observations and describe the extreme solar events observed in the declining phase of the current activity cycle on the basis of the CORONAS-F data.

Introduction

The CORONAS-F satellite was launched on July 31, 2001 (i.e., close to the maximum of the current cycle 23) to a near-circular orbit with a height of about 500 km and inclination of 83 deg.

The scientific payload of the satellite comprised 15 instruments, most of which (12 devices) were intended for direct observations of the Sun, and three instruments formed the SCR complex and were measuring energy particles along the satellite trajectory and the hard solar radiation. The measuring range of the instruments covered a broad spectrum of radiations and particle energies – from the optical emission to gamma rays and from tens of keV to a few GeV. Some instruments were taking measurements in overlapping energy ranges. This made the CORONAS-F data extremely useful for complex studies, including the study of solar phenomena and their near-Earth manifestations.

Extreme solar events

High-resolution solar images obtained with the CORONAS-F/SPIRIT X-ray telescope in various spectral lines corresponding to different temperature layers in the solar atmosphere made it possible to localize numerous active events in the Sun and to study their morphology [1]. In the declining phase of the current cycle, the outstanding events were recorded during October-November 2003 and in January and September 2005.

Extreme events in October-November 2003

The level of solar activity observed in October and November 2003 was the highest for the past 30 years, and a number of very intensive flares and ejections were recorded during that period. The situation is illustrated in Fig. 1, which shows a lot of active regions with flares, magnetic loops, and very hot areas. The outstanding flares and ejections recorded in the period under discussion might have been due to the global (actually, hemispheric) asymmetry of the active regions on the solar surface (see Fig. 2), i.e., the situation when about 30 active regions existed in one hemisphere and none at all, in another. As a result, large gradients of the magnetic field caused the observed powerful events.Numerous dimmings (see Fig. 1) observed in that period formed as a result of the total or partial opening of the initially closed magnetic field lines in the process of the coronal mass ejections and the associated decrease of the emission measure. The ejections repeated in the same magnetic configurations, which managed to restore their magnetic field and brightness in the lapse of time between the events. The bright regions in Fig. 1 are the post-eruptive arcades.

Fig. 3 represents a record of the nuclear gamma-lines recorded by the AVS device during the flare of November 29, 2003. These lines indicate the presence of various chemical elements and their isotopes in the solar atmosphere. In the case under discussion, these are iron, magnesium, silicon, neon, oxygen, and hydrogen. One can also see a spectral feature corresponding to the line of the trapped flare-generated neutrons. The gamma-radiation spectrum shown in the figure provides the primary spectrum of the flare-accelerated protons, which characterizes the acceleration process itself.

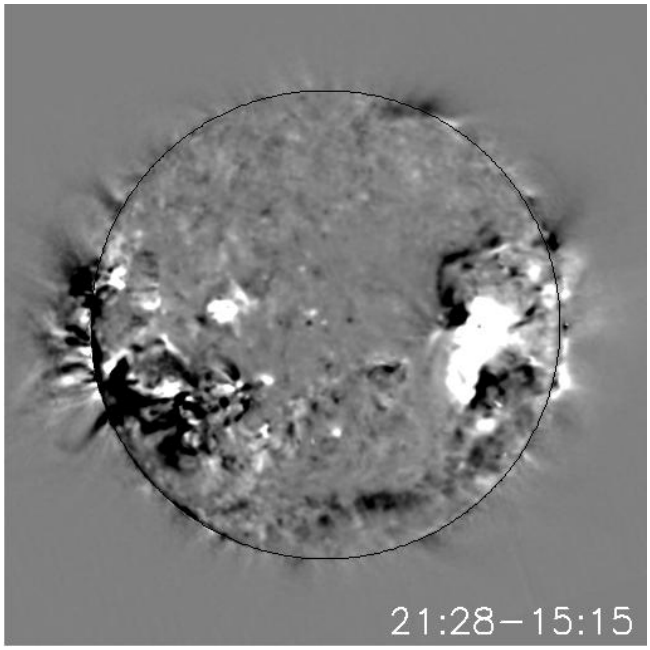

Fig.1. Abnormally high solar activity on October 26, 2003. Dark regions correspond to the decreased emission measure due to the mass evacuation during ejections; light regions correspond to post-eruption arcades

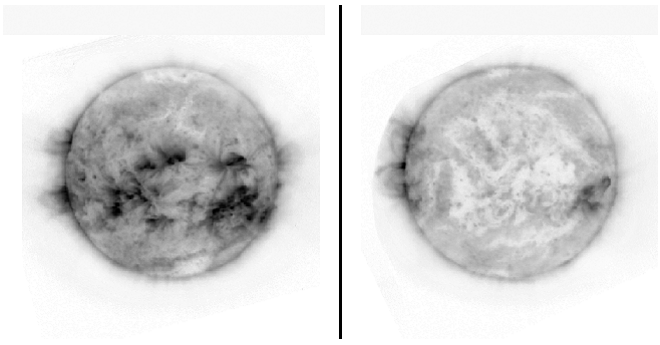

Fig.2. Solar activity in October and November 2003. One can see the longitudinal (hemispheric) asymmetry in the distribution of active regions on the solar surface

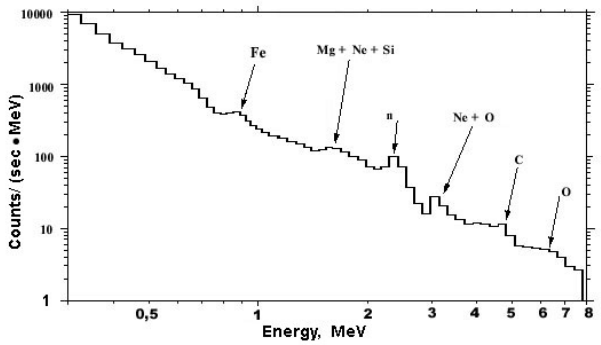

Fig.3. Gamma lines from the flare of October 29, 2003 showing the presence of various chemical elements and isotopes in the solar atmosphere

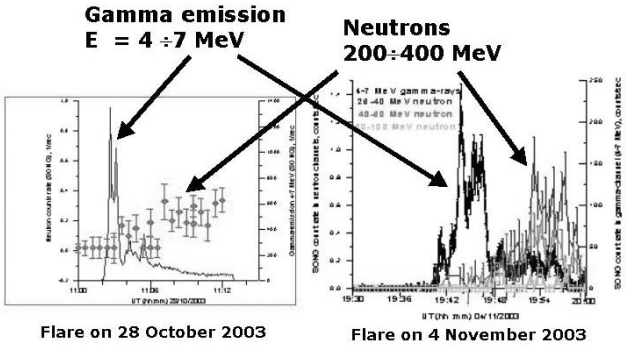

Fig.4. Gamma-ray and neutron fluxes from the flares of October 29 (left) and November 4 (right), 2003

Fig. 4 shows a CORONAS-F/SONG record of the gamma radiation and neutron fluxes from the major flares of October-November 2003. Since neutrons have no charge and move along straight lines, unlike the protons and electrons moving along the interplanetary magnetic field, the neutron data compared with other observations made it possible to determine the time of escape of the accelerated protons from the solar corona.

A distortion of the magnetosphere and radiation belts during two severe magnetic storms caused by the events of October 23-29, 2003 (namely, the motion of the radiation belts inside the magnetosphere accompanied by penetration of the solar energetic particles) is illustrated in Fig. 5. A new effect was revealed consisting in the disappearance of the outer radiation belt of electrons in the main phase of the storm at energies above 1.5 MeV. This is likely to be due to the precipitation of electrons to the loss cone during the geomagnetic field disturbances.

Extreme event of January 2005

Among the records of solar cosmic rays and magnetospheric response to solar flares and ejections obtained with the CORONAS-F scientific complex, we can isolate an interesting interval of January 15-21, 2005 (Fig. 6), when there occurred several flares producing large fluxes

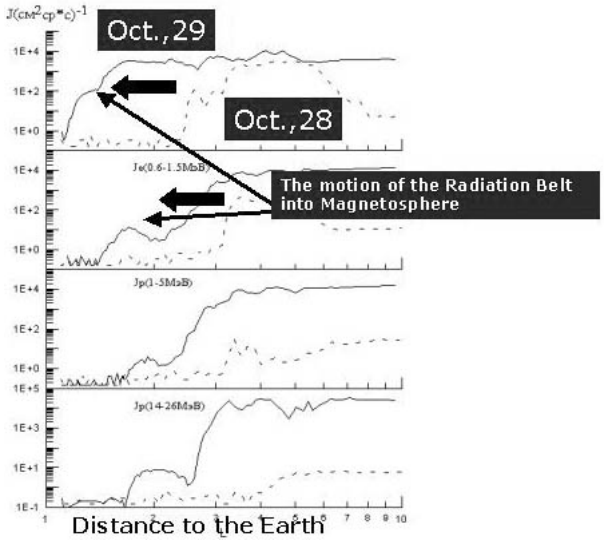

Fig.5. Magnetosphere distortion and penetration of radiation in the events of October 28029, 2003

of energetic particles and a coronal mass ejection, which caused strong disturbances in the magnetosphere and radiation belts. The most complete data are available for the flare of January 20, 2005 (Fig. 7), which was recorded when the satellite was crossing the equator. During a decrease of the high-energy gamma-quanta against the GCR background, we measured an additional increase of the high-energy particle flux (Fig. 6, lower panel) and, using the latitudinal geomagnetic cut-off (i.e., of the anomaly of latitudinal variation of the galactic cosmic rays), estimated the energy of the first particle arrival (~5 GeV). An enhancement of the high-energy particle flux was recorded at the L-shell of ~1.5 at 6:56 UT, while the neutron monitor readings at the South Pole station began to increase at 6:49 UT. The delay in recording the flare-accelerated protons with the threshold energy of 6 GeV at L~1.5 suggests that this is the maximum energy value for these particles. A preliminary analysis of the SPR-N and SONG data from the CORONAS-F and GOES satellites shows that the energy release of that flare was mainly in the form of accelerated particles. The flare-generated coronal mass ejection reached the Earth's magnetosphere on January 21, and the magnetospheric disturbance developed mainly at positive Bz component of the interplanetary magnetic field. The dayside magnetopause approached the Earth to the distance of 5 R_E, and the outer boundary of the radiation belt moved to the shell L~3. The relaxation of the radiation belt after the storm lasted longer than in the case of the classical storms.

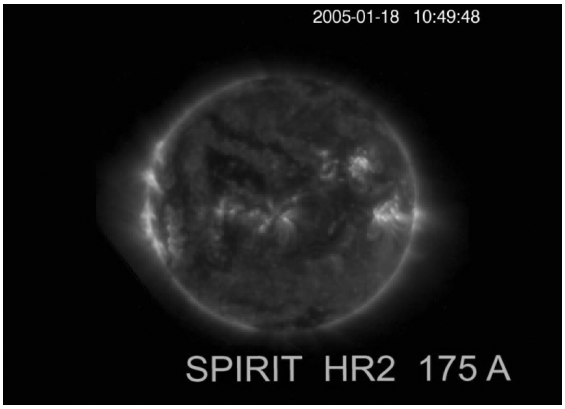

Fig.6. Image of the solar surface as observed by CORONAS-F/SPIRIT on January 18, 2005

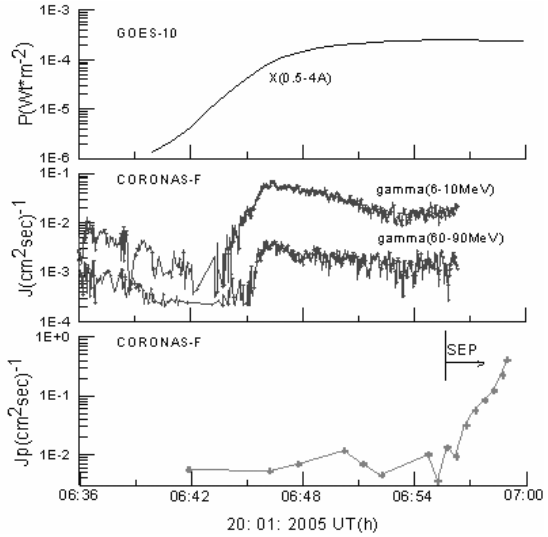

Fig.7. Emission of the solar flare of January 20, 2005.Upper panel – thermal X-ray flux (3÷24 keV, GOES-10). Middle panel – counting rate of hard gamma quanta from bremsstrahlung in the range of 6÷10 MeV and from the decay of pions generated in nuclear reactions of the accelerated relativistic protons with the nuclei in the solar corona (40÷90 MeV). The lower panel – additional increase of the counting rate of high-energy charged particles (protons) in the energy range > 100 MeV. SEP – solar energetic particles

Extreme events of September 2005

A series of extreme events occurred in the Sun from September 6 to September 17, 2005: 10 X-ray flares of importance X and 27 flares of importance M accompanied by intensive coronal mass ejections and severe geomagnetic storms. During that period, the CORONAS-F/SPIRIT device recorded 13 flares. All outstanding events were associated with a large active region AR10808 with a complex magnetic structure, which appeared from behind the eastern limb and produced a super-powerful flare of importance X17.1/3B (beginning at 17:17 UT, maximum at 17:40 UT, and end at 18:47 UT). It was the fifth flare in intensity and the largest in total flux of soft X-rays for 30 years of observations. The flare image was obtained with the CORONAS-F/SPIRIT telescope at 18:18 UT (Fig. 8). In spite of the flare position at the eastern limb, a great number of solar accelerated particles (including >1000 MeV protons) reached the Earth in short time. The maximum proton flux with an energy >10 MeV (1880 pfu) was recorded at the beginning of September 11, and the maximum flux of the >100 MeV protons (~10 pfu), at the end of September 9. About 43 hours after the flare beginning, an interplanetary shock reached the Earth, and a minor geomagnetic storm began. A geomagnetic pulse of 89 nT was recorded on the day side on September 7. The electromagnetic impact on the Earth's environment was maximum - R5 (Radio Blackout). The intensity of hard X-rays in the range of 100-300 keV exceeded the values recorded during the extreme events of November 4, 2003.

The analysis of the images obtained in the 175 Å coronal lines with temperatures of about 1.2 MK shows that all flare events observed were accompanied by a radical reconstruction of the magnetic field lines in the flare region (Fig. 9). The major limb flare of September 7, 2005 was accompanied by coronal mass ejections at a speed of about

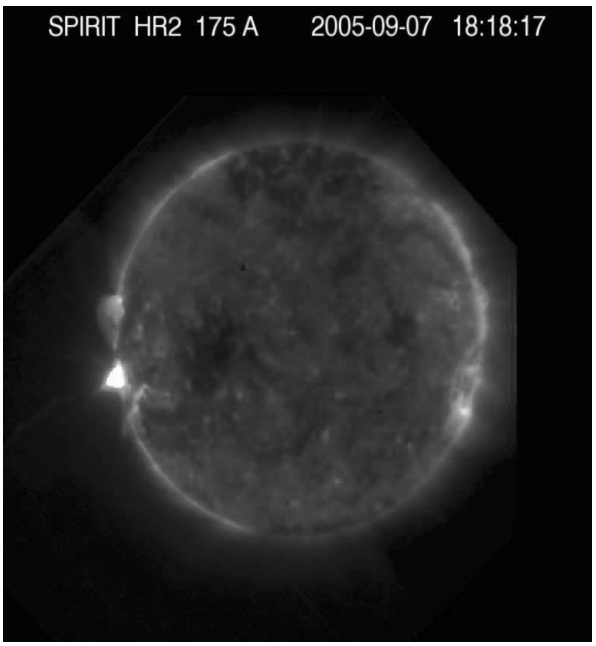

Fig.8. Solar limb flare of September 7, 2005 as observed by CORONAS-F/SPIIT

550 km/s. As a result of these ejections, deep dimmings (temporary decreases of brightness associated with the evacuation of matter during the ejection) are observed on the solar images at 175 Å. On September 7, after the outstanding flare X17 at 17:40 UT and the associated coronal ejection, the decrease of the emission intensity at 175 Å in the dimming was about 7% of the total solar irradiance. On September 13, after the flares X1.5 at 19:27 UT and X1.7 at 23:22 UT, the emission in the dimming decreased by about 5%. Simultaneous observations of the solar corona with the CORONAS-F/SPIRIT spectroheliograph in the ranges of 177-210 Å and 280÷335 Å provided the line spectra corresponding to the pre-flare and maximum phases of the flare evolution and allowed us to detect the appearance of multiple hot lines and the general increase of the line intensities in the flare maximum phase. The ratio of the emission line intensities in the spectra of the limb flare of importance X17 recorded on September 7, 2005 were used to determine the differential emission measure. Its temperature dependence reveals that the maximum emission of the flare-generated plasma falls within the temperature range in the vicinity of 10 MK.

When passing along the disk, the active region AR10808 had the area >1400 m.v.h. and contained multiple delta-

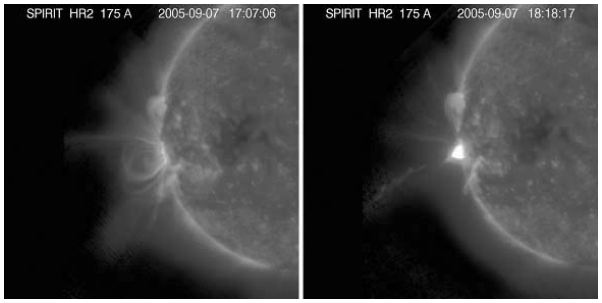

Fig.9. Limb structure of the solar corona under pre-flare conditions (left) and in the maximum phase (right) of the importance

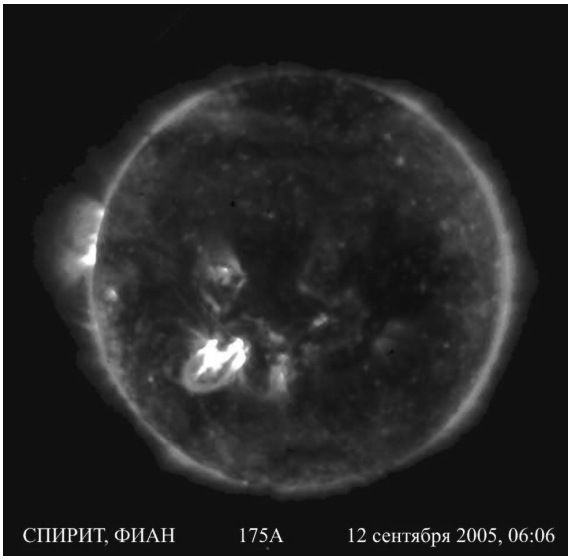

Fig.10. Active region AR10808 on the solar disk

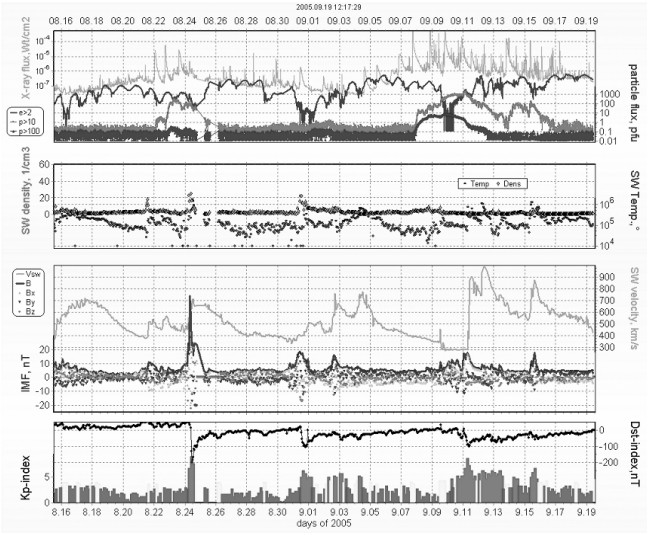

Fig.11. Heliogeophysical activity in September 2005

configurations (see Fig. 10). The series of the flares observed in that AR, caused strong long-lasting geomagnetic disturbances on the Earth (Fig. 11). The magnetic storm, which started on September 10, reached its maximum on September 11. Magnetic storms were observed for six days running (September 9-15) and essential disturbances, for 8 days running (September 9-16). The daily mean Ap-index on September 11 was 105. The Ap-index during the whole interval from September 9 to September 16 had the values 17, 30, 105, 66, 51, 25, 43, and 18. One of the greatest Forbush effects in the current cycle (the forth in magnitude) equal to 13% was recorded on the night of September 10-11.

Later, on September 19, the active region AR 10808 decreased and simplified significantly, but still conserved a delta-configuration.

Observation and analysis of the flare-generation emissions

Flare spectrometer IRIS

The mathematical treatment of the intensity time profiles of the emission from minor flares obtained during 2005 and earlier revealed complex time features with the pulses of about 3-5 s in the profiles of soft and hard X-rays (3÷40 keV), which could be isolated against the background of 10-s pulses. X-ray flux variations with a time scale of about 20 s were detected in the energy range of ~100÷150 keV. Variations in the time structure of the emission intensity with the phase of the cycle were studied to reveal an intensive quasi-periodic component with a period of about 20 s and a few weaker components with the periods from 4 to 12 s existing in the pre-flare phase. In the post-flare phase, nearly all components split into two o more elements and the emission energy is mostly concentrated in the region of small periods. The physical interpretation of the outstanding events under discussion is associated with treating the complex magnetic features existing in the solar atmosphere (flare loops and arcades) as a system of the connected oscillators, which can change their frequency and oscillation amplitude, collapse, and re-appear in the course of the flare evolution, as well as with the energy exchange between the flare loops. One-second oscillations of the emission intensity can be accounted for by MHD waves "running" along the magnetic loop, which arise as a result of disturbance at one end of the loop. For the typical parameters of the coronal plasma, the numerical estimates of the magnetic loop oscillation periods during a flare range from 2.2 to 66 s.

The study of the dynamics of the hard X-ray energy spectra in different phases of the flare evolution with a time resolution of 1 s has shown that, for some flares, the spectrum is perfectly well described in all phases by the power-law function with the power index changing in time. At the peak of the emission intensity, the spectrum index decreases, and in the decay phase increases. Flares were also observed, in which an intricately shaped spectrum consisting of two components was formed in the growth and maximum phases. The spectrum below 45 keV was, probably, formed by the thermal emission of hot plasma, and above 45 keV, by the bremsstrahlung of fast electrons. Such a shape of the spectrum was conserved in the flare decay phase. As the energy increased, the emission spectrum became steeper. This can be explained if we suggest that the distribution function of the fast electrons generating the X-ray bremsstrahlung has a cut-off at a certain maximum energy of about 150-170 keV. The cut-off in the spectrum of the fast electrons can arise due to interaction with plasma waves, taking into account the non-linear scatter of these waves on the background plasma ions.

Amplitude-time spectrometer AVS-F

The time profiles of the counting rates of gamma quanta from a number of solar flares obtained with the AVS device in various energy ranges corresponding to the nuclear lines, positron line, and neutron trapping line were analyzed to reveal features with the time scales from 16 to 80 c.

A similar analysis in the energy range of 0.1÷20 MeV with a time resolution of 1 ms showed the presence of fine structures with typical time scales from 7 to 35 mc in the time profiles of some flares (e.g., in the flare of January 20, 2005).

Ultraviolet emission

With the aid of the ultraviolet solar radiometer SUFR-Sp-K and ultraviolet spectrophotometer VUSS-L, it was possible to measure the fluxes of ultraviolet radiation of solar flares. Fig. 12 provides an example of such

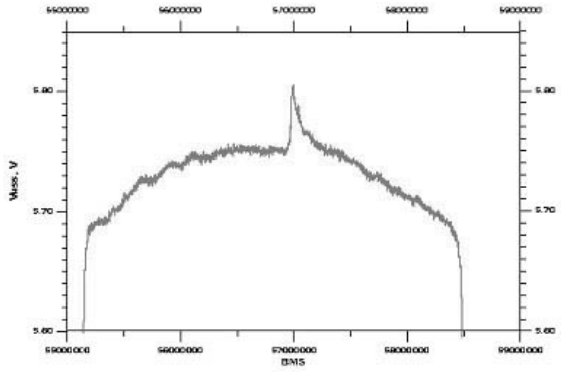

Fig.12. Ultraviolet emission flux recorded during the solar flare of January 21, 2003 in the Lα line (at wavelengths shorter than 130 nm)

measurements in the Lα-line (in the wavelength range below 130 nm) carried out with the VUSS device during the flare of January 21, 2003. For X-ray flares of importance C9-M1, the typical variation of ultraviolet radiation within the band near the Lα-line is approximately 0.5%. In the most intensive flares, the enhancement of ultraviolet radiation in the 120-nm range does not exceed a few percent.

Helioseismic observations within the CORONAS-F/DIFOS experiment

Continuous helioseismic observations with a multi-channel spectrophotometer on board the CORONAS-F satellite were started in August 15, 2001. An important result of those observations was that they showed the feasibility of helioseismic studies based on satellite observations on the Earth's orbit. Such studies became possible owing to the newly developed methods that allowed us to fill the gaps in data in the periods of crossing the Earth's shadow, to subtract the light reflected from the Earth's atmosphere and detected by the spectrophotometer, to analyze the data obtained and compare them with the results of other observations and theoretical investigations.

The multiple channels of the DIFOS spectrophotometer (350, 500, 650, 850, 1100, and 1500 nm), which distinguish it significantly from the other space-borne devices for observing the fluctuations of the solar luminosity, allowed us to examine the phase shift of the oscillations [2] observed in different channels of the instrument and to reveal a

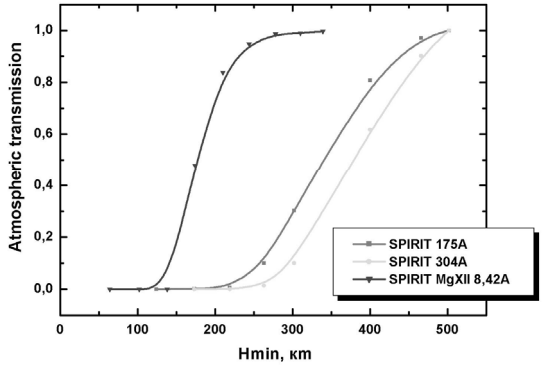

Fig.14. The transparency of the Earth's atmosphere as a function of altitude H_{min}

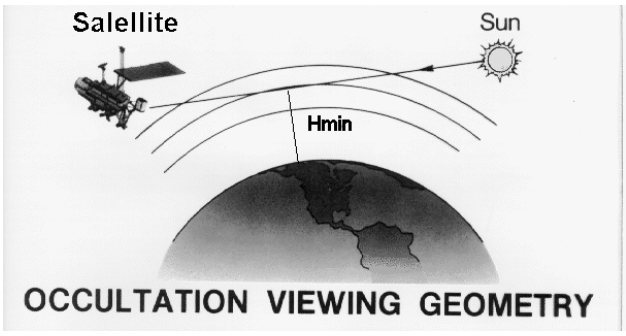

Fig.13. The scheme of measuring the transparency of the Earth's atmosphere from solar observations with the CORONAS-F/SPIRIT X-ray telescope

previously unknown effect: the motion of oscillations from the upper and lower to the middle layers of the photosphere. The fact that oscillations move downward from the upper photosphere, while their source is under the photosphere in the convection zone cannot be explained in terms of the adiabatic theory usually applied to helioseismic observations. The waves run to the middle of the photosphere where the oscillation damping is the strongest due to the non-adiabaticity; i.e., the middle layers ensure a sink of the energy carried by the waves from above and below. This newly found effect is a direct evidence of non-adiabaticity of the evanescent *p*-modes of oscillations in the photosphere.

Earth's upper atmosphere

The Earth's upper atmosphere was studies by the X-ray absorption recorded with the CORONAS-F/SPIRIT X-ray telescope as the satellite entered and left the Earth's shadow (see Fig. 13). Such observations were used to establish the latitude dependence of the X-ray absorption coefficients with the height resolution improved by a factor of about 100 (Fig. 14). The dependence of the density and composition of the Earth's atmosphere on the solar activity level was studied up to the altitudes of 500 km, and the content of the molecular nitrogen and atomic oxygen was determined.

Similar observations were carried out in the ultraviolet range with the SUFR radiometer and VUSS spectrophotometer. A special method was developed to determine the content of the molecular oxygen – one of the main constituents of the atmosphere. These observations provided experimental data necessary to construct an updated model of the Earth's atmosphere. Along with the well-known precipitations of energetic particles from the

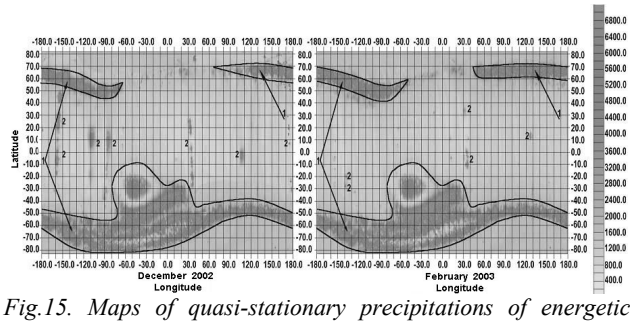

Fig.15. Maps of quasi-stationary precipitations of energetic particles from the magnetosphere to the ionosphere. 1 – radiation belts, 2-quasi-stationary precipitations

magnetosphere to the ionosphere observed in the polar regions and in the zone of the Brazil anomaly, the AVS device detected localized (about 30° in geographical latitude and about 10° in geographical longitude) quasi-stationary low-latitude and equatorial precipitations (see Fig. 15), whose origin still remains unclear. These precipitations are characterized by a noticeable (by 20-30%) increase of the background radiation. Their lifetime can reach 8 days.

Conclusion

The results of observations of the CORONAS-F mission are provided in the reviews [1, 3-10]. The author is grateful to I.A.Zhitnik, S.V.Kuzin, S.N.Kuznetsov, Yu.D.Kotov, N.I.Lebedev, and Yu.D.Zhugzhda for the data used in this paper.This work is supported by Russian Foundation for Fundamental Research (grant №06-02-16359).

REFERENCES

[1] V.Kuznetsov, I.Zhitnik, I.Sobel'man. "CORONAS-F: Contribution to Solar-Terrestrial Physics", Vestnik RAN, Vol.75, 8, 2005, pp704-714

[2] Yu.Zhugzhda. "Analytical signal as a tool for investigation of the properties of p-mode oscillations on the Sun", Pis'ma v Astronomicheskii Zhurnal, Vol.32, 5, 2006, pp1-16 (Astronomy Letters, 2006, in press)

[3] V.Oraevsky, I.Sobelman. "Comprehensive Studies of Solar Activity on the CORONAS-F Satellite". Astronomy Letters, Vol.28, 6, 2002, pp401-410 (Translated from Pis'ma v Astronomicheskii Zhurnal, Vol.28, 6, 2002, pp457-467)

[4] V.Oraevskii, I.Sobel'man, I.Zitnik, V.Kuznetsov. Comprehensive solar studies by CORONAS-F satellite: new results. Physics – Uspekhi, Vol.45, 8, 2002, pp886-896 (Translated from Uspekhi Fizicheskikh Nauk, Vol.172, 8, 2002, pp949-959)

[5] V.Oraevsky, I.Sobel'man, I.Zitnik, V.Kuznetsov, A.Stepanov, G.Polischuk, P.Kovilin, A.Negoda, V.Dranovsky, Ya.Yatskiv. "CORONAS F observations of active phenomena on the Sun", J. Adv. Space Res., Vol.32, 12, 2003, pp2567-2572

[6] V.Kuznetsov. "The Solar Observatory CORONAS-F: Three Years of Observations of Solar Activity", COSPAR Inf. Bull., 161, 2004, pp90-93

[7] V.Kuznetsov, Yu.Charikov, Yu.Kotov, S.Kuznetsov, E.Mazets, A.Nusinov, V.Pankov, I.Sobelman, J.Sylwester. "A review of the solar results from CORONAS-F satellite", Proc. IAU Symp.223 "Multi-Wavelength Investigations of Solar Activity", 2004, pp357-366

[8] J.Sylwester, I.Gaicki, Z.Kordylewski, M.Kowalinski, S.Novak, S.Plocieniak, M.Siarkowski, B.Sylwester, W.Trzebinski, J.Culhane, M.Whyndham, R.Bentley, P.Guttridge, J.Lang, K.Phillips, C.Brown, G.Doschek, V.Oraevsky, V.Kuznetsov, A.Stepanov, D.Lisin. "RESIK – Bent crystal solar X-ray spectrometer for studies of Coronal Plasma Composition", Solar Physics, Vol.226, 1, 2005, pp45-72

[9] V.Kuznetsov. "The Results of Study of the Sun and Solar-Terrestrial Relations with the CORONAS-F Satellite: A Review", Solar System Research, Vol.39, 6, 2005, pp433-441

[10] V.Kuznetsov. "Results of the CORONAS-F observation of solar flares and active events in the Sun", Izvestiya Rossiiskoi Akademii Nauk. Seriya Fizicheskaya, Vol.70, 16, 2006, pp58-63 (will be published in Bulletin of the Russian Academy of Sciences: Physics)

Dynamic of Electromagnetic Emission during the Period of Solar Extreme Events

M.S. Durasova, V.M. Fridman, T.S. Podstrigach, O.A. Sheiner, S.D. Snegirev, Yu.V. Tikhomirov

Radiophysical Research Institute, Nizhny Novgorod, Russia, rfj@nirfi.sci-nnov.ru

This work is devoted to study the behavior of solar emission during the period of January 2005. The analysis is based upon observations made with Radio telescopes in the out-of-town observatory NIRFI "Zimenki".

Introduction

A study of the conditions for appearance and development of the processes, which lead to the explosive phenomena with the large energy release require a special attention. In this case the basic tools, with the aid of which it is possible the solution of the problems of flare energy release regions and coronal mass ejections formation should be the research of the spectral composition of emission, the study of the wave and fluctuating motions and the dynamics of magnetic field. The study of the characteristics of radio emission and their dynamics over a wide range of wavelengths plays an important role. It is so because of the majority of the phenomena of different nature find effective reflection in the radio emission, and the value of spectral range bears information about the spatial structure of processes at different layers of solar atmosphere.

It is established that 2-3 days prior to the event of powerful energy release in the atmosphere of the sun occur the processes, whose action brings to such events, finally. They are floating up of new magnetic fluxes [1], the complication of the magnetic structure of sunspots groups [2], energy storage in the active region and developing in this case nonstable processes, which bring subsequently to the reconnection of magnetic pour [3]. All these processes are reflected in the radio emission, for example, in such forms as a "step-like" increase in the intensity of the microwave emission of active regions [4], the complication of the structure of polarized radiation from the sunspots [5], the appearance of a radio source above the neutral line of magnetic field [6]. Achievements in the study of wave motions in the active regions by the radio methods are connected with the detection of long-period (with period of more than 20 minutes) pulsations. Effect of the growth of such long-period pulsations in the cm solar radio emission 2-3 days before proton flares has been discovered in the events of August 1972 [7] and later was confirmed, using specially developed equipment in observations [8].

The presence of the special features in the radio emission, which precede the registration of Coronal Mass Ejections (CMEs), accompanied Solar Extreme Events, attests to the fact that the processes of energy storage and (or) the appearances of instabilities, which lead to the formation CMEs occur on the Sun. According to the existing opinion, these processes begin on the surface of the Sun and in the lower layers of solar atmosphere [9]. Since the microwave emission is formed precisely in these layers, a study of sporadic phenomena in the radio-frequency band before the registration of CMEs for the development of laws governing such processes must be sufficiently effective [10].

In this research project we have continued analyzing the radio data preceding registration of CMEs: the events and their dynamics in the centimeter and decimeter ranges of radio waves.

Set of data

We study solar radio emission during the period of January 2005, period of solar extreme events. The analysis is based upon observations made with radio telescopes in the out-of-town observatory of Radiophysical Research Institute (NIRFI) "Zimenki". We have monitoring observations of solar radio emission in cm-dm frequency range: 9114, 2950, and 900 MHz.

As it is seen from the data processes leading to main solar events start to be visible in solar radio emission during 2-3 days before the events. Using routine solar observational data of 4 powerful flares of January, 2005 (15, 17, 19, and 20) and CMEs are examined. The possibilities of realization the procedure of powerful flares prediction on the base of monitoring observations of long-period pulsations are considered.

Results and discussion

Figs. 1 (a, b, and c) presented below are the behaviour of solar radio emission during calm periods far away from solar flares (figures are presented in different scales). As we can see there are no distinctive long-period pulsations in radio emission.

Figs. 1 (d, e, and f) present the time behaviour of microwave emission during the days close to main solar flares. We detect the growth of amplitude of long-period (with a period of more than 20 minutes) pulsations before powerful flares.

The intervals following the previous one coincide with periods preceding CMEs and flare registration. It was established earlier that sporadic events in solar radio emission accompanied CMEs formation. Sporadic radio emission prior to the 2-hour interval up to the registration the CMEs on the coronagraphs is analyzed. The selection of this interval is explained by the results of studies about the mean lifetime of the precursors of CMEs, which is on the average ~ 30 minutes [11]. The so-called "single" events were selected from the entire set of data - when the preceding event of CMEs was recorded not less than 8 hours prior to, and the following event recorded not less than 6 hours after the event in question [12]. The above selection was caused by the available data about the characteristic recovery times of the structure of active region after the passage of CMEs and the existence of sporadic phenomena in the radio-frequency band on the phases before and after passage of CMEs [12].

Tables 1 and 2 contain the list of sporadic components of radio emission called microwave precursors for flares January 17 (intensity max was observed at about 09:28UT) and 19 (max of microwave burst was observed at 09:40 UT).

As we see from the Tables during the time interval of 1.5h on January 17 and 1h on January 19 just before flash phase of the burst one can see such small events as simple

impulsive ***C***, simultaneous numerous frequencies ***GRF, RF*** or ***SER***. Most of sporadic events are broad-band, because of they are observed in all used frequencies (types of broad-band precursors are marked as bold in Tables I and II). This fact is the confirmation of preliminary formulated rules.

Both of these events (January 17 and 19, 2005) are accompanied by Halo type CMEs [13]. There were events with extremely high speed: more than 2000 km/s.

Figs. 2 and 3 present temporal behaviour of microwave emission during powerful events of January 17 and 19, consequently. On January 19 the flash phase of burst is ahead the CMEs registration on 30 min, and on January 17 this interval is about 48 min. The last fact cannot be explained as initial CMEs propagation in solar atmosphere because of very high speed of CMEs. The phenomenon of CMEs' output seems to be during sharp growth of radio emission.

It is well known that there is a lot of research on the diagnostic possibilities of flare loops parameters, using parameters of the periodic oscillations of radio emission in the bursts. Our study of oscillations in time period closer to the bursts can be considered as the illustration of wave dynamics.

Figure 4 presents power spectrum of solar radio flux during different time interval before the main energy release: Fig. 4 (a, b) ─ in 100 min; Fig. 4 (c, d) ─ in 60 min; and Fig. 4 (e, f) ─ in 50 min.

As it is seen from the pictures: the earlier observations are - the noisy behavior of spectrum is. Whereas the closer to the main phase of the burst the bigger amplitude of spectral component with observing allocated periods of about 14-22s.

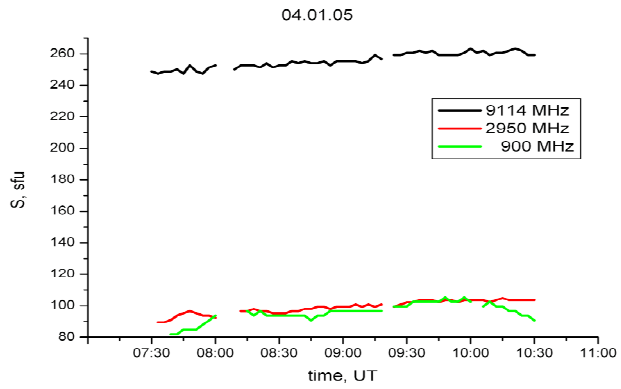

Fig.1a

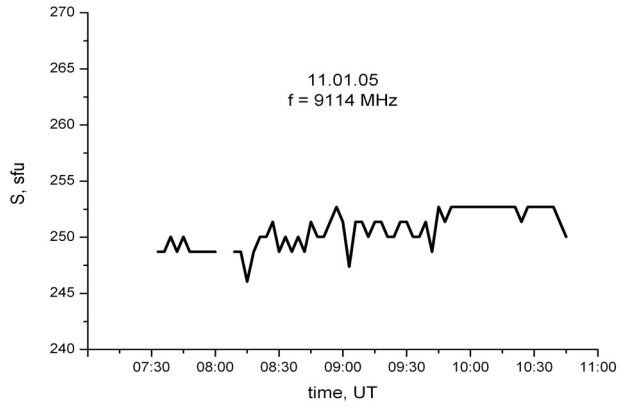

Fig.1b

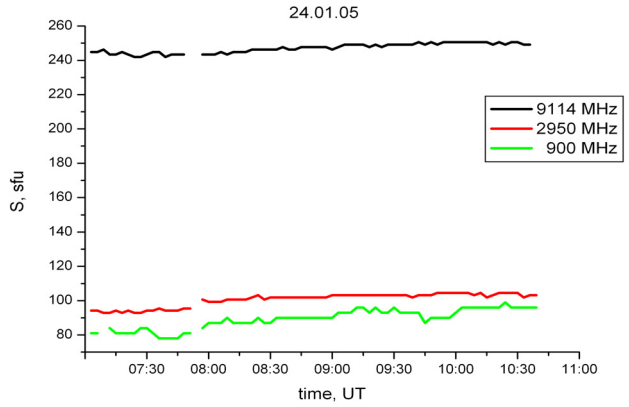

Fig.1c

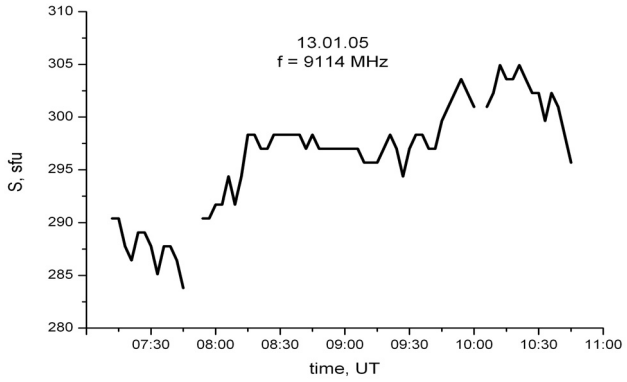

Fig.1d

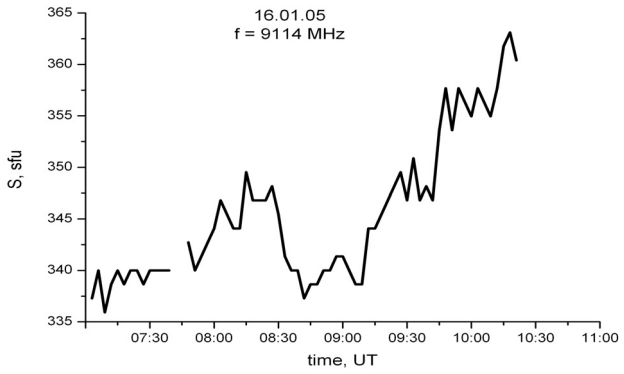

Fig.1e

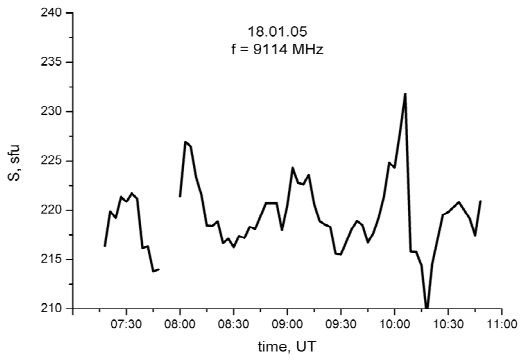

Fig.1f

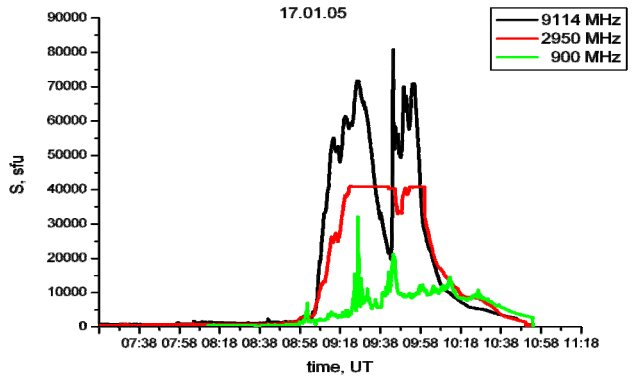

Fig 2

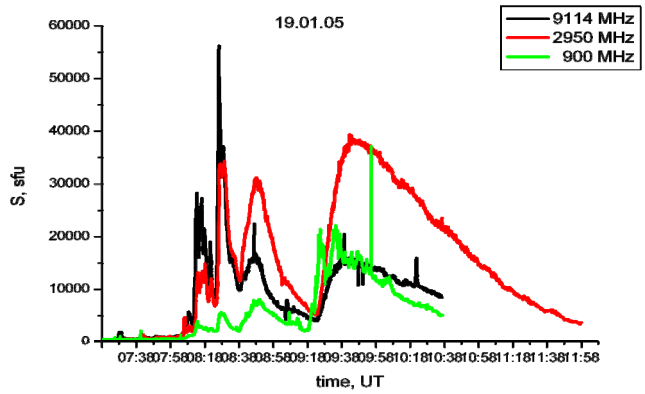

Fig 3

TABLE I

January, 17. 2005

Frequency MHz	Type	Start UT	Max UT	Duration min	Flux sfu
9114	**GRF**	**0709.0**	**0712.8**	**39**	**31**
2950	**GRF**	**0711.E**	**0712.8**	**7.5**	**7**
900	**GRF**	**0709.0**	**0733.0**	**36**	**9**
9114	**RF**	**0751.0**	**0841.0**	**50**	**115**
	SF	0755.3	0756.4	4.5	102
			0756.7		95
	GRF	0804.0	0819.5	23	37
	SER	0804.0	0804.4	8.5	150
			0804.6		150
			0806.3		31
			0806.7		39
			0807.6		53
			0808.6		92
			0809.5		48
	SF	0812.6	0814.6	5	24
			0815.2		24
	SF	0831.3	0831.6	2	45
2950	**RF**	**0721.5**	**0850.0**	**88.5**	**90**
	S	0755.8	0756.7	3.3	11
	GRF	0804.0	0819.0	23	26
	SER	0804.0	0804.3	9.3	11
			0804.6		49
			0804.9		88
			0809.0		33
	SF	0831.3	0831.6	1.5	26
	SF	0837.0	0837.5	1.3	7
	SF	0840.3	0841.5	2.7	37
900	**RF**	**0839.0**	**0857.0**	**18**	**75**
	SF	0841.0	0841.7	1.5	72
	SF	0844.7	0845.0	1.3	51
	SF	0850.0	0850.5	1.4	21
	SF	0852.6	0853.0	0.8	33

TABLE 2

January, 19. 2005

Frequency MHz	Type	Start UT	Max UT	Duration min	Flux sfu
9114	**GRF**	**0707.0**	**0712.8**	**13**	**19**
	RF	**0724.0**	**0803.0**	**39**	**88**
	SF	0727.0	0728U	6	>270
	SF	0739.0	0740.4	7	139
			0740.8		110
			0741.4		165
			0741.6		131
	SF	0747.0	0749.4	9	85
			0749.8		76
			0750.2		58
			0750.6		54
	RF	0757.0	0757.5	6	19
			0801.5		80
			0802.0		77
			0802.5		83
2950	**RF**	**0717.0**	**0747.0**	**30**	**26**
	SF	0727.0	0728.6	3	62
	SF	0740.0	0740.5	7	26
			0741.5		54
			0741.7		130
			0742.0		150
			0742.2		113
	RF	**0747.0**	**0803.0**	**16**	**81**
	SER	0747.0	0749.7	15.5	74
			0751.5		44
			0753.2		52
			0755.5		32
			0756.0		45
			0757.2		64
			0757.5		68
			0758.5		33
			0801.5		26
			0802.5		56
900	**GRF**	**0725.3**	**0728.8**	**4.8**	**13**
	S	0725.3	0725.5	0.3	72
	S	0728.3	0728.4	0.2	122
	GRF	**0740.0**	**0743.5**	**5**	**16**
	SER	0740.0	0740.3	2	165
			0740.5		330
			0740.7		90
			0741.5		20
	GRF	**0747.0**	**0754.0**	**14.5**	**16**
	SF	0803.6	0803.6	0.7	155
			0803.8		60
	RF	0804.4	0808.0	4	112

To compare the behavior of components analogous results are presented in Fig. 4 (g, h) obtained during the falling part of burst.

Conclusion

Thus, in this paper we demonstrated the dynamics of sporadic radio emission phenomena for the extreme events of January 2005 on the base of monitoring observations. It is seen that microwave emission reflects the processes, proceeding in the lower solar atmosphere at the stage preceding the most powerful phenomena of solar activity.

Dynamic events in microwave emission include: the dynamics of the long-period pulsations of solar radio emission in 1-3 days prior to powerful solar flares, spectral compositions and the dynamics of CMEs precursors in 2-hour interval just before the CMEs' registration, increase the amplitude of periodic components of microwave emission in the range of 14-22 seconds directly before the powerful flares.

All of these, in our opinion, are the evidence of the effective using of microwave observations data for the analysis of the processes preceded solar extreme events.

Acknowledgments

The work is carried out with the support of Russian Fund for Basic Research and FPSTP "Integration" (p. Space Weather).

REFERENCES

[1] H. Wang, P. Gallagher, V. Yurchyshyn et al., BBSO, № 1117, 2001.
[2] Y. Zhang, J.H. Lin, H.Q. Zhang. "Coronal and Stellar Mass Ejections"; Proceedings IAU, Symposium No. 226. K.P. Dere, J. Wang & Y. Yan, eds. – Cambridge: Cambridge University Press, 2005, p. 229.
[3] B. Somov. "Actual problems of nature of solar and stellar activity". International Meeting (N.Novgorod, 2-7 June 2003): Proceedings. Vol. 1. – Nizhny Novgorod: IAP RAS, 2003, p. 75.
[4] N. Kardapolova, V. Nefed'ev, G. Smol'kov. "Prediction of solar activity and observations of solar active events". Symposium KAPG: Programme and abstracts. – Leningrad: GAO AS SSSR, 1987, p.54.
[5] V. Bogod, S. Tokhchukova, Pis'ma AZh, Vol.29, №4, 2003, p.305.
[6] G. Gel'freikh, Izv. RAS, ser. Physicheskaya, Vol.59, №7, 1995, p. 90.
[7] M.M. Kobrin, A.I. Korshunov, S.I. Arbuzov, V.V. Pakhomov, V.M. Fridman, Yu.V. Tikhomirov, Solar Physics, Vol. 56, 1978, p. 359.
[8] S.V. Semenova, V.M.Fridman, O.A.Sheiner, et al. "About the Possibility of Creation the Methodic of Short-Term Prediction for Solar Proton Flares on the Base of Long-Period Pulsations of Solar Radio Emission", Preprint NIRFI [in Russian], Gorky, N228, 1987.
[9] G. Zhou, J. Wang, Z. Cao, A&A, Vol. 397, 2003, p. 1057.
[10] O.A. Sheiner, V.M. Fridman. "Spectral features in solar microwave emission preceding CME onset", "Coronal and Stellar Mass Ejections": Proceedings IAU, Symposium No. 226. K.P. Dere, J. Wang & Y. Yan, eds. – Cambridge: Cambridge University Press, 2005, pp. 233-234.
[11] O.A. Sheiner, M.S. Durasova. "Solar microwave precursors and coronal mass ejections: possible connection", Radiophysics and Quantum Electronics, Vol.37, N 7, 1994, p.883.
[12] O.A. Sheiner, V.M. Fridman, M.S. Durasova. "Characteristics of nonstationary solar radio emission corresponding to CMEs formation in solar atmosphere", Proceeding "SOLSPA: The Second Solar Cycle and Space Weather Euroconference", Vico Equense, Italy, 24-29 September 2001 (ESA SP-477, February 2002), pp.373-376.
[13] http://cdaw.gsfc.nasa.gov/CME_list/

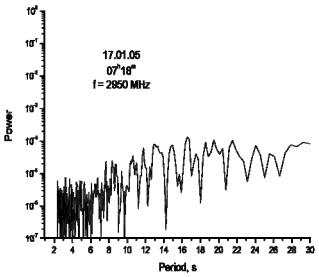

Fig. 4a

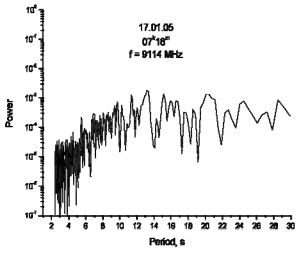

Fig. 4b

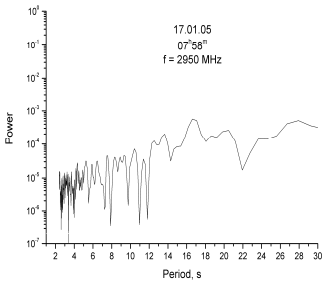

Fig. 4c

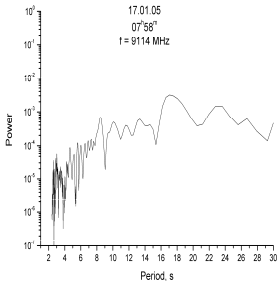

Fig. 4d

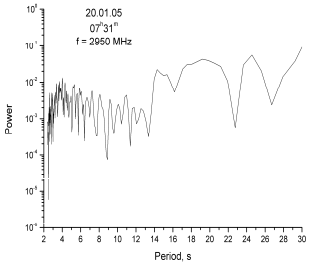

Fig. 4g

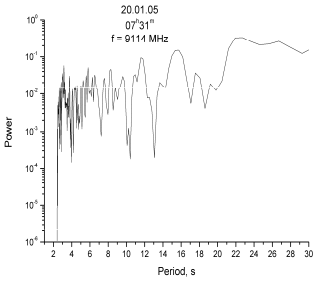

Fig. 4h

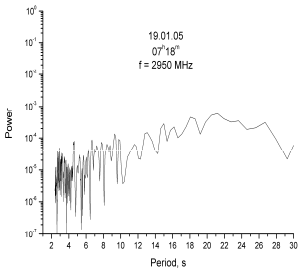

Fig. 4e

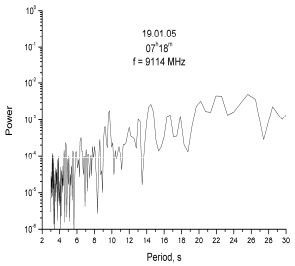

Fig. 4f